COMPUTATIONAL INVESTIGATION OF LOW-PRESSURE TURBINE AERODYNAMICS

A Thesis
Submitted to the Graduate Faculty
of the
North Dakota State University
of Agriculture and Applied Science

By

Alexander Paul Flage

In Partial Fulfillment of the Requirements
for the Degree of
MASTER OF SCIENCE

Major Department:
Mechanical Engineering

April 2015

Fargo, North Dakota

North Dakota State University
Graduate School

Title

Computational Investigation of Low-Pressure Turbine Aerodynamics

By

Alexander Paul Flage

The Supervisory Committee certifies that this ***disquisition*** complies with North Dakota State University's regulations and meets the accepted standards for the degree of

MASTER OF SCIENCE

SUPERVISORY COMMITTEE:

Dr. Bora Suzen
Chair

Dr. Ghodrat Karami

Dr. Om Yadav

Dr. Forrest Ames

Approved:

4/16/2015
Date

Dr. Alan R. Kallmeyer
Department Chair

ABSTRACT

The design of today's gas turbine engines is heavily reliant on accurate computational fluid flow models. Creating prototype designs is far more expensive than modeling the design on a computer; however, current turbulence and transitional flow models are not always accurate. Several turbulence and transition models were validated at North Dakota State University by analyzing the flow through a low pressure turbine of a gas turbine engine. Experimental data for these low pressure turbines was provided by the University of North Dakota. Two separate airfoil geometries are analyzed in this study. The first geometry is a first stage flow vane, and the second geometry is an incidence angle tolerant turbine blade. Pressure and heat transfer data were compared between computations and experiments on the turbine blade surfaces. Simulations were conducted with varying Reynolds numbers, Mach numbers, and free stream turbulence intensities and were then compared with experiments.

ACKNOWLEDGMENTS

I would like to extend my extreme gratitude to Dr. Bora Suzen for the opportunity to research under him. He has been extremely helpful and has proved to be a wealth of knowledge throughout the research process.

I would like to thank Dr. Forrest Ames at UND for the guidance and help on the experimental side of this research.

I would like to thank Dr. Karami, Dr. Ames, and Dr. Yadav for taking the time to be part of my graduate committee.

I would like to Jamison Huber for his previous work on this research and preparing everything very well for me to continue.

Finally, I would like to thank my wife Lily for the love and support through graduate school.

TABLE OF CONTENTS

LIST OF TABLES

Table Page

LIST OF FIGURES

LIST OF SYMBOLS

c ..... chord length, m

C_f ..... skin friction, $\frac{\tau_w}{\frac{1}{2}\rho_\infty U_\infty^2}$

C_p ..... pressure coefficient, $\frac{(p_{total}-p)}{\frac{1}{2}\rho_\infty U_\infty^2}$

$FSTI$ ..... free stream turbulence intensity

h ..... heat transfer coefficient, W/m^2-K

K_t ..... flow acceleration parameter, $\left(\frac{\nu}{U^2}\right)\left(\frac{dU}{ds}\right)$

L_{ref} ..... reference length

P_s ..... static pressure, Pa

P_t ..... total pressure, Pa

q'' ..... heat flux from blade surface, W/m^2

Re ..... Reynolds number, $\frac{\rho_\infty U_\infty L_{ref}}{\mu_\infty}$

s ..... surface arc length, m

U ..... streamwise velocity, m/s

U_{in} ..... inlet velocity, m/s

U_{exit} ..... exit velocity, m/s

U_∞ ..... freestream velocity, m/s

γ ..... intermittency factor

ε ..... turbulent dissipation rate, $-\frac{dk}{dt}$,m^2/s^3

θ ..... momentum thickness

ρ_∞ ..... freestream density, kg/m^3

μ_∞ ..... freestream molecular viscosity, Pa-s

μ_t ..... eddy viscosity

v ..... kinematic viscosity, $\frac{\mu}{\rho}$, m^2/s

ω ..... turbulent eddy frequency, s^{-1}

ω_{loss} ..... loss coefficient, $\frac{P_{in}-P_{total}}{P_{in}}$

k ..... turbulence kinetic energy, m^2/s^2

ε ..... turbulence dissipation rate, m^2/s^3

v_m ..... kinematic eddy viscosity, $\frac{\mu_t}{\rho}$, m^2/s

u' ..... streamwise fluctuation velocity, m/s

v' ..... normal fluctuation velocity, m/s

l ..... turbulence length scale, m

Lu ..... turbulence energy scale, m

LIST OF APPENDIX FIGURES

Figure Page

1. INTRODUCTION AND RESEARCH OBJECTIVES

As new aircraft are developed for higher altitudes and higher speeds while lowering pollution, complex flow conditions are introduced into gas turbine engines. These complex flows include higher turbulence intensities and higher Mach numbers, both of which can increase the levels of heat transfer on the turbine blades (Ames, Wang, & Barbot, 2003). Flight at higher altitudes also results in lower Reynolds numbers. During flight at low Reynolds number conditions, flow separation can occur and turbine efficiency can drop as a result (Glassman, Whitney, & Steward, 1994). This research will explore each of these conditions in detail. When designing components in gas turbine engines, it is much more cost effective to model flows using computational fluid dynamics (CFD) rather than analyzing prototypes in wind tunnels. In order for computational studies of heat transfer and losses to be accurate, designers must have flow models that are capable of detecting transitional and turbulent flow. Current turbulence models are fairly accurate at low turbulence intensities; however, heat transfer is usually over predicted as turbulence intensities and Reynolds numbers rise. The model used in this research is the γ-Re_θ transition model, which has proven to accurately capture the results of transitional flows over a wide range of flow characteristics. Unfortunately, heat transfer calculations are over predicted with this model when turbulence intensities and Reynolds numbers increase.

The goal of this research is to implement changes to the γ-Re_θ transition model that account for increased turbulence levels. Experiments have been done by Dr. Forrest Ames and his research group at the University of North Dakota detailing flows over low pressure turbine blades and vanes. Simulations conducted at NDSU are compared to the experimental results, and the transition model is modified according to any discrepancies found between simulations and

experiments. These cases will be used to test and validate the newly modified γ-Re_θ model. The results from this study will also establish a base for future model refinement and improvement.

2. TURBULENCE AND TRANSITION REVIEW

2.1. Turbulent Flow

When working with any fluid flow, the flow can be laminar, turbulent, or in a transitional state between the two. For most engineering applications, fluid flows are considered to be turbulent. Turbulence describes the random fluctuations in flow properties along with eddy formation and dissipation. The random and chaotic nature of turbulence makes it incredibly difficult for researchers to simulate.

2.1.1. Introduction to Turbulence

The study of turbulence is not at all new, in fact the first documented studies of turbulence go back over 500 years to the sketch books of Leonardo da Vinci. Figure 2.1 below shows da Vinci's famous sketch of turbulence. Along with this sketch he describes turbulence with a surprisingly modern definition (McDonough):

> *"... the smallest eddies are almost numberless, and large things are rotated only by large eddies and not by small ones, and small things are turned by small eddies and large."*

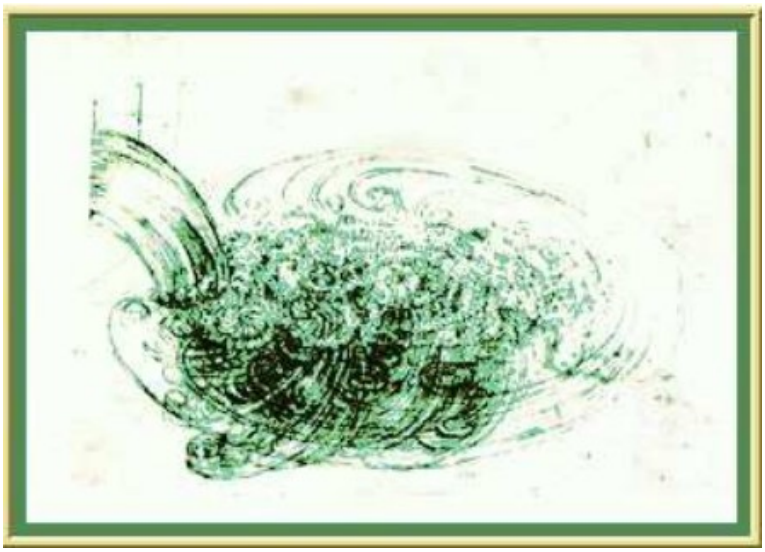

Figure 2.1. Leonardo da Vinci's Sketch of Turbulent Flow (McDonough)

As time moves forward to the present day, there are still unanswered questions in the field of turbulence research. Through many experiments and simulations, researches have gathered a much better picture of the mechanisms of turbulent flow. The current problem in the field of fluid dynamics is the mathematical modeling of turbulent flow. This field of study has rapidly progressed over recent decades due to significant increases in computational power. The goal of the current project is to validate and expand on current turbulence models for turbine flows.

There are many different definitions of turbulence, but perhaps the most basic definition from a fluid mechanics standpoint is a flow that contains random, chaotic behavior of the fluid parameters. These parameters include the three velocity components, shear stresses, temperature, pressure, or any other field variable (Munson, Young, Okiishi, & Huebsch, 2010). This fluctuating behavior is not the only thing that makes up a turbulent flow, however. Frank White suggests that there are several other characteristics that come with turbulent flow in addition to these fluctuations. There will also be eddies of continuously varying sizes from the thickness of the boundary layer down to small fractions of a millimeter. The turbulent motion will be self-sustaining, so once turbulent flow is initiated, new eddies will be produced as others are dissipated, continuing the turbulent trend. Finally, turbulent flows will have mixing characteristics that are much stronger than that of laminar flow. The diffusion of mass, momentum, and energy is significantly increased due to turbulent mixing (White, 2006).

Because turbulence is such a complex topic, turbulence modeling has been extremely difficult for researches. Although significant progress has been made in turbulence simulation, there is a great deal of work to be done in this field.

2.1.2. The Scales of Turbulence

While turbulence is regarded as a random and chaotic phenomenon, it can be quantified in terms of a wide range of eddy sizes, or scales. If an eddy has a length scale, l, and a velocity scale, u, then it has a time scale, l/u. These scales are used to describe the different characteristics of a turbulent flow (Burden, 2008). A continuum approach may still be used when solving problems that involve turbulence because even the smallest scales in a turbulent flow are still much larger than any molecular length scale (Tennekes & Lumley, 1972). Figure 2.2 below shows an example of the varying eddy sizes in a turbulent flow.

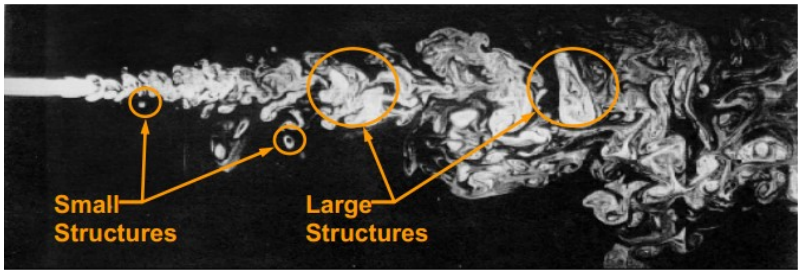

Figure 2.2. Eddy Size Variation in a Turbulent Flow (ANSYS , 2010)

Turbulent flow consists of a continuous range of scales. Turbulence is dominated by the largest eddies, which are considered to be the energy carrying eddies. These larger eddies are responsible for the enhanced diffusivity and added stresses of a turbulent flow. Turbulent eddies are dissipative by nature, but the largest eddies can persist for distances up to 30 times the width of the flow. Because of this, a turbulent flow requires knowledge of the upstream history before the state of the flow can be solved at a downstream location (Wilcox, 2006).

As the turbulence decays, energy transfers from the larger eddies to smaller ones. The smallest eddies then dissipate into heat by means of molecular viscosity. It can be inferred from these mechanisms that turbulence is always dissipative by nature. In a 1941 publication by Andrei Kolmogorov, a dimensional analysis technique was implemented to estimate the smallest

turbulence scales. Kolmogorov's theory, called the universal equilibrium theory, stated that the smallest eddies should be in a state in which the rate of energy received from larger eddies is equal to the rate that the energy is dissipated to heat (Kolmogorov, 1941). From this theory, the smallest scales should only depend on the rate that energy is supplied by the larger eddies, ε, and the kinematic viscosity, ν. Based on these two variables, characteristic scales of length, time, and velocity are given below in equation (2.1).

$$\eta \equiv \left(\frac{\upsilon^3}{\varepsilon}\right)^{\frac{1}{4}}, \qquad \tau \equiv \left(\frac{\upsilon}{\varepsilon}\right)^{\frac{1}{2}}, \qquad \nu \equiv (\upsilon\varepsilon)^{\frac{1}{4}} \tag{2.1}$$

These equations are known as the Kolmogorov scales of length, time, and velocity. To provide an example of how small the Kolmogorov length scale really is, consider an air flow at 65 mph. The Kolmogorov length scale is of the order $(10)^{-4}$, which is still hundreds of times greater than the molecular diameter. For this reason, the continuum approach is valid for turbulence modeling (Wilcox, 2006).

2.1.3. Governing Equations of Fluid Flow

Before any turbulence modeling discussion can take place, the equations that govern all fluid motion must be discussed. There are three physical phenomena that the governing equations are derived from: the conservation of mass, the conservation of momentum, and the conservation of energy. The conservation of mass equation is often referred to as the continuity equation, and it physically means that mass can neither be created nor destroyed. There are three equations that make up the momentum equations—one for each direction. These momentum equations are referred to as the Navier-Stokes equations, which are named after the two scientists who derived them. The momentum equations are derived from Newton's second law, which states that force is equal to the product of an object's mass and acceleration. One additional

equation governs the conservation of energy. This brings the total number of governing equations for any fluid flow up to five. Equation (2.2) below is the complete mass conservation equation, and equations (2.3), (2.4), and (2.5) are the x, y, and z momentum conservation equations.

$$\frac{\partial \rho}{\partial t} + \left[\frac{\partial(\rho u)}{\partial x} + \frac{\partial(\rho v)}{\partial y} + \frac{\partial(\rho w)}{\partial z}\right] = 0 \tag{2.2}$$

$$\frac{\partial u}{\partial t} + u\frac{\partial u}{\partial x} + v\frac{\partial u}{\partial y} + w\frac{\partial u}{\partial z} = \frac{1}{\rho}\left[-\frac{\partial p}{\partial x} + \frac{\partial \tau_{xx}}{\partial x} + \frac{\partial \tau_{yx}}{\partial y} + \frac{\partial \tau_{zx}}{\partial z}\right] \tag{2.3}$$

$$\frac{\partial v}{\partial t} + u\frac{\partial v}{\partial x} + v\frac{\partial v}{\partial y} + w\frac{\partial v}{\partial z} = \frac{1}{\rho}\left[-\frac{\partial p}{\partial y} + \frac{\partial \tau_{xy}}{\partial x} + \frac{\partial \tau_{yy}}{\partial y} + \frac{\partial \tau_{zy}}{\partial z}\right] \tag{2.4}$$

$$\frac{\partial w}{\partial t} + u\frac{\partial w}{\partial x} + v\frac{\partial w}{\partial y} + w\frac{\partial w}{\partial z} = \frac{1}{\rho}\left[-\frac{\partial p}{\partial z} + \frac{\partial \tau_{xz}}{\partial x} + \frac{\partial \tau_{yz}}{\partial y} + \frac{\partial \tau_{zz}}{\partial z}\right] \tag{2.5}$$

These equations can be condensed and rewritten into vector form. They then take the form of

$$\frac{D\rho}{Dt} + \rho \operatorname{div} \boldsymbol{V} = 0 \tag{2.6}$$

$$\rho\frac{D\boldsymbol{V}}{Dt} = \rho g - \nabla p + \frac{\partial}{\partial x_j}\left[\mu\left(\frac{\partial v_i}{\partial x_j} + \frac{\partial v_j}{\partial x_i}\right) + \delta_{ij}\lambda\, div\, \mathbf{V}\right] \tag{2.7}$$

Several simplifications can be made to these equations depending on flow characteristics. For a potential flow, which is assumed to be incompressible and inviscid, the density (ρ) and viscosity (μ) terms are constant. These assumptions reduce the governing equations down to a much simpler form. (White, 2006). The simplified continuity and the Navier-Stokes equations are shown below with the assumption of an incompressible flow:

$$\text{div}\,\mathbf{V} = 0 \tag{2.8}$$

$$\rho\frac{D\boldsymbol{V}}{Dt} = \rho g - \nabla p + \mu\nabla^2\mathbf{V} \tag{2.9}$$

The final governing equation, the conservation of energy, is shown below:

$$\rho\frac{D}{Dt}\left(e + \frac{p}{\rho}\right) = \frac{Dp}{Dt} + \text{div}(k\nabla T) + \tau'_{ij}\frac{\partial u_i}{\partial x_j} \tag{2.10}$$

The conservation of energy is derived from the 1st law of thermodynamics, which states that if work and heat are added to a system, the energy in the system will also increase. Several simplifications can also be made to the energy equation depending on the flow type. Instead of using the internal energy variable, enthalpy can be used instead. Enthalpy is related to internal energy by the following equation:

$$h = \left(e + \frac{p}{\rho}\right) \tag{2.11}$$

This substitution is made because enthalpy is often a more useful variable in fluid flows.

The energy equation can be further simplified by collecting the last term in equation (2.10) and calling it the dissipation function, Φ. This function is given below:

$$\Phi = \tau'_{ij}\frac{\partial u_i}{\partial x_j} \tag{2.12}$$

The full energy equation is now given by

$$\rho\frac{Dh}{Dt} = \frac{Dp}{Dt} + \text{div}(k\nabla T) + \Phi \tag{2.13}$$

If a flow is traveling with a low velocity, it can be considered incompressible. If this is the case, equation (2.13) can be simplified and written in terms of thermodynamic properties. This simplified equation is given below:

$$\rho c_p \frac{DT}{Dt} \approx \text{div}(k\nabla T) \tag{2.14}$$

If a constant thermal conductivity is assumed, the energy equation can be simplified even further. This following equation is referred to as the incompressible heat-convection equation (White, 2006):

$$\rho c_p \frac{DT}{Dt} \approx k\nabla^2 T \tag{2.15}$$

The three principle equations discussed in this section in this section govern all fluid flows. In the world of computational fluid dynamics, every flow model is based on the principals that mass, momentum, and energy must be conserved.

2.1.4. Reynolds-Averaged Equations

Because turbulence exhibits random and chaotic fluctuations of flow characteristics, the flow variables can hold different values at a given location as time progresses. Figure 2.3 below shows an example of velocity profile fluctuations on a flat plate. These fluctuations are not limited to velocity profiles, however.

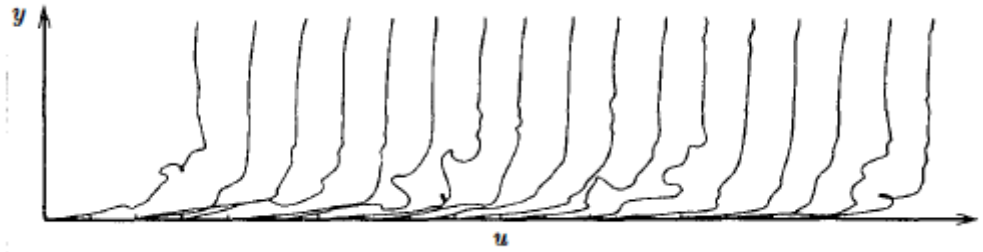

Figure 2.3. 17 Different Instances of a Velocity Profile at the Same Location on a Flat Plate (Wilcox, 2006)

Due to the fluctuating nature of the turbulent variables, a statistical approach is taken to solve the governing equations. The most common type of statistical averaging was given by Osborn Reynolds in 1895, and this approach is still used as the basis for many current turbulence models today. This method is referred to as Reynolds averaging, where all flow variables are given by the sum of mean and fluctuating components. In other words,

$$u(x) = \bar{u}(x) + u'(x) \tag{2.16}$$

where u is any turbulent variable, $\bar{u}$ is the average component of u, and u' is the fluctuating component of u. When the Navier Stokes equations are expanded into mean and fluctuating components of velocity, there are some additional terms that appear in the equations. These additional terms are called momentum fluxes, and they act as apparent stresses throughout the flow. These stresses represent new unknowns into the Navier Stokes equations, so additional equations are required to solve. With the addition of new equations, there are even more unknowns introduced. The challenge of creating enough equations to represent each of the unknowns in the Navier Stokes equations is called the "Turbulent Closure Problem".

Figure 2.4 below shows a sample of boundary layer velocity profiles at a given location with an instantaneous snapshot versus the average flow profile. The fluctuations in a turbulent boundary layer are too large to be ignored, so the Reynolds averaging technique is implemented

to simplify the problem. When Reynolds averaged equations are used, the average velocity profile is considered, and the velocity fluctuations are buried in the new stress term called Reynolds stresses.

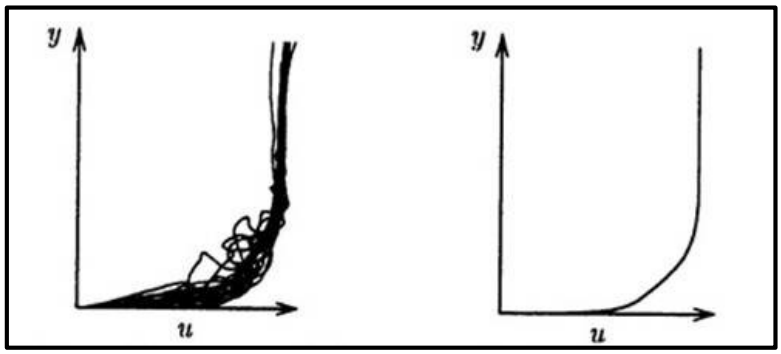

Figure 2.4. Instantaneous and Average Boundary Layer Velocity Profiles (Wilcox, 2006)

Similarly, Figure 2.5 below shows a velocity contour for an instantaneous snapshot of the flow against a time-averaged contour of the flow. In most engineering applications, the average flow characteristics are sufficient, so statistical averaging techniques provide a useful way to approach turbulence modeling.

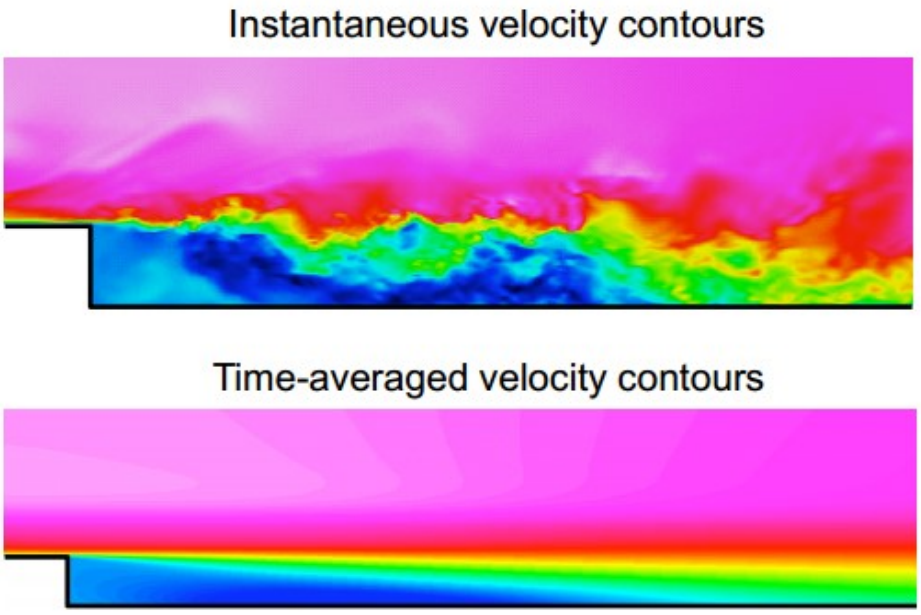

Figure 2.5. Instantaneous vs Time-averaged Velocity Contours (ANSYS , 2010)

There are three forms of Reynolds averaging in turbulence modeling research. These are the time average, spatial average, and ensemble average. (Wilcox, 2006). Time averaging is used for stationary turbulence, the most common type of turbulence for engineering applications. Figure 2.5 above was obtained using time averaging. If $f(x,t)$ is an instantaneous flow variable, then its time average, $F_T(x)$, is defined by

$$F_T(x) = \lim_{T\to\infty} \frac{1}{V} \int_t^{t+T} f(x,t)dt \tag{2.17}$$

Spatial averaging is used for homogenous turbulence, which is turbulence that is uniform in all directions on average. Spatial average can be completed by doing a volume integral in all directions. If $f(x,t)$ is an instantaneous flow variable, then its spatial average, F_V, is given by

$$F_V(t) = \lim_{V\to\infty} \frac{1}{V} \iiint_V f(x,t)dV \tag{2.18}$$

Ensemble averaging is used for flows that decay with time. It is the most general type of Reynolds averaging. (Wilcox, 2006). If N experiments are performed with identical boundary and initial conditions where $f(x,t) = f_n(x,t)$ in the n^{th} experiment, then ensemble average, F_E, is given by

$$F_E(x,t) = \lim_{N\to\infty} \frac{1}{N} \sum_{n=1}^{N} f_n(x,t) \tag{2.19}$$

The time averaging technique applies best to the turbine flows that are analyzed with this project, so this will be the only technique discussed moving forward. The equation development below will show how the conservation equations can be time averaged for simplification. Equations (2.20) and (2.21) below show for the conservation of mass and momentum for an incompressible flow.

$$\frac{\partial u_i}{\partial x_i} = 0 \tag{2.20}$$

$$\rho \frac{\partial u_i}{\partial t} + \rho u_j \frac{\partial u_i}{\partial x_j} = -\frac{\partial p}{\partial x_i} + \frac{\partial t_{ji}}{\partial x_j} \tag{2.21}$$

where u_i is velocity, x_i is position, t is time, p is pressure, ρ is density, and t_{ij} is the viscous stress tensor given by

$$t_{ij} = 2\mu s_{ij} \tag{2.22}$$

where μ is molecular viscosity and s_{ij} is the strain rate tensor,

$$s_{ij} = \frac{1}{2}\left(\frac{\partial u_i}{\partial x_j} + \frac{\partial u_j}{\partial x_i}\right) \tag{2.23}$$

To simplify the Reynolds averaging process, the convective terms are re-written in conservation form. For example,

$$u_j \frac{\partial u_i}{\partial x_j} = \frac{\partial}{\partial x_j}(u_j u_i) - u_i \frac{\partial u_j}{\partial x_j} = \frac{\partial}{\partial x_j}(u_j u_i) \tag{2.24}$$

After simplifying and rewriting the convective terms in conservation form, the Navier-Stokes equation becomes

$$\rho \frac{\partial u_i}{\partial t} + \rho \frac{\partial}{\partial x_j}(u_j u_i) = -\frac{\partial p}{\partial x_i} + \frac{\partial}{\partial x_j}(2\mu s_{ji}) \tag{2.25}$$

When the velocity components of the continuity equation (2.20) and Navier Stokes equation (2.25) are time averaged, the Reynolds averaged equations of motion are obtained and they are as follows:

$$\frac{\partial U_i}{\partial x_i} = 0 \tag{2.26}$$

$$\rho \frac{\partial U_i}{\partial t} + \rho \frac{\partial}{\partial x_j}\left(U_j U_i - \overline{u_j' u_i'}\right) = -\frac{\partial P}{\partial x_i} + \frac{\partial}{\partial x_j}\left(2\mu S_{ji}\right) \tag{2.27}$$

The instantaneous components of the velocity don't show up in the time averaged continuity equation, so there is nothing out of the ordinary when solving this equation. The Navier Stokes equation, on the other hand, has a new term introduced in terms of the fluctuating velocity components. The correlation $\overline{u_j' u_i'}$ is introduced, and solving for this correlation requires an additional equation. Modeling this term is the fundamental problem of turbulence modeling. To find all of the mean flow properties of the turbulent flow, a method for calculating $\overline{u_j' u_i'}$ is required.

A more popular form of the time averaged Navier Stokes equation is given below in equation (2.28).

$$\rho \frac{\partial U_i}{\partial t} + \rho U_j \frac{\partial U_i}{\partial x_j} = -\frac{\partial P}{\partial x_i} + \frac{\partial}{\partial x_j}\left(2\mu S_{ji} - \rho \overline{u_j' u_i'}\right) \tag{2.28}$$

This equation is referred to as the Reynolds-Averaged Navier-Stokes, or RANS, equation. The term $-\rho \overline{u_j' u_i'}$ is called the Reynolds-stress tensor and is denoted by $\rho \tau_{ij}$, where τ_{ij} is the specific Reynolds stress tensor given by (Wilcox, 2006).

$$\tau_{ij} = -\overline{u_i' u_j'} \tag{2.29}$$

This is a symmetric tensor, so $\tau_{ij} = \tau_{ji}$, and it has 6 independent components. Unfortunately, the process of time averaging added 6 unknowns to the problem, but it didn't add any new equations. At this point, there are ten unknowns and only four equations to solve them. This turbulence

closure problem introduces the need for turbulence modeling. The primary goal of turbulence modeling research is to develop accurate relationships that satisfy the Navier Stokes equations. (Wilcox, 2006).

2.2. Laminar to Turbulent Flow Transition

Up to this point, the discussion has been limited to turbulent flow. However, this research project focuses on flows over low pressure turbine sections, which are not always fully turbulent. Low pressure turbines often have extended regions of transitional flow that must be considered in design. Unfortunately, the prediction of transition is very difficult because flow stability theory predicts the end of laminar flow, but it doesn't predict the onset of turbulent flow. There is no theory of transition, only experimental correlations (White, 2006). Large strides have been made in the prediction of transitional flow, but much of the transition process remains a mystery to predict. From basic fluid mechanics, it is known that flow can transition at a critical Reynolds number, but this Reynolds number doesn't give any information about the flow characteristics during transition. The flow characteristics are influenced by many factors, the most important being the pressure distribution from the outer flow, the wall roughness and curvature, and the free stream turbulence intensity (Schlichting, 1979). There have been four main approaches to tackling the problem of predicting transition: Mayle's correlation of spot production rate based on acceleration parameters and the free stream turbulence levels, correlations by Gostelaw based on a pressure gradient parameter, correlations based on stability theory developed by Walker, and correlations in terms of turbulence intensity from Narasimha (Walker, 1993). One of the primary goals for the current research project is to validate commercially available transition models and offer suggestions for improvement in low pressure turbine flows.

2.2.1. Modes of Transition

When a flow reaches a critical point where it can longer remain a stable laminar flow, it can transition to turbulent flow by several different transition mechanisms. These modes of transition are natural, bypass, separated flow, periodic-unsteady, and reverse transition (Mayle, 1991).

2.2.1.1. Natural Transition

When a flow reaches a critical state where it can no longer remain laminar, several phases take place before the flow becomes fully turbulent. First, the boundary layer forms small instabilities called 2-D Tollmien Schlichting waves. These instabilities then grow into three dimensional vortices. As the vortices break down, turbulent spots form and they are spread downstream until fully turbulent flow is developed (Mayle, 1991). This process of transition is shown below in Figure 2.6.Figure 2.7

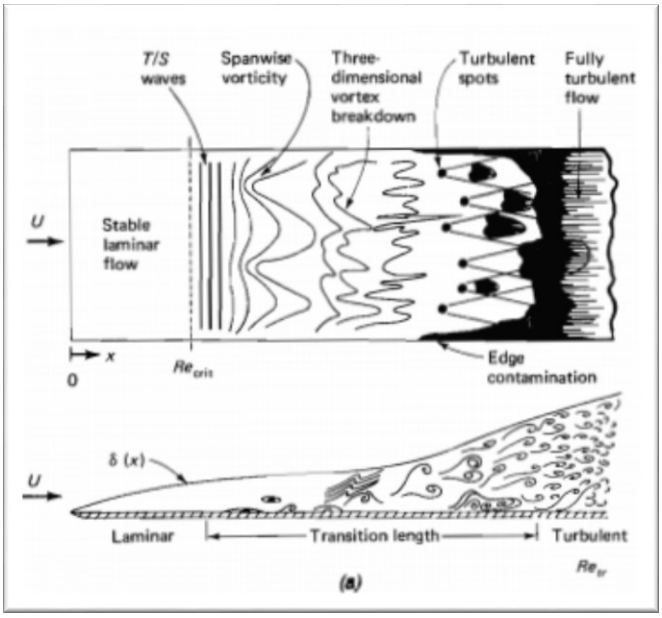

Figure 2.6. Steps of Natural Transition (White, 2006)

2.2.1.2. Bypass Transition

When a flow has a high free stream turbulence intensity, the first stages of natural transition can be completely bypassed. A laminar flow will form turbulent spots in the boundary layer, and the flow becomes turbulent without the formation of T-S waves (Mayle, 1991).

2.2.1.3. Separated-Flow Transition

If a flow separates from the surface, transition can occur in the free-shear layer near the surface. Once the flow becomes turbulent, it can reattach to the surface. This separation and reattachment forms a bubble on part of the surface. The separated transition is very common in gas turbine engines. The flow can separate in high speed regions on the suction surface of an airfoil where the pressures are low. The flow can also separate near an airfoil's leading edge. Figure 2.7 below shows how flow transitions from laminar to turbulent over a separation bubble.

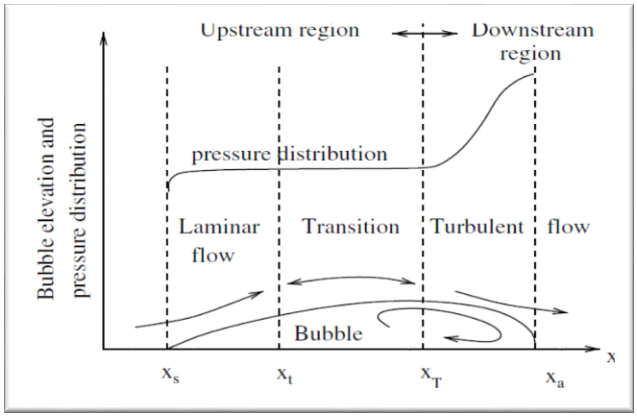

Figure 2.7. Transitional Flow over a Separation Bubble (Mayle, 1991)

As the flow transitions over a separation bubble, it can go through all the phases of natural transition, depending on the turbulence levels in the free stream.

Separated flow transition is an important thing to consider in airfoil design. Large separation bubbles can cause significant aerodynamic losses in turbines. Short separation bubbles can force the flow to become turbulent and give designers more control on performance (Mayle,

1991). Modeling these types of flows is something that needs much more development. The present research focuses primarily on separated flow transition and how it can be predicted accurately.

2.2.1.4. Periodic-Unsteady Transition

The rotational nature of a gas turbine engine causes wakes to be passed downstream from each turbine in a periodic manner. These wakes can each induce an unsteady turbulent flow downstream. This can pose difficulties for designers because at any point in time, the flow could be laminar at a given location, but due to the periodic nature of the flow, it could be turbulent at another time.

2.2.1.5. Reverse Transition

The modes of transition discussed thus far occur when flow transitions from laminar to turbulent, but the reverse can also occur. This process is called relaminarization or reverse transition. This type of transition can occur when a flow goes through a strong acceleration through a nozzle. Since the airfoils in a gas turbine engine generate flows with high levels of acceleration, reverse transition is very possible. In general, this relaminarization can occur on an airfoil under low free stream turbulence levels (Mayle, 1991).

2.2.2. Factors Affecting Flow Transition

There are several different flow characteristic that can affect the onset of transition. These factors include pressure gradients, turbulence conditions, surface characteristics, flow speeds, and heat transfer levels. One of the goals of this project was to simulate the flow over a given airfoil while manipulating turbulence intensity and flow speed (compressibility) to investigate the effects on transition.

2.2.2.1. Pressure Gradient

Pressure gradient plays a role in the onset of transition when the free stream turbulence levels are relatively low. In gas turbines, the dominating factor that affects transition is the turbulence level (Mayle, 1991). As the turbulence levels decrease, a favorable pressure gradient will decrease the production rate of turbulent spots, effectively delaying the transition to turbulent flow. Experiments have shown that as the pressure gradient becomes more and more adverse, turbulent spot production increases, and the onset of transition occurs much sooner. It was also found that the length of the transition flow region is shorter under an adverse pressure gradient. In other words, the flow goes from laminar to turbulent with very almost no transitional region between (Gostelow, Blunden, & Walker, 1994).

2.2.2.2. Free Stream Turbulence

When designing a gas turbine engine, it is important to consider higher levels of freestream turbulence. Within the gas turbine, the turbulence level is the most dominant factor on the characteristics of flow transition. Previous research has shown that the production of turbulent spots increases with increased free stream turbulence levels. Because of this increase, transition is more likely to begin sooner. At higher turbulence levels, the transition length also shortens. (Gostelow, Blunden, & Walker, 1994) (Mayle, 1991).

2.2.2.3. Compressibility

When a flow is supersonic, the compressibility can have an effect on the characteristics of transition. The shockwaves that come with supersonic flows can also affect flow transition. Research on the compressibility effects on transition is very limited to this day, but the general trend that has been found is that spot production is decreased with an increasing Mach number, and therefore transition is delayed with increased Mach numbers (Mayle, 1991).

2.2.2.4. Surface Roughness

As one might expect, surface roughness can change the transition Reynolds number. A smooth surface corresponds to a later transition location, while a rougher surface would promote transition into turbulence much sooner. Similar to each of the other factors affecting transition to this point, surface roughness plays a larger role on transition onset when the free stream turbulence intensity is lower. The higher turbulence intensities found in gas turbine engines generally allows designers to neglect the effects of roughness on transition (Mayle, 1991).

2.2.2.5. Surface Curvature

The concavity of a surface can also affect the onset of transition. Previous experiments have shown that flows on a concave surface can become unstable due to the centrifugal forces that are encountered. These forces cause the flow to become unstable and undergo transition sooner. When a flow is passing a convex surface, transition can be slightly delayed. At higher free stream turbulence levels, however, the transition occurs exactly like it would on a flat surface (Mayle, 1991).

2.2.2.6. Heat Transfer

The high turbulence levels encountered in a gas turbine engine generally outweigh any heat transfer effects that might affect transition. At lower turbulence levels, however, heat that transfers from the airfoil surface to the surrounding flow field can speed up the process of transition into turbulent flow. Turbine blades are often cooled with a technique called film cooling. This technique involves injecting coolant into the flow from the surface of the airfoil. While this may reduce the heat transferred to the surrounding flow, the process of the injection introduces enough free stream turbulence to cause the flow to become turbulent (Mayle, 1991).

2.2.3. Transition and Turbulence in Turbomachinery Applications

In many fluid flow applications, design is based around the assumption that the flow is completely turbulent. In gas turbine engines, this assumption cannot be made. A significant portion of the turbines can be exposed to laminar, transitional, or turbulent flow, and it is critical that this information be designed around. Figure 2.8 below shows a basic schematic of flow over a turbine. This turbine encounters a significant portion of laminar flow followed by a region of separated flow. The flow then transitions until it reattaches and becomes turbulent.

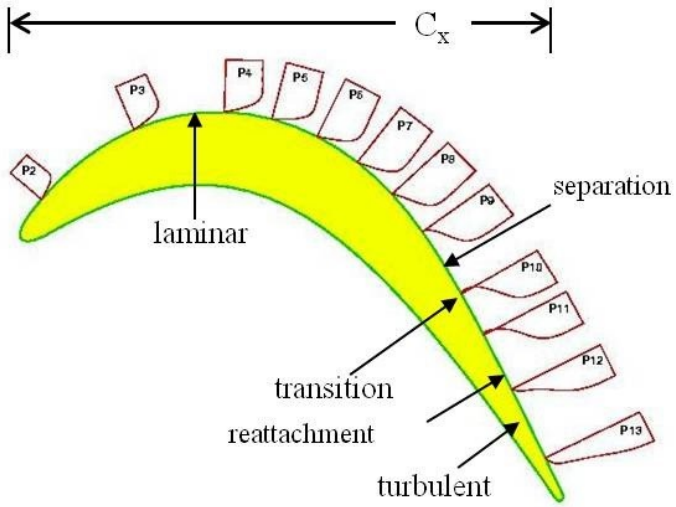

Figure 2.8. Transition over a Separation Bubble on the Suction Surface

While laminar and turbulent flow can be modeled very accurately, transitional flow remains very difficult to model. The low pressure turbine of a gas turbine engine significantly accelerates the flow, and this causes an extended transition region. As discussed previously in section 2.2.2 above, there are many factors that affect transition.

3. TURBULENCE AND TRANSITION MODELING

3.1. Turbulence Modeling

Turbulence and transition both remain very complex phenomena to predict. Using Reynolds averaging techniques discussed above in section 2.1.4 allows researchers to predict the characteristics of turbulent flow in a simplified way with a high level of accuracy. There are several different turbulence models that take advantage of this Reynolds averaging technique, and three common models used in this research will be discussed below.

3.1.1. Model Types

Depending on the flow problem, there are many different turbulence models to choose from. The most basic models are called zero equation models, which are algebraic models. In zero equation models, the eddy viscosity of the fluid is algebraically related to the length scales of the flow. This simple models can be useful and easy to solve, but higher order models are much more accurate. There are several "one equation" models which use a single differential equation to calculate the turbulence kinetic energy in the flow field. The eddy viscosity is obtained from this energy transport equation, and the turbulent flow field can be resolved. While the one equation models are more accurate than algebraic models, they are more computationally expensive to solve. With the rapid growth of computer power in today's world, it is becoming much more realistic to use two equation models, or even higher order models that can model turbulence very accurately. This project relies on two very common two-equation models that will be discussed in more detail below.

3.1.1.1. *k-ε* Models

For many years, the k-ε turbulence model was perhaps the most common of all two equation models. There are many variations of the k-ε model, but the standard model will be

described here. The idea of this model is to calculate the turbulence kinetic energy along with the eddy dissipation rate at every location in the flow field. With these variables, the eddy viscosity can be calculated by the following equation.

$$\nu_t = C_\mu \frac{k^2}{\epsilon} \tag{3.1}$$

where C_μ is a constant. The following equations show the transport of turbulence kinetic energy and turbulence eddy dissipation rate (Wilcox, 2006):

$$\frac{\partial k}{\partial t} + U_j \frac{\partial k}{\partial x_j} = \tau_{ij} \frac{\partial U_i}{\partial x_j} - \varepsilon + \frac{\partial}{\partial x_j}\left[\left(\nu + \frac{\nu_t}{\sigma_\varepsilon}\right)\frac{\partial k}{\partial x_j}\right] \tag{3.2}$$

$$\frac{\partial \varepsilon}{\partial t} + U_j \frac{\partial \varepsilon}{\partial x_j} = C_{\varepsilon 1} \frac{\varepsilon}{k} \tau_{ij} \frac{\partial U_i}{\partial x_j} - C_{\varepsilon 2} \frac{\varepsilon^2}{k} + \frac{\partial}{\partial x_j}\left[\left(\nu + \frac{\nu_t}{\sigma_\varepsilon}\right)\frac{\partial \varepsilon}{\partial x_j}\right] \tag{3.3}$$

Where the closure coefficients are defined as

$$C_{\varepsilon 1} = 1.44; \quad C_{\varepsilon 2} = 1.92; \quad C_\mu = 0.09; \quad \sigma_\varepsilon = 1.0; \quad \sigma_\varepsilon = 1.3 \tag{3.4}$$

Many modifications of this model exist for different applications. Modifications may include different closure coefficients or additional terms to incorporate different flow properties like wall effects or compressibility effects.

3.1.1.2. *k-ω* Models

The k-ω model is set up very similarly to the k-ε model in that it is a model which uses two transport equations to solve for the eddy viscosity of the flow field. In this case, the two transport equations are solving for the kinetic energy (k) of the flow and the dissipation per unit turbulence kinetic energy (ω) of the flow. This model calculates eddy viscosity in the flow field with the following equation (Wilcox, Turbulence Modeling for CFD, 2006):

$$\nu_t = \frac{k}{\bar{\omega}}; \qquad \bar{\omega} = \max(\omega, C_{lim}\sqrt{\frac{2S_{ij}S_{ij}}{\beta^*}}); \quad C_{lim} = \frac{7}{8} \tag{3.5}$$

The following equations show the transport of the kinetic energy and the specific dissipation rate:

$$\frac{\partial k}{\partial t} + U_j\frac{\partial k}{\partial x_j} = \tau_{ij}\frac{\partial U_i}{\partial x_j} - \beta^* k\omega + \frac{\partial}{\partial x_j}\left[\left(\nu + \sigma^*\frac{k}{\omega}\right)\frac{\partial k}{\partial x_j}\right] \tag{3.6}$$

$$\frac{\partial \omega}{\partial t} + U_j\frac{\partial \omega}{\partial x_j} = \alpha\frac{\omega}{k}\tau_{ij}\frac{\partial U_i}{\partial x_j} - \beta\omega^2 + \frac{\sigma_d}{\omega}\frac{\partial k}{\partial x_j}\frac{\partial \omega}{\partial x_j} + \frac{\partial}{\partial x_j}\left[\left(\nu + \sigma\frac{k}{\omega}\right)\frac{\partial \omega}{\partial x_j}\right] \tag{3.7}$$

Where the closure coefficients are

$$\alpha = \frac{13}{25}; \quad \beta = \beta_0 f_\beta; \quad \sigma = \frac{1}{2}; \quad \beta^* = \frac{9}{100}; \quad \sigma^* = \frac{3}{5}; \quad \sigma_{d0} = \frac{1}{8} \tag{3.8}$$

$$\sigma_d = \begin{cases} 0, & \frac{\partial k}{\partial x_j}\frac{\partial \omega}{\partial x_j} \le 0 \\ \sigma_{d0}, & \frac{\partial k}{\partial x_j}\frac{\partial \omega}{\partial x_j} > 0 \end{cases} \tag{3.9}$$

$$\beta_0 = 0.0708; \quad f_\beta = \frac{1 + 85\chi_\omega}{1 + 100\chi_\omega}; \quad \chi_\omega = \left|\frac{\Omega_{ij}\Omega_{jk}S_{ki}}{(\beta^*\omega)^3}\right|; \tag{3.10}$$

Ω_{ij} and S_{ij} are the mean-rotation and mean-strain-rate tensors, respectively. These quantities are given by

$$\Omega_{ij} = \frac{1}{2}\left(\frac{\partial U_i}{\partial x_j} - \frac{\partial U_j}{\partial x_i}\right); \qquad S_{ij} = \frac{1}{2}\left(\frac{\partial U_i}{\partial x_j} + \frac{\partial U_j}{\partial x_i}\right) \tag{3.11}$$

Like the k-ε model, the k-ω has undergone many changes since its beginning in the 1970s. To this day, the model continues to change as new developments become available with

higher powered computers. The current model presented in this section is capable of predicting shock-separated flows without the need of adding compressibility corrections. It can also predict flows with attached boundary layers, or mildly separated flows. Overall, the k-ω model is a very robust model with many applications in the gas turbine industry.

3.1.1.3. Shear Stress Transport Model

The Shear Stress Transport (SST) turbulence model that is based from the k-ω equations. It is a two equation eddy viscosity model that combines the benefits of the k-ω and k-ε models together. This SST model behaves very well with adverse pressure gradients and separated flows. It has been validated with many standard engineering flow data, and for these reasons, it is the model that is used in this research.

The SST turbulence model switches between the k-ε and k-ω model based on a blending function that is governed by distance to the nearest wall. The model coefficients change based on wall distance, effectively blending the models together. For areas closest to the wall, the original Wilcox k-ω coefficients are implemented. As the wall distance increases into the freestream flow, the standard k-ε coefficients are used. This switching of coefficients allows researchers to obtain the accurate results given by the k-ω model without having the free stream sensitivity. The coefficient blending function is given by Menter (Menter, 1994):

$$\phi = F_1\phi_1 + (1 - F_1)\phi_2 \tag{3.12}$$

where ϕ_1 represents any constant in the original k-ε model, ϕ_2 represents the same corresponding constant in the k-ω model, and F_1 is a blending function based on the distance from the nearest wall. ϕ then represents the corresponding constant for the new SST model.

The key improvement of the SST model from an aerodynamic perspective is that it accounts for the transport of the turbulent shear stresses. The inclusion of these shear stress terms

in the model are what make it behave so well in adverse pressure gradient flows. The second improvement of the SST model is its definition of eddy viscosity given here:

$$\nu_t = \frac{a_1 k}{max(a_1 \omega; \Omega F_2)} \tag{3.13}$$

where a_1 is a constant, Ω is a measure of the strain rate, and F_2 is a blending function that equals 1 for boundary layer flows and 0 for free shear layers. This new eddy viscosity formulation more accurately predicts adverse pressure gradient flows (Wilcox, 2006) (Menter, 1994).

3.1.1.4. Modified k-ε Turbulence Model Development

One of the primary goals of this project was to implement modifications to the default turbulence models to improve the results. To accommodate the effects of high turbulence intensity, Ames et al. developed an algebraic turbulence model (Ames F. E., 1999). This algebraic model works well in the outer regions of the boundary layer, but fails near the wall. To accommodate for the effects near the wall, the algebraic turbulence model is coupled with a mixing length model by means of a natural blending function. Implementing the mixing length model near the wall ensures appropriate log law behavior in the inner regions of the boundary layer. The goal of this project was to take the ideas of the algebraic turbulence model and apply them to the Shear Stress Transport model in the ANSYS CFX software. The damping function was to be applied to the k-ε portion of the SST model, which captures the flow effects away from the wall. Because the turbulence models in this software are somewhat restricted, a study was done strictly on the k-ε model instead. A test was completed with the mixing length model to verify whether or not the turbulence models in CFX could be modified with positive results. The development of the mixing length model, which stems from the k-ε model, is given below (Ames & Kwon, 1996):

The original k-ε model defines eddy viscosity as

$$\nu_{m=C_\mu \frac{k^2}{\varepsilon}} \tag{3.14}$$

Where Cμ = 0.0945

At this point, the turbulent kinetic energy (k) and turbulent eddy dissipation (ε) need to be resolved.

The standard definition of k is

$$k = \frac{1}{2}(u'^2 + v'^2 + w'^2) \tag{3.15}$$

If an isotropic turbulence condition is assumed,

$$\overline{u'^2} = \overline{v'^2} = \overline{w'^2} \tag{3.16}$$

Substituting this into the k equation above, a relationship between k and u' is developed.

$$k = \frac{3}{2}\overline{u'^2} \tag{3.17}$$

Solving for the fluctuating velocity component,

$$u' = v' = w' = \sqrt{\frac{2}{3}k} \tag{3.18}$$

Based on these definitions, a new mixing length model for eddy viscosity has been proposed, the *v'l* model:

$$\nu_{m=v'l} \tag{3.19}$$

Where *l* is the turbulence length scale and *v'* is the fluctuating component of the velocity normal to the streamwise direction.

From the previous formulation,

$$v' = \sqrt{\frac{2}{3}k} \tag{3.20}$$

The length scale for the *v'l* model is given as

$$l = C_{\mu}\sqrt{\frac{3}{2}}\frac{k^{\frac{3}{2}}}{\varepsilon} \tag{3.21}$$

To account for the effects near the walls, a damping function based on the curve of $\frac{v'^2}{v_{\infty}{}'^2}$ vs. $\frac{y}{Lu}$ was developed. The proposed damping function is

$$(1 - e^{\frac{-2.9y}{Lu}})^{\frac{2}{3}} \tag{3.22}$$

Where *y* is the normal distance from the wall and Lu is the turbulence energy scale defined as

$$Lu = 1.5\frac{u'^3}{\varepsilon} \tag{3.23}$$

Substituting for u',

$$Lu = \sqrt{\frac{2}{3}}\frac{k^{\frac{3}{2}}}{\varepsilon} \tag{3.24}$$

Near the wall, a new expression is formed for the length scale:

$$l = C_{\mu}1.5Lu(1 - e^{\frac{-2.9y}{Lu}})^{\frac{2}{3}} \tag{3.25}$$

Incorporating the near wall effects into the k-ε model, the length scale now becomes

$$l = \min(C_{\mu}\sqrt{\frac{3}{2}}\frac{k^{\frac{3}{2}}}{\varepsilon}, C_{\mu}\sqrt{\frac{3}{2}}\frac{{k_{\infty}}^{\frac{3}{2}}}{\varepsilon_{\infty}}\left(1 - e^{\frac{-2.9y}{\sqrt{\frac{2}{3}}{k_{\infty}}^{\frac{3}{2}}\varepsilon_{\infty}}}\right)) \tag{3.26}$$

Similarly, the *v'* component of the model is defined as

$$v' = \min(\sqrt{\frac{2}{3}k}, \sqrt{\frac{2}{3}k_{\infty}}\left(1 - e^{\frac{-2.9y}{\sqrt{\frac{2}{3}}{k_{\infty}}^{\frac{3}{2}}\varepsilon_{\infty}}}\right)) \tag{3.27}$$

With the turbulence length scale and fluctuating component fully defined, the mixing length model can now be implemented into ANSYS CFX using the built-in CFX Expression Language. Upon successful implementation of this mixing length model, the proposed algebraic turbulence model with a blending function will be implemented into the k-ε portion of the SST model. The goal of this model is to better represent flows with high turbulence levels.

3.1.1.5. Higher Order Modeling Techniques

The two-equation turbulence modeling techniques discussed above are used exclusively in this research. However, with emerging computer technology, there are new techniques that allow researchers to obtain even more accurate results. The k-ε, k-ω, and SST models use Reynolds averaging approximation techniques to obtain closure with the models. To solve the Navier Stokes and continuity equations without Reynolds averaging, Direct Numerical Simulation (DNS) techniques can be implemented. This technique requires that the grid spacing is small enough to resolve the smallest turbulence scales throughout the entire domain. This is the limiting factor of DNS, as current computer technology is still not powerful enough to simulate a flow in a reasonable amount of time. Another technique for highly accurate simulation is the Large Eddy Simulation (LES) in which the smallest eddies in the flowfield are modeled, and the largest eddies are simulated exactly. The idea behind this method is that computational time can

be saved by modeling the smaller eddies because they are less critical in the final solution. A third modeling method is called Detached Eddy Simulation (DES). DES handles large eddies by simulating them exactly, just like LES. However, DES handles thin shear layers and boundary layers with Reynolds averaging techniques. The advantages of this DES technique are that it can produce very accurate results while saving computational time (Wilcox, Turbulence Modeling for CFD, 2006).

These modeling techniques are relatively new in the turbulence field, and they are capable of producing very accurate results. As computer power continues to grow, these techniques will become more and more relevant. For this current research, the computational time is too great, and a two-equation Reynolds averaged model is implemented instead.

3.2. **Transition Modeling using Intermittency**

To this point, the flow modeling discussion has been limited to fully turbulent flow. In the case of gas turbine engines, or more specifically low pressure turbines, a significant portion of the flow can be in a transitional state. To maximize efficiency of the low pressure turbine, it is imperative that the flow is modeled correctly, regardless of the turbulent state it is in. Small increases in turbine efficiency can yield significant fuel savings over the lifespan of an aircraft. The modeling of transition poses a difficult problem in the world of computational fluid dynamics, but predictions are becoming more accurate as computational power grows. The current research project predicts transition by means of an intermittency transport model, which will be detailed in the sections below.

3.2.1. Model Development

A concept of intermittency is employed to predict transitional flows. This intermittency variable, γ, is incorporated into the computations to modify the effective eddy viscosity, $\mu_{t,eff}$, such that

$$\mu_{t,eff} = \gamma \mu_t \tag{3.28}$$

This transition model is coupled with Menter's SST turbulence model to calculate the eddy viscosity along with other turbulence parameters.

The study of intermittency based transition models stems back to the 1950s with experimental data from Dhawan and Narasimha. An empirical intermittency distribution function was developed across a region of flow transition (Dhawan & Narasimha, 1958). Similar correlations were developed in the 1970s through experiments from Chen and Thyson. These experiments improved the intermittency distribution for flows with changing pressure gradients (Chen & Thyson, 1971). Significant improvements to these intermittency correlations have come in the mid-1990s. Based on the work of Chen and Thyson, Solomon et al. have developed an improved method for calculating transitional flows with changing pressure gradients. The model of Solomon is based on the breakdown physics and the rate of turbulent spot production through the transition zone (Solomon, Walker, & Gostelow, 1995).

In 1996, Steelant and Dick developed an intermittency transport equation such that the intermittency distribution of Dhawan and Narasimha was reproduced. This model was coupled with two sets of Navier Stokes equations to predict transitional flows with varying pressure gradients. Unfortunately, this model was developed with two sets of strongly couple equations, and this method is not compatible with existing CFD codes. Today's codes only use a single set

of Navier Stokes equations for solving. Another drawback of this model is its lack of variation of intermittency in the cross-stream direction (Steelant & Dick, 1996).

In 1992, a model from Cho and Chung implemented a three equation k - ε – γ turbulence model. This model explicitly includes intermittency into the standard k – ε that was discussed in section 3.1.1.1 above. This model was not designed to predict flow transition, but it did provide an accurate intermittency distribution in the cross stream direction (Cho & Chung, 1992).

In 1999, Suzen and Huang developed a new transport model for intermittency to combine the best features of the models discussed above. This model reproduces the intermittency distribution of Dhawan and Narasimha, and it also provides a proper variation of intermittency in the cross stream direction. To accomplish this, Steelant and Dick's and Cho and Chung's models were blended. The idea of this model was to be able to predict transitional flow under a range of turbulence intensities and pressure gradients. The intermittency can be implemented into the calculation by using a condition averaged set of Navier Stokes equations. This method can be difficult because the conditioned equations are highly coupled. Instead, the eddy viscosity calculated by a turbulence model is simply multiplied by the intermittency factor to obtain the effective eddy viscosity (Suzen & Huang, 1999).

A series of experiments from Savill called the T3- series cases were designed to test any turbulence model's ability to predict the effects of turbulence intensity on the transition of a laminar boundary layer for varying pressure gradients (Savill, 1993). The transition model showed a good transition behavior for each of these test cases along with the low-pressure turbine experiments of Simon et al. (Simon, Qiu, & Yuan, 2000).

The model developed by Suzen and Huang proved that an intermittency based could reliably be used to predict transition. The difficulty with this model is the additional equation

required to calculate the intermittency. This additional transport equation is solved for the momentum thickness Reynolds number. The momentum thickness Reynold number is used to define the onset criteria in the intermittency equation. This intermittency function is coupled with the SST turbulence model from Menter and Langtry, and it affects the production term of the turbulent kinetic energy downstream of the transition point. In an effort to make the model more generic and compatible with all CFD codes, the model is based only on local variables, so it can be used in unstructured parallel Navier-Stokes solvers (Menter & Langtry, 2012).

The γ-Re_θ model is formulated based on a combination of experimental correlations and locally formulated transport equations. The quantity that triggers the transition process is the strain rate Reynold number, which is defined as follows:

$$Re_v = \frac{\rho y^2}{\mu}\left|\frac{\partial u}{\partial y}\right| = \frac{\rho y^2}{\mu} S \tag{3.29}$$

where y is the distance to the nearest wall and S is the shear strain rate. This strain rate Reynolds number is a local property so it can easily calculated at each grid point, making it compatible with many modern CFD codes. Figure 3.1 below shows a scaled profile of the strain rate Reynolds number for a Blasius boundary layer.

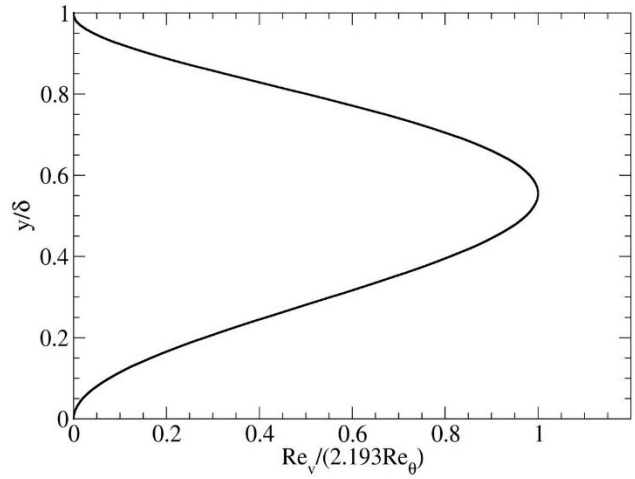

Figure 3.1. Scaled Vorticity Reynolds Number, Re_v, Profile for Blasius Boundary Layer (Menter & Langtry, 2012)

This scaling is implemented so the maximum vorticity Reynolds number in the Blausius boundary layer is one. This is done by dividing the Blausius velocity profile by the corresponding momentum thickness Reynolds number along with a constant, which turns out to be 2.193. With this relationship, it turns out that vorticity Reynolds number and momentum thickness Reynolds number are directly related:

$$Re_\theta = \frac{\max(Re_v)}{2.193} \tag{3.30}$$

This relationship is valid for moderate pressure gradients, as the difference between the actual momentum thickness Reynolds number and the maximum of the vorticity Reynolds number is less than 10%. Based on these relationships, a framework can be built for correlation based transition models (Menter & Langtry, 2012).

3.2.1.1. γ-Re_θ Model Equations

The transition model utilized in this research project is called the γ-Re_θ transition model. It was designed to couple with the Shear Stress Transport turbulence model discussed in section 3.1.1.3 above. This transition model introduces two new variables into the flowfield:

intermittency (γ) and momentum thickness Reynold number (Re_θ). Each of these variables is governed by a transport equation that is solved everywhere in the flowfield. The intermittency variable is used to determine whether or not the flow is laminar, turbulent, or somewhere in between. If the intermittency is zero, the flow is laminar. If the intermittency value is one, the flow is turbulent. If the intermittency carries any value between zero and one, the flow is considered transitional, and the γ-Re_θ transition model accounts for this (Menter & Langtry, 2012). The development of this transitional model is given below.

The transport equation for the intermittency, γ, is given by

$$\frac{\partial(\rho\gamma)}{\partial t}+\frac{\partial(\rho U_j\gamma)}{\partial x_j}=P_\gamma-E_\gamma+\frac{\partial}{\partial x_j}\left[\left(\mu+\frac{\mu_t}{\sigma_f}\right)\frac{\partial\gamma}{\partial x_j}\right] \tag{3.31}$$

where the transition sources, P_γ, are given by

$$P_\gamma=F_{length}c_{a1}\rho S[\gamma F_{onset}]^{0.5}(1-c_{e1}\gamma) \tag{3.32}$$

where S is the strain rate magnitude and F_{length} is an empirical correlation that controls the length of transition. The destruction/relaminarization source, E_γ, is defined as:

$$E_\gamma=c_{a2}\rho\Omega\gamma F_{turb}(c_{e2}\gamma-1) \tag{3.33}$$

where Ω is the vorticity magnitude. The onset of transition is controlled by the following functions:

$$Re_V=\frac{\rho y^2 S}{\mu} \tag{3.34}$$

$$F_{onset\,1}=\frac{Re_v}{2.193\,Re_{\theta c}} \tag{3.35}$$

$$F_{onset\,2}=min(max(F_{onset\,1},F^4_{onset\,1}),2.0) \tag{3.36}$$

$$R_T = \frac{\rho k}{\mu \omega} \tag{3.37}$$

$$F_{onset\,3} = max\left(1 - \left(\frac{R_T}{2.5}\right)^3, 0\right) \tag{3.38}$$

$$F_{onset} = \max(F_{onset\,2} - F_{onset\,3}, 0) \tag{3.39}$$

where $Re_{\theta c}$ is the critical Reynolds number where the intermittency begins to increase in the laminar boundary layer. This increase in intermittency occurs upstream of the transition Reynolds number, $\widetilde{Re}_{\theta t}$. The F_{length} and $Re_{\theta c}$ correlations are both functions of the transition Reynolds number. A correlation for F_{length} based on $\widetilde{Re}_{\theta t}$ has been developed based on the T3 series and Schubauer and Klebanof test cases. This correlation is given below.

$$F_{length} = \begin{cases} \left[398.198 * 10^{-1} + (-119.270 * 10^{-4})\tilde{Re}_{\theta t} + (-132.567 * 10^{-6})\tilde{Re}_{\theta t}^{\,2}\right], \tilde{Re}_{\theta t} < 400 \\ \left[263.404 + (-123.939 * 10^{-2})\tilde{Re}_{\theta t} + \left(119.548 * 10^{-5}\right)\tilde{Re}_{\theta t}^{\,2} + (-101.695 * 10^{-8})\tilde{Re}_{\theta t}^{\,3}\right], 400 \le \tilde{Re}_{\theta t} < 596 \\ \left[0.5 - \left(\tilde{Re}_{\theta t} - 596.0\right) * (3.0 * 10^{-4})\right], 596 \le \tilde{Re}_{\theta t} < 1200 \\ [0.3188], 1200 \le \tilde{Re}_{\theta t} \end{cases} \tag{3.40}$$

The correlation between $Re_{\theta c}$ and $\widetilde{Re}_{\theta t}$ is defined as:

$$Re_{\theta c} = \begin{cases} \left[\tilde{Re}_{\theta t} - \left(\begin{matrix} 396.035 * 10^{-2} + (-120.656 * 10^{-4})\tilde{Re}_{\theta t} + (868.230 * 10^{-6})\tilde{Re}_{\theta t}^{\,2} \\ +(-696.506 * 10^{-9})\tilde{Re}_{\theta t}^{\,3} + (174.105 * 10^{-12})\tilde{Re}_{\theta t}^{\,4} \end{matrix}\right)\right], \tilde{Re}_{\theta t} \le 1870 \\ \left[\tilde{Re}_{\theta t} - \left(593.11 + \left(\tilde{Re}_{\theta t} - 1870.0\right) * 0.482\right)\right], \tilde{Re}_{\theta t} > 1870 \end{cases} \tag{3.41}$$

The constants for the intermittency equation are given by:

$$c_{a1} = 2.0; \quad c_{e1} = 1.0; \quad c_{a2} = 0.06; \quad c_{e2} = 50.0; \quad \sigma_f = 1.0; \tag{3.42}$$

If transition is induced by flow separation, the following modification is made:

$$\gamma_{sep} = min\left(s_1 max\left[0, \left(\frac{Re_v}{3.235 Re_{\theta c}}\right) - 1\right] F_{reattach}, 2\right) F_{\theta t} \tag{3.43}$$

$$F_{reattach} = e^{-\left(\frac{R_T}{20}\right)^4} \tag{3.44}$$

$$\gamma_{eff} = \max(\gamma, \gamma_{sep}) \tag{3.45}$$

$$s_1 = 2 \tag{3.46}$$

The transport equation that governs the momentum thickness Reynolds number for transition, $\widetilde{Re}_{\theta t}$, is given by:

$$\frac{\partial(\rho \tilde{R}e_{\theta t})}{\partial t} + \frac{\partial(\rho U_j \tilde{R}e_{\theta t})}{\partial x_j} = P_{\theta t} + \frac{\partial}{\partial x_j}\left[\sigma_{\theta t}(\mu - \mu_t)\frac{\partial \tilde{R}e_{\theta t}}{\partial x_j}\right] \tag{3.47}$$

where the source term, $P_{\theta t}$, is given by:

$$P_{\theta t} = \ c_{\theta t}\frac{\rho}{t}\left(Re_{\theta t} - \tilde{R}e_{\theta t}\right)(1.0 - F_{\theta t}) \tag{3.48}$$

$$t = \frac{500\mu}{\rho U^2} \tag{3.49}$$

where *t* is a time scale implemented for dimensional reasons. The time scale was determined based on dimensional analysis with the requirement that it scales with the convective and diffusive terms in the transport equation. The blending function, $F_{\theta t}$, turns the source term on and off in the boundary layer and allows $\tilde{R}e_{\theta t}$ to diffuse in from the freestream. This blending function holds a value of zero in the freestream and one in the boundary layer. The blending function is given below:

$$F_{\theta t} = min\left(max\left(F_{wake}e^{-\left(\frac{y}{\delta}\right)^4}, 1.0 - \left(\frac{\gamma - 1/c_{e2}}{1.0 - 1/c_{e2}}\right)^2\right), 1.0\right) \tag{3.50}$$

where

$$\delta = \frac{50\Omega y}{U} * \delta_{BL}; \quad \delta_{BL} = \frac{15}{2}\theta_{BL}; \quad \theta_{BL} = \frac{\tilde{R}e_{\theta t}\mu}{\rho U} \tag{3.51}$$

$$F_{wake} = e^{-\left(\frac{Re_\omega}{1E+5}\right)^2}; \quad Re_\omega = \frac{\rho\omega y^2}{\mu} \tag{3.52}$$

The model constants for the $\tilde{R}e_{\theta t}$equation are:

$$c_{\theta t} = 0.03; \quad \sigma_{\theta t} = 2.0; \tag{3.53}$$

The onset of transition is based on an empirical correlation with the following two parameters:

$$\lambda_\theta = \frac{\rho\theta^2}{\mu}\frac{dU}{ds} \tag{3.54}$$

$$Tu = 100\frac{\sqrt{2k/3}}{U} \tag{3.55}$$

This γ-Re_θ transition model was developed to couple with the SST turbulence model. It does so by modifying the turbulent production and destruction terms in the transport equations of the SST model. The coupled model is given below:

$$\frac{\partial}{\partial t}(\rho k) + \frac{\partial}{\partial x_j}(\rho u_j k) = \tilde{P}_k - \tilde{D}_k + \frac{\partial}{\partial x_j}\left[(\mu + \sigma_k\mu_t)\frac{\partial k}{\partial x_j}\right] \tag{3.56}$$

$$\tilde{P}_k = \gamma_{eff}P_k \tag{3.57}$$

$$\tilde{D}_k = min\left[max\left(\gamma_{eff}, 0.1\right), 1.0\right]D_k \tag{3.58}$$

where P_k and D_k are the original turbulence production and destruction terms in the SST turbulence model.

This transition model can be unstable for certain types of flows, however. To improve numerical stability, the acceleration parameters, turbulence intensity, and empirical correlations should be limited as shown below:

$$-0.1 \leq \lambda_\theta \leq 0.1; \quad Tu \geq 0.027; \quad Re_{\theta t} \geq 20; \tag{3.59}$$

One other critical parameter for accurate use of this model is grid density. For the boundary layer to be accurately captured, the grid must have a y+ value of approximately one at the first grid point off the wall. If the y+ spacing is too large, the location of the onset of transition moves upstream, so it is critical that a fine enough grid is used to capture all of the boundary layer effects.

3.2.1.2. γ-Re_θ Model Validation

Before any turbulence or transition model can be applied to a specific case, it should be validated against accepted data for basic engineering flows. This includes, but is not limited to, flow over a flat plate, flow over a cylinder in crossflow, and flows over a common airfoil. The γ-Re_θ transition model has gone through many changes since its inception, and with each change, the new model is rigorously tested before it is accepted as an accurate transition model.

The following is a list of several publications that validate the γ-Re_θ transition model for various flow cases:

- Flat plate experiments (Schubauer & Klebanoff, 1955)
- European Research Community On Flow, Turbulence, and Combustion (ERCOFTAC) benchmarks (Savill, 1993)
- Low-pressure turbine experiments (Simon, Qiu, & Yuan, 2000)
- PAK-B blade experiments (Lake, King, & Rivir, 1999), (Huang, Corke, & Thomas, 2003), (Volino, 2002)
- Unsteady wake-blade interactions (Kaszeta, Simon, & Asphis, 2001), (Stieger, 2002)

Previous work at NDSU has also detailed the limitations of the γ-Re_θ transition model by testing over a wide range of Reynolds numbers and turbulence intensities over a first stage incompressible flow vane (Kingery, Suzen, & Ames, 2010). Each of these cases listed above covers a wide range of flow characteristics including turbulence levels, Reynolds numbers, boundary conditions, and flow field geometries. The γ-Re_θ transition model behaves very well for each of these flows, so it is considered a validated model of the turbine flows that are being analyzed in this research project.

4. UND COMPRESSIBLE FLOW EXPERIMENTS

This section details the wind tunnel experiments conducted at the University of North Dakota. The data gathered by these experiments is directly used for the current simulations that are conducted at NDSU. All initial and boundary conditions of the flows come directly from these experiments.

4.1. **Wind Tunnel Characteristics and Capabilities**

The UND wind tunnel facility is unique because it can operate at steady state, whereas many transonic wind tunnels use a blow down technique. Most existing transonic wind tunnels are limited to a narrow range of Reynolds numbers, but this facility is capable of reaching exit chord Reynolds numbers as high as 1 million and as low as 50,000. This capability is desirable, as it allows for a wide range of experiments. One important study investigating the effects of large scale turbulence in turbines due to advanced combustor design was conducted at University of North Dakota's large-scale high-speed cascade wind tunnel (Ames F. , 1997). The current facility is capable of running at Reynolds numbers between 50,000 and 1,000,000 and Mach numbers ranging from 0.5 to 0.9. Free stream turbulence levels can range from 0.8% for the low turbulence (LT) cases to 9% for the Dry Low NOx (DLN) combustor cases. At the top and bottom of the cascade section are 2 bleed valves. These valves can be opened to allow a specified amount of the flow out of the cascade to provide consistent flow characteristics around each blade or vane surface (Ames F. E., 2013). The cascade test section can also be removed and replaced to test different geometries. Figure 4.1 below shows the full schematic of the closed-loop wind tunnel at UND. Figure 4.2 shows a detailed view of the turbine cascade from which all data is gathered. The inlet static and exit static taps provide boundary conditions for the

computations, and the instrumented blade or vane offer experimental results for comparison with the computations.

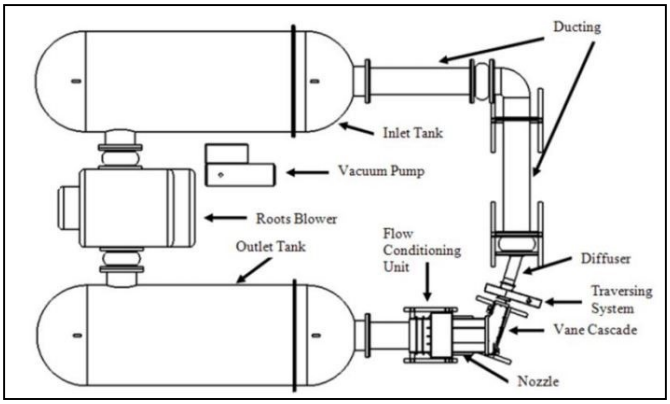

Figure 4.1. Schematic of Closed-loop High-speed Low Reynolds Number Flow Facility with Linear Vane Cascade Test Section (Ames F. E., 2013)

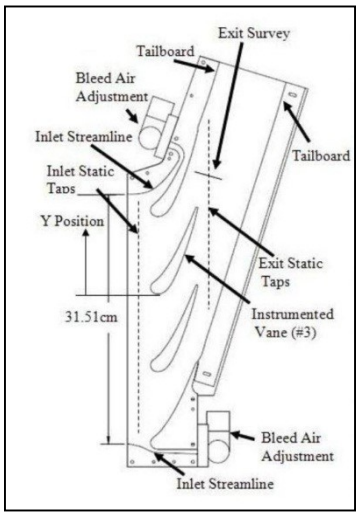

Figure 4.2. Schematic of Cascade Test Section (Ames F. E., 2013)

For this project, the wind tunnel at UND was used to provide data for 2 different geometries. The first geometry was a first stage flow vane in a NASA Global Hawk aircraft. The second geometry analyzed was an incidence angle tolerant turbine blade.

4.2. **Compressible Vane Cascade Setup**

The geometry used to test NASA Global Hawk vane is shown above in Figure 4.2. The pitch is 9.77 cm with a chord length equal to 12.1 cm. The cascade consists of four vanes (2.8

times scale) with the third from the bottom vane being instrumented. For this study, data was gathered at Reynolds numbers 90,000, 180,000, 360,000, and 720,000. Each of the experiments were run at an exit Mach number of 0.7, 0.8, and 0.9. At each condition, a high (9%) and low (0.8%) turbulence setting was also computed. These experiments detailed heat transfer and aerodynamic losses on a conventionally loaded first stage vane. A total of 48 cases were analyzed for this Global Hawk geometry.

4.3. **Incidence Angle Tolerant Turbine Blade Cascade Setup**

The second geometry involved in this project is an incidence angle tolerant turbine blade that comes from the low pressure turbine of the NASA Large Civil Tilt Rotor Vehicle, which is currently under development. This prototype aircraft is shown below in Figure 4.3.

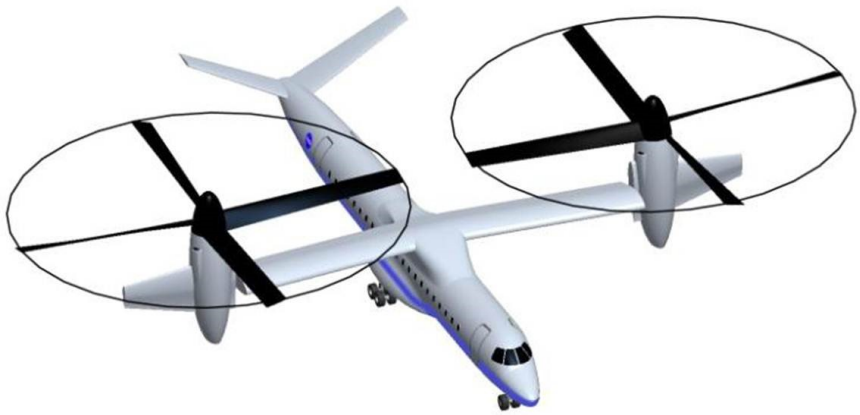

Figure 4.3. NASA Large Civil Tilt Rotor (LCTR) Vehicle (Snyder, 2012)

This aircraft has a variable speed power turbine, and as the rotational speed of the turbine changes, so does the perceived angle of attack (Snyder, 2012). As the rotational speed of the turbine increases, the normal component of the flow decreases, and therefore the angle of attack decreases. Figure 4.4 below displays a breakdown of the turbine flow's velocity components.

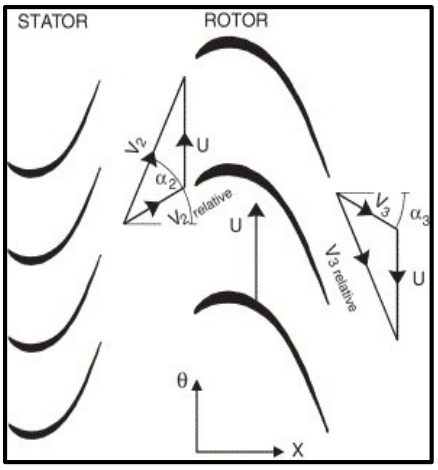

Figure 4.4. Variable Speed Turbine Flow Speed Characteristics (Hodson, 2005)

In general, the highest rotational speeds will be encountered during take-off conditions, and as the rotational speed slows for cruise flight, the angle of attack moves to the design angle for the given airfoil. The idea of the incidence angle tolerant turbine blade being analyzed in the current project is to minimize aerodynamic losses during take-off conditions while retaining optimal aerodynamic characteristics during cruise flight.

The experimental setup for the incident tolerant turbine blade is very similar to that of the vane in Figure 4.2 above. The blade geometry is substituted into the cascade section and the new shape is analyzed in the same way. In this case, two of the blades are instrumented. The 3rd blade from the bottom is again the primary instrumented blade with taps running along its surface at the midspan location. The 2nd blade from the bottom is also instrumented, but it has half of its taps located at ¼ span and the other half located at midspan. The additional data locations allow researchers to ensure that the flow is consistent through each passage as data is being collected. It also shows if there is any change in flow characteristics across the span of the blade surface. These characteristics can then be compared with computational results. Figure 4.5 shows blade 2 and blade 3, the two instrumented blades. Note that blade 2 has taps only at the midspan location, and blade 3 has taps at ¼ span and midspan.

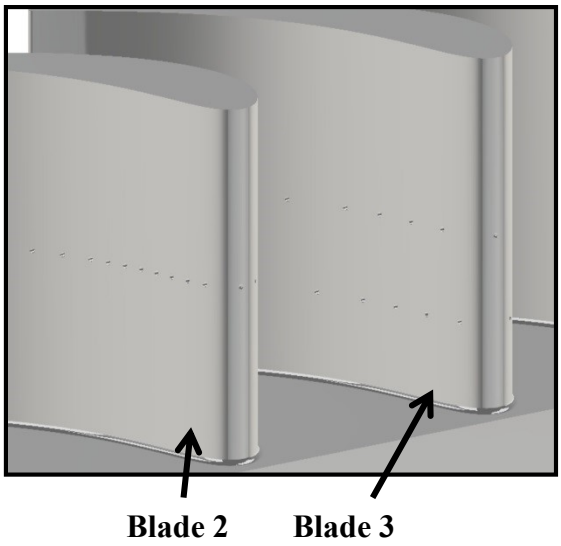

Figure 4.5. Experimental Data Tap Locations for Compressible Turbine Blade Cases

Once all the experiments are completed at UND, the raw pressure and temperature data is provided from each of the tap locations in the experiments. Turbulence characteristics are also estimated based on previous experiments conducted at UND. These data are then translated into the proper information used for computational inputs at NDSU.

5. METHODS OF CFD COMPUTATIONS AT NDSU

5.1. Hardware and Software Descriptions

The computations completed in this project were done with the aid of the high powered computing cluster at NDSU called the Center for Computationally Assisted Science and Technology (CCAST). Initially, the computations were run on a system called Cluster 3, which had 128 compute nodes with 8 processors per node. The theoretical maximum performance was 10.9 TFLOPS, and 20 ANSYS CFX licenses were available for use. As of the spring of 2014, a new system was installed called Thunder cluster. This new cluster has 53 compute nodes with 20 processors per node. The theoretical performance of the Thunder cluster is 40 TFLOPS, nearly 4 times that of Cluster 3. The ANSYS CFX license count was also increased to 128. These performance increases have greatly decreased the runtime required to complete each of the simulations in this project. Figure 5.1 below shows a photo of the CCAST computer clusters utilized for this project.

Figure 5.1. Center for Computationally Assisted Science and Technology

Several different software were used on the computational side of this project. Solidworks was used to generate the flowfield geometries. Once the geometries were available, a mesh was created using ANSYS CFX. ICEM CFD was also used to create several mesh grids, but the primary mesh software used in finding the results in the following sections was ANSYS CFX. Once the grid was established, the primary flow solver the simulations was ANSYS CFX. CFX is a very powerful computational tool that has all of the turbulence and transitional flow models that are being validated with this project.

5.1.1. Turbulence Models Implemented

One of the goals of this project was to validate current turbulence models for the given flowfields that were commercially available. In this case, the Shear Stress Transport turbulence model coupled with the γ-Re_θ transition model were the models selected for validation. As discussed in section 3.1.1.3 above, the SST model provides very accurate predictions for turbulent flows. Should any discrepancies be encountered with this SST- γ-Re_θ model combination, the second goal of this project was to implement model improvements. Model improvements are based on the k-ε turbulence model. This model will be manipulated to better represent flows at high turbulence levels and near-sonic Mach numbers.

5.1.2. Flowfield Geometry and Mesh Generation

3D flowfield models are provided by UND for each selected geometry, but the mesh is generated for each case at NDSU. In this project, two separate geometries were analyzed, and both will be shown below. A detailed mesh study was done by Jamison Huber (Huber, 2013), and the final mesh grids of that study will be discussed in the sections below.

5.1.2.1. First Stage Stator Vane

The first geometry analyzed in this project was a first stage stator vane from the NASA Global Hawk. An aerodynamic study as well as a heat transfer study will be conducted on this geometry. The computations will be run at several different Mach numbers and Reynolds numbers. The geometry will also be tested at a high turbulence (HT) setting of 9% and a low turbulence (LT) setting of 0.8%. Table 5.1 below shows each of the simulations to be conducted for the aerodynamic study, and Table 5.2 shows a tabulated breakdown of all the simulations to be completed for the heat transfer study.

Table 5.1. Aerodynamic Vane Simulations To Be Conducted

Mach Number	Turb. Level	Reynolds Numbers
0.7	LT	90K, 180K, 360K, 720K
	HT	90K, 180K, 360K, 720K
0.8	LT	90K, 180K, 360K, 720K
	HT	90K, 180K, 360K, 720K
0.9	LT	90K, 180K, 360K, 720K
	HT	90K, 180K, 360K, 720K

Table 5.2. Heat Transfer Vane Simulations To Be Conducted

Mach Number	Turb. Level	Reynolds Numbers
0.7	LT	90K, 180K, 360K, 720K, 1000K
	HT	90K, 180K, 360K, 720K, 1000K
0.8	LT	90K, 180K, 360K, 720K, 1000K
	HT	90K, 180K, 360K, 720K, 1000K
0.9	LT	90K, 180K, 360K, 720K, 1000K
	HT	90K, 180K, 360K, 720K, 1000K

A total of 54 simulations were completed for the Global Hawk flow vane; however, to acquire the desired results for the heat transfer computations, each case had to be run with an adiabatic wall condition in addition to a heat flux condition. This doubled the number of

simulations required for the heat transfer cases, so the total number of simulations required for this geometry was 84. Figure 5.2 below shows the 3D models of the vane geometry used in these simulations.

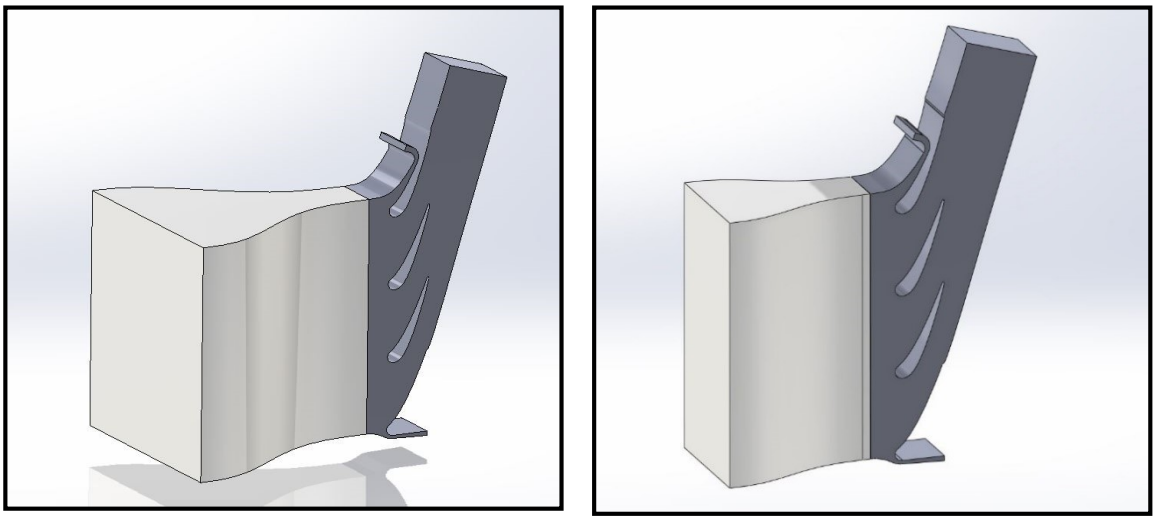

Figure 5.2. Compressible Flow Vane Geometry for Low (left) and High (right) Turbulence Settings

Depending on the turbulence condition desired, a different nozzle is attached to the cascade. The final mesh previously created by Jamison Huber for the high turbulence vane cascade is shown below in Figure 5.3 and Figure 5.4 (Huber, 2013).

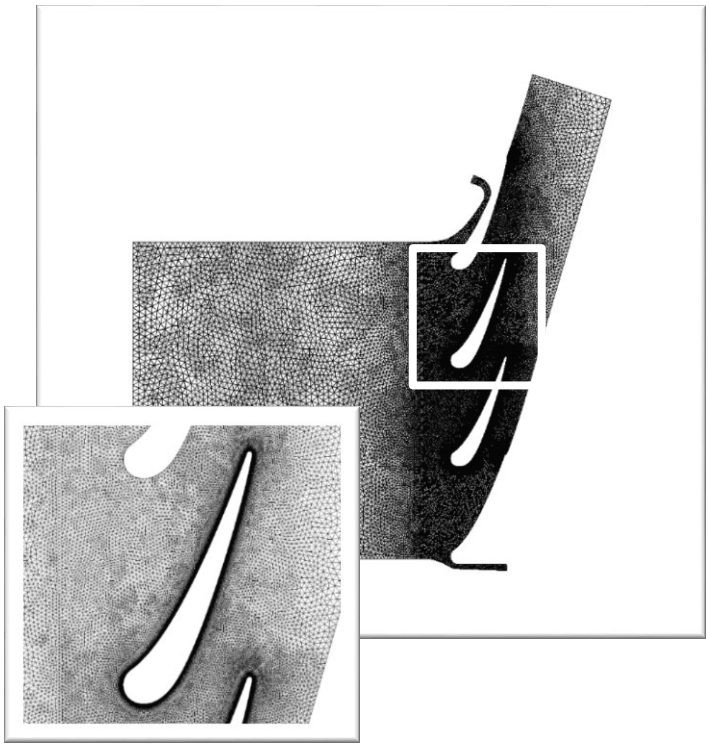

Figure 5.3. Compressible Flow Vane Mesh-Side and Zoomed View

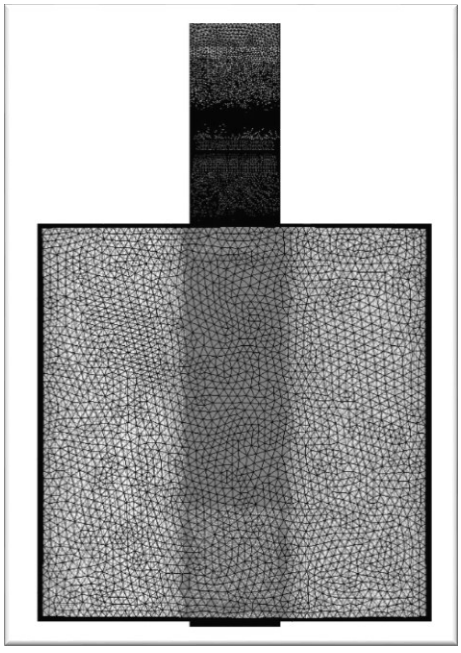

Figure 5.4. Compressible Flow Vane Mesh-Front View

The final mesh was developed based on solution convergence and the accuracy of the results. Three different grids were tested, and the shown grid was selected for the computations. The entire domain had a body spacing of 6 mm, the vane passage and wake region had a body spacing of 1.5 mm, and the vane surfaces each had a set of inflation layers extending into the passages. Because the SST model works best with a y^+ value near 1 (Menter, 1994), the first layer thickness was determined to be 1.5 $(10)^{-6}$ m thick. An inflation layer was also placed on the walls of the inlet nozzle to gather information about the viscous effects near the walls of the flowfield. The total number of nodes and elements for the vane mesh is 6.4 million and 18.7 million, respectively. A mesh with identical parameters was created for the low turbulence nozzle.

5.1.2.2. Incidence Angle Tolerant Turbine Blade

The second geometry analyzed in this project was an incidence angle tolerant turbine blade from the NASA Large Civil Tilt Rotor Vehicle. It was tested at 8 different angles of attack, from the take-off angle (-17 degrees) to the cruise angle (40 degrees). The inlet nozzle was changed in the experiment to obtain each different angle of attack. The 3D flowfield models for each angle of attack are shown below in Figure 5.5.

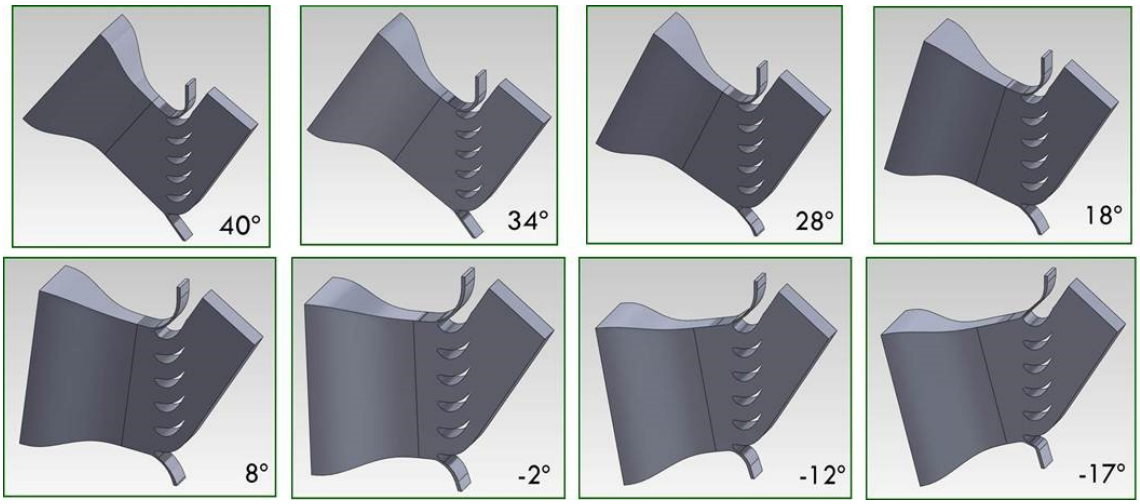

Figure 5.5. Flowfield Geometry for Each Angle of Attack

This geometry was also tested at four Reynolds numbers ranging from 50,000 to 568,000. A low turbulence (0.8%) and a high turbulence (4%) setting were also implemented at each Reynolds number and angle of attack. Table 5.3 below shows each of the simulations to be completed on the turbine blade. A total of 64 computations were completed on this geometry.

Table 5.3. Tabulated List of Simulations To Be Conducted

Incidence Angle	**Turb. Level**	**Reynolds Numbers**
40°	LT	50K, 66K, 228K, 568K
	HT	50K, 66K, 228K, 568K
34°	LT	50K, 66K, 228K, 568K
	HT	50K, 66K, 228K, 568K
28°	LT	50K, 66K, 228K, 568K
	HT	50K, 66K, 228K, 568K
18°	LT	50K, 66K, 228K, 568K
	HT	50K, 66K, 228K, 568K
8°	LT	50K, 66K, 228K, 568K
	HT	50K, 66K, 228K, 568K
-2°	LT	50K, 66K, 228K, 568K
	HT	50K, 66K, 228K, 568K
-12°	LT	50K, 66K, 228K, 568K
	HT	50K, 66K, 228K, 568K
-17°	LT	50K, 66K, 228K, 568K
	HT	50K, 66K, 228K, 568K

The mesh generation for this turbine geometry was identical to that of the Global Hawk vane. A mesh study was conducted in a previous project (Huber, 2013), and the final mesh will be discussed here. A body sizing of 5.7 mm was implemented on the entire domain. Near the blade passages, a body was placed that contained a much finer spacing of 0.76 mm. This fine spacing allows the solver to more accurately capture the flow characteristic in the wake region. Because the SST model works best with a y^+ value of 1, an inflation layer was placed on each blade surface with the first layer thickness being $1(10)^{-6}$ m. The total number of nodes was approximately 11.5 million for each case. Figure 5.6 below shows the final mesh used in the turbine blade cases. As the angle of attack changes, all mesh parameters remain constant, but the geometry changes.

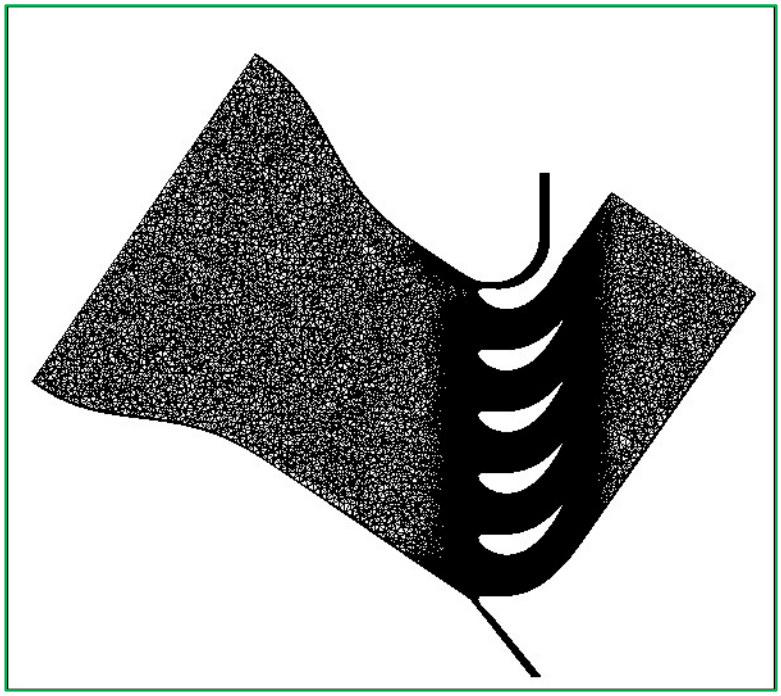

Figure 5.6. Final Mesh for Turbine Blade Cases

With the geometry and mesh developed, the next step of the project is to implement the experimental data into the CFD software as boundary or initial conditions.

5.1.3. Transitioning from Experimental Data to Computational Inputs

The following is a list of variables given by the experiments conducted at UND:

- Total Temperature
- Total Pressure
- Reynolds Number
- Mach Number
- Static Pressure
- Static Temperature
- Velocity

These variables are provided at locations ¼ chord upstream, ¼ chord downstream, and around the instrumented blade or vane surface. The following list gives each of the variables required for input into the CFX simulations conducted at NDSU:

- Reference pressure
- Relative pressure at inlet
- Turbulence kinetic energy (k)
- Turbulence eddy dissipation (ε)
- Total temperature at inlet
- Relative pressure at the outlet

The reference pressure (domain pressure) in CFX is set equal to the static pressure in the outlet of the experiments. Relative pressure at the inlet is calculated by subtracting the domain pressure (above) from the total inlet pressure in the experiments. The experimental pressures are given along the entire height of the cascade, so the values are averaged. Turbulence kinetic energy is calculated by the following equation:

$$k = 1.5(UI)^2 \tag{5.1}$$

where U is the average velocity at the inlet and I is free stream turbulence intensity, both of which are calculated experimentally.

Turbulent eddy dissipation is calculated with the following equation:

$$1.5 * \frac{u'^3}{\varepsilon} = \text{Lu} \tag{5.2}$$

where *u*' is the fluctuating component of the streamwise velocity and Lu is the energy scale (cm), both of which are obtained experimentally.

Total temperature at the inlet is given experimentally. Relative pressure at the outlet is set to 0 Pa for each case. At this point, there is enough information to begin the computations. Since the data locations are slightly different between the experiments and computations (i.e. ¼ upstream vs. nozzle inlet), the data may slightly deviate from the experimental values. If this is the case, the computations are iterated until the experimental data is perfectly matched. This process will be discussed in more detail in the results sections below.

6. RESULTS AND DISCUSSION OF COMPRESSIBLE FLOW SIMULATIONS

6.1. Part I—First Stage Stator Vane

As the vane data is presented, note the variables on each axis and how they are represented. The y-axis presents the variable of interest, and the x-axis represents the surface arc around the vane. The center of each plot on the x-axis represents the stagnation region where S = 0. As the S value become negative, the data presented corresponds to the top surface of the vane, or the suction surface. As the S value grows positive, the data shown represents the suction surface. Figure 6.1 below shows a schematic of how the data is displayed regarding the x-axis.

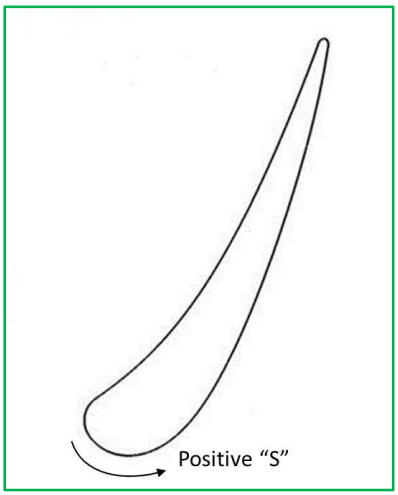

Figure 6.1. Vane Surface Arc X-axis Notation

An aerodynamic study along with a heat transfer study was conducted on the flow vane. Each set of results will be presented separately in the following sections.

6.1.1. Aerodynamic Simulation Results

During the aerodynamic simulations of the NASA Global Hawk vane, pressure data along the instrumented vane surface was compared between the UND experiments and the

computations conducted at NDSU. Figure 6.2 through Figure 6.5 display the results of these simulations for each Reynolds number and turbulence level tested.

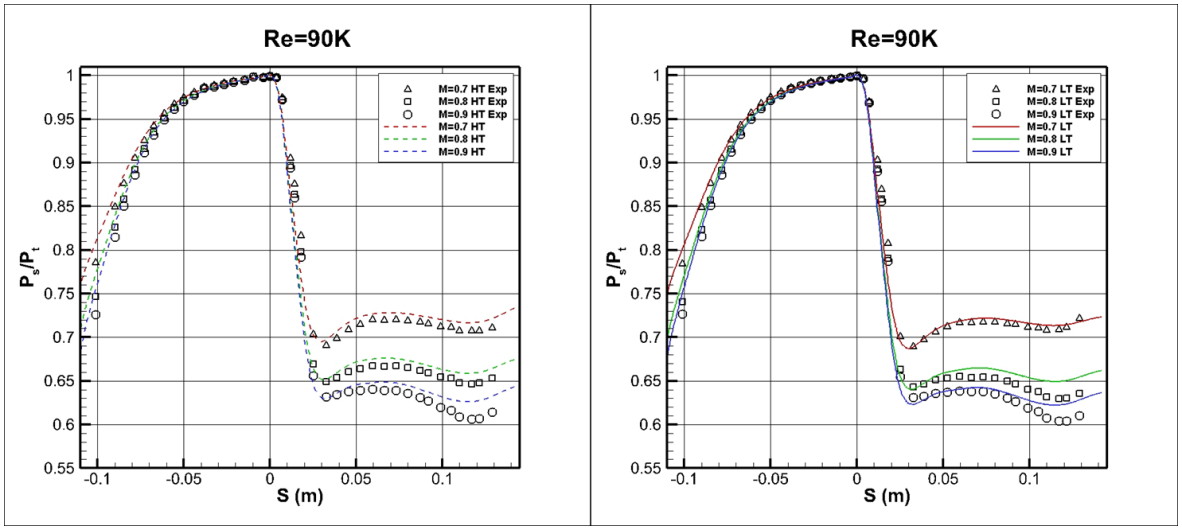

Figure 6.2. Ps/Pt Plots for Re = 90,000 at High Turbulence (left) and Low Turbulence (right) Setting.

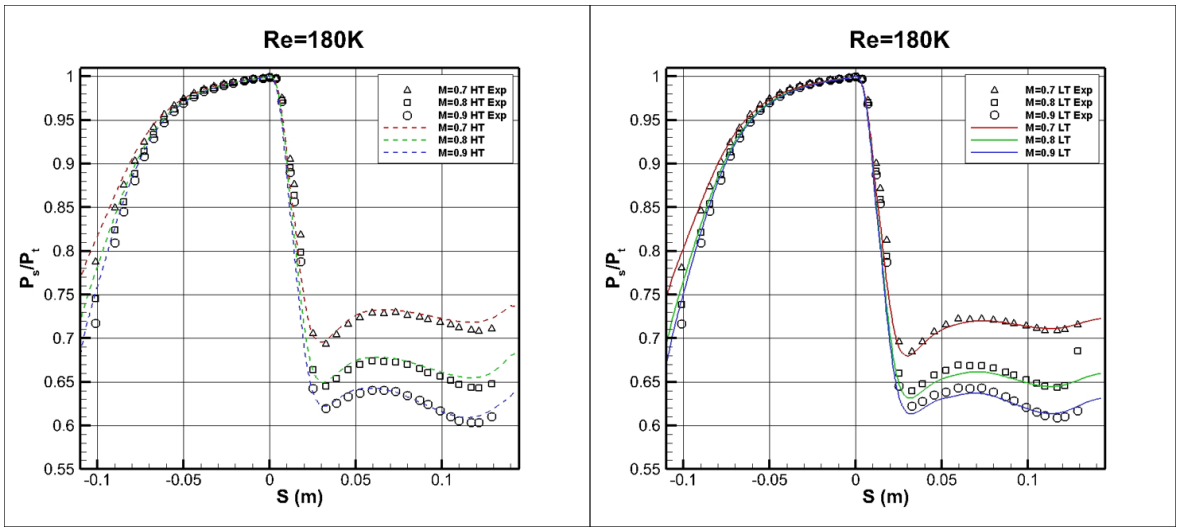

Figure 6.3. Ps/Pt Plots for Re = 180,000 at High Turbulence (left) and Low Turbulence (right) Setting.

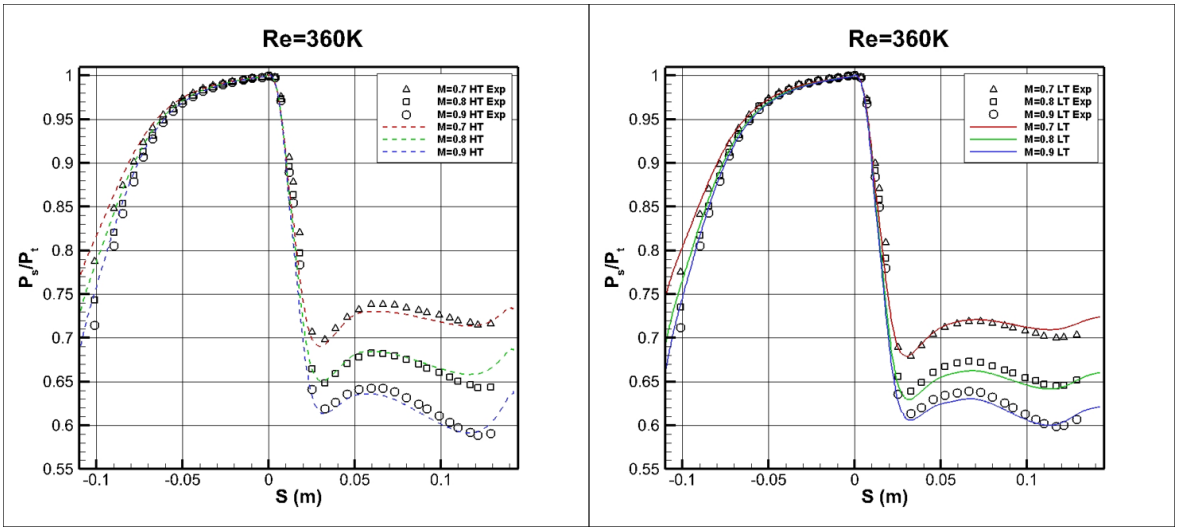

Figure 6.4. Ps/Pt Plots for Re = 360,000 at High Turbulence (left) and Low Turbulence (right) Setting.

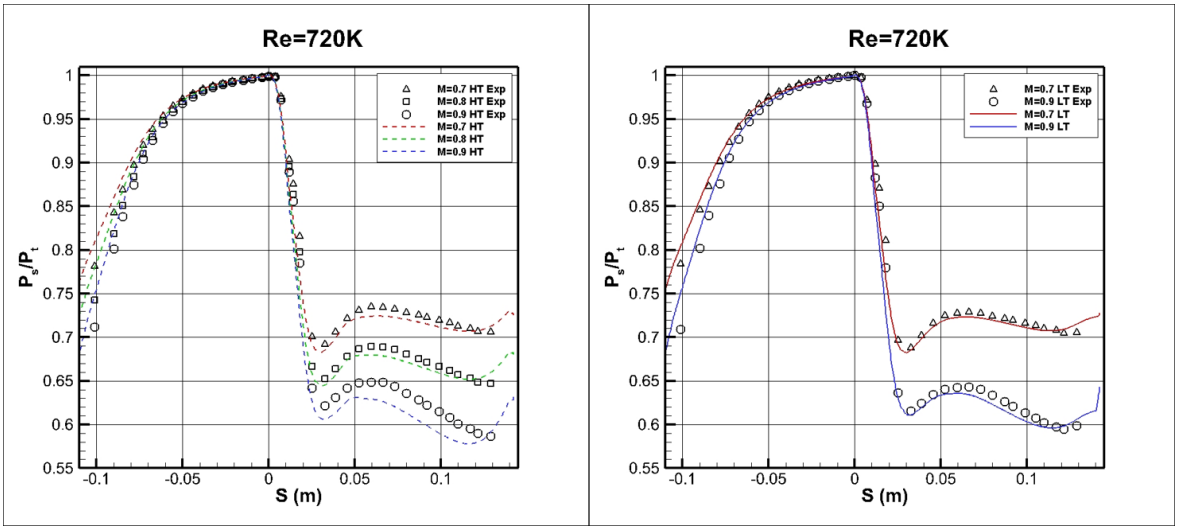

Figure 6.5. Ps/Pt Plots for Re = 720,000 at High Turbulence (left) and Low Turbulence (right) Setting.

In general, the SST turbulence model and the γ-Re_θ transition modeled provided nearly perfect predictions on the pressure surface of the vane. On the suction surface, the data was slightly over predicted at lower Reynolds numbers and under predicted at the higher Reynolds numbers. When investigating these discrepancies, it was found that the exit Mach number was slightly off from the experimental values. To remedy this problem, the pressure at the outlet of

the domain was increased or decreased to speed up or slow down the flow to match the experimental values, depending on the initial prediction. Once the exit Mach number was matched with the experimental values, the Ps/Pt plots show a near perfect prediction across the entire vane surface. An example of this improvement at a Reynolds number of 360,000 is shown in Figure 6.6 and Figure 6.7 below.

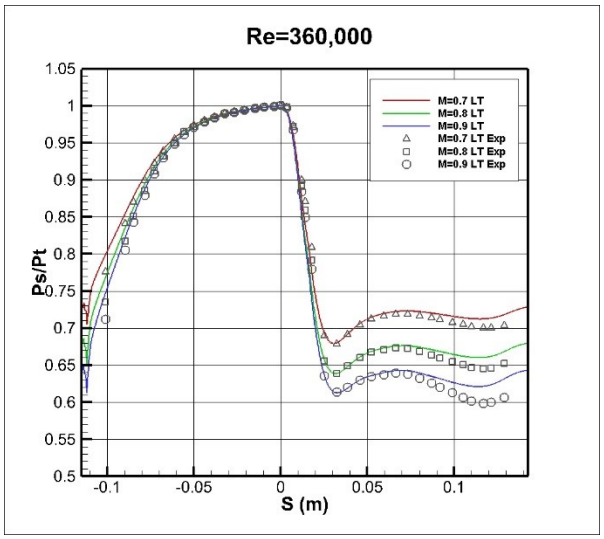

Figure 6.6. Corrected Pressure Distribution for Re = 360,000 at Low Turbulence

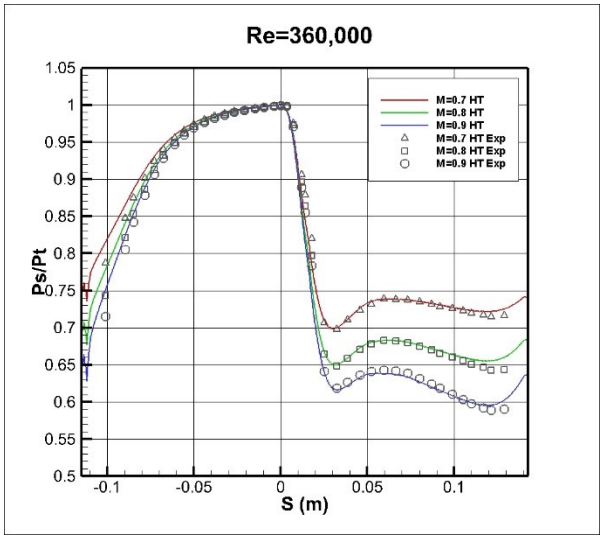

Figure 6.7. Corrected Pressure Distribution for Re = 360,000 at High Turbulence

Before any heat transfer or wall shear investigations take place, it is important to verify that the experimental parameters are matched correctly. At this point, it is safe to begin comparing wall heat transfer data with the experimental results at UND.

6.1.2. Heat Transfer Simulation Results

After an aerodynamic study was conducted on the vane geometry, a separate heat transfer study was completed at the same flow conditions. In this study, the variable of interest was the heat transfer coefficient, which was calculated by the following equation:

$$h = \frac{q''}{(Blade\ Surface\ Area) * (T_{flux} - T_{adiabatic})} \tag{6.1}$$

where *q''* is a heat flux on the vane surface, which is found experimentally. T_{flux} is the temperature of the vane surface during the simulation run with a heat flux condition, and $T_{adiabatic}$ is the temperature of the vane surface during the adiabatic condition. Because both an adiabatic and a heat flux condition are required to obtain results, the heat transfer study required twice the amount of computations to acquire the results.

Previous studies at NDSU (Kingery, Suzen, & Ames, 2010) have shown that heat transfer is over predicted by the SST model on the suction surface of the vane during higher turbulence settings and higher Reynolds numbers for incompressible flows. These studies also predicted an early onset of transition using the SST-γ-Re_θ model combination. The geometry in the present study is very similar, however the compressibility effects of the flow are now being analyzed. Results for all heat transfer cases are shown below in Figure 6.8-Figure 6.12.

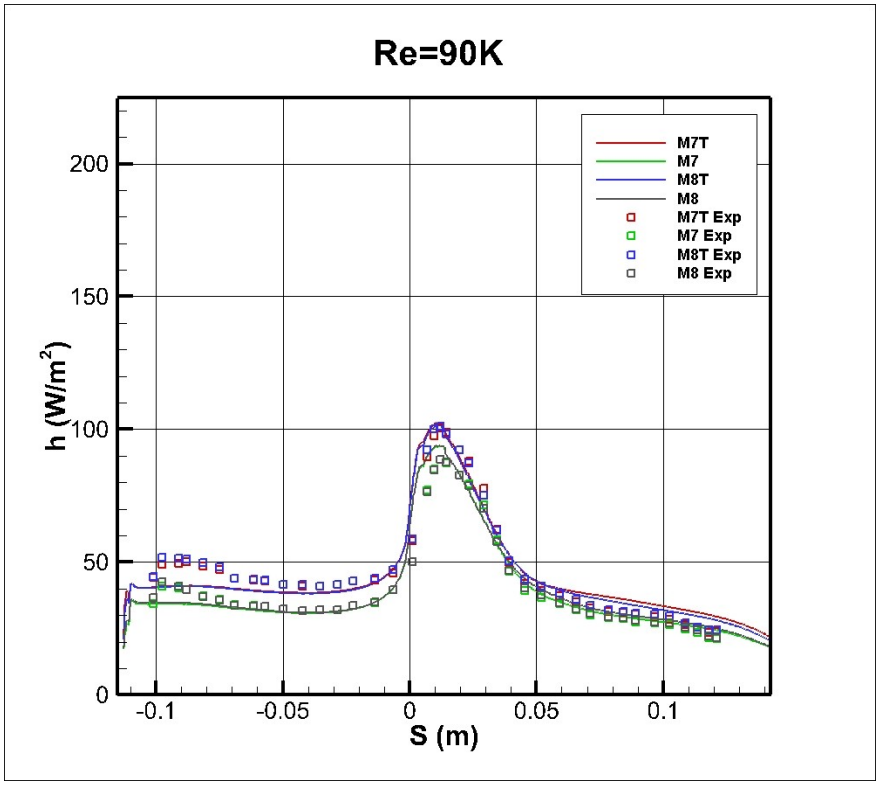

Figure 6.8. Heat Transfer Coefficient for Re = 90,000

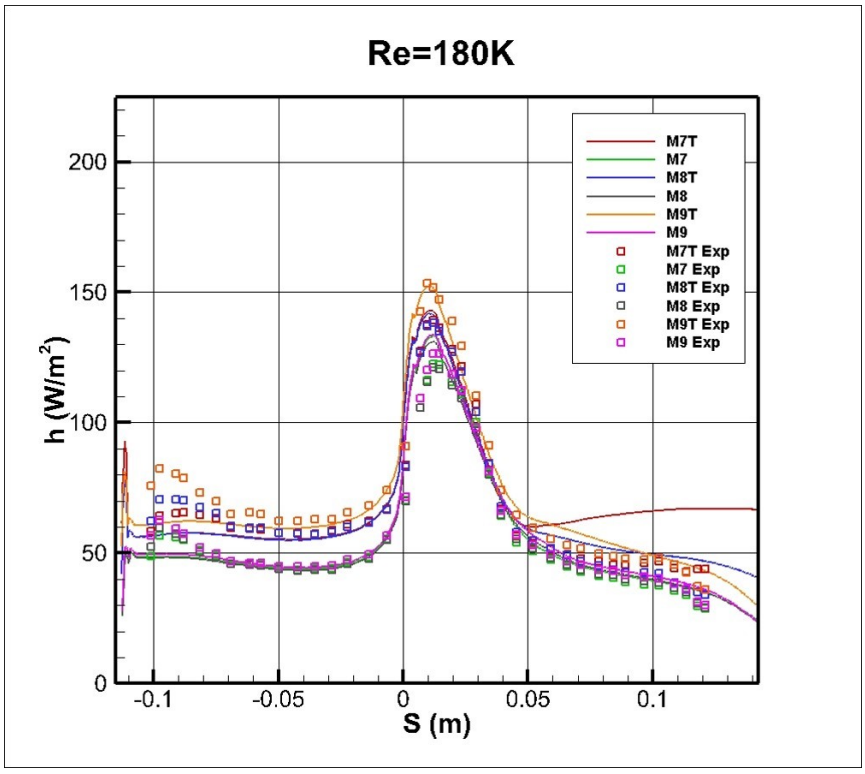

Figure 6.9. Heat Transfer Coefficient for Re = 180,000

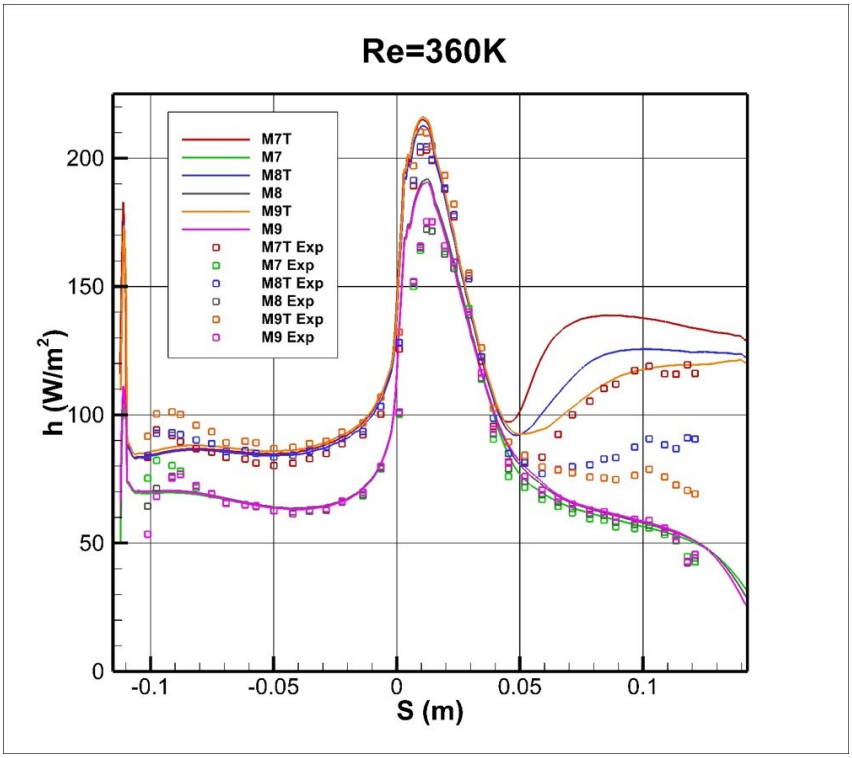

Figure 6.10. Heat Transfer Coefficient for Re = 360,000

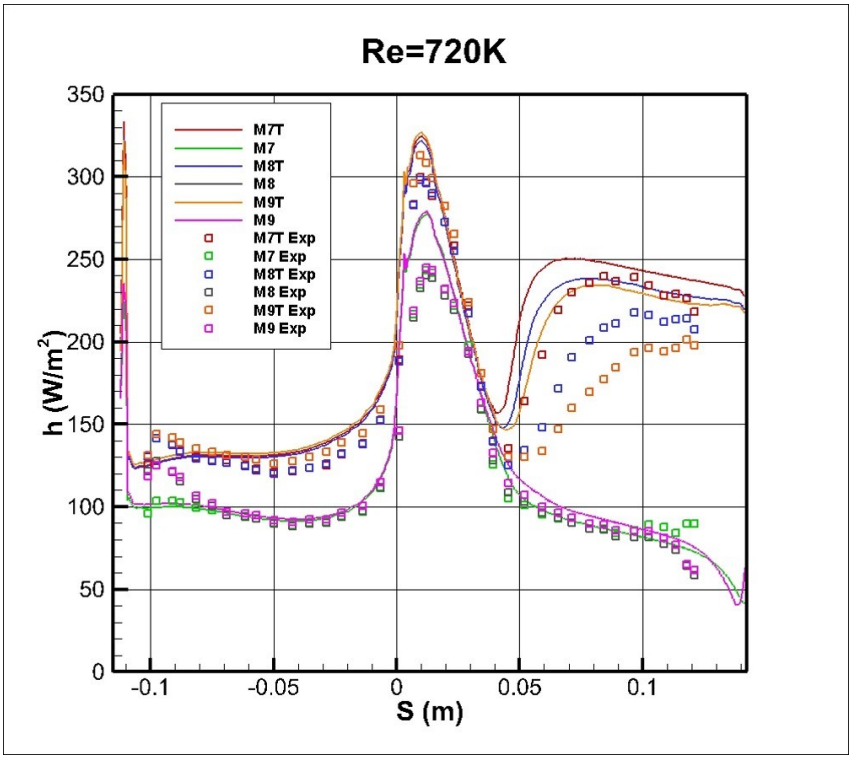

Figure 6.11. Heat Transfer Coefficient for Re = 720,000

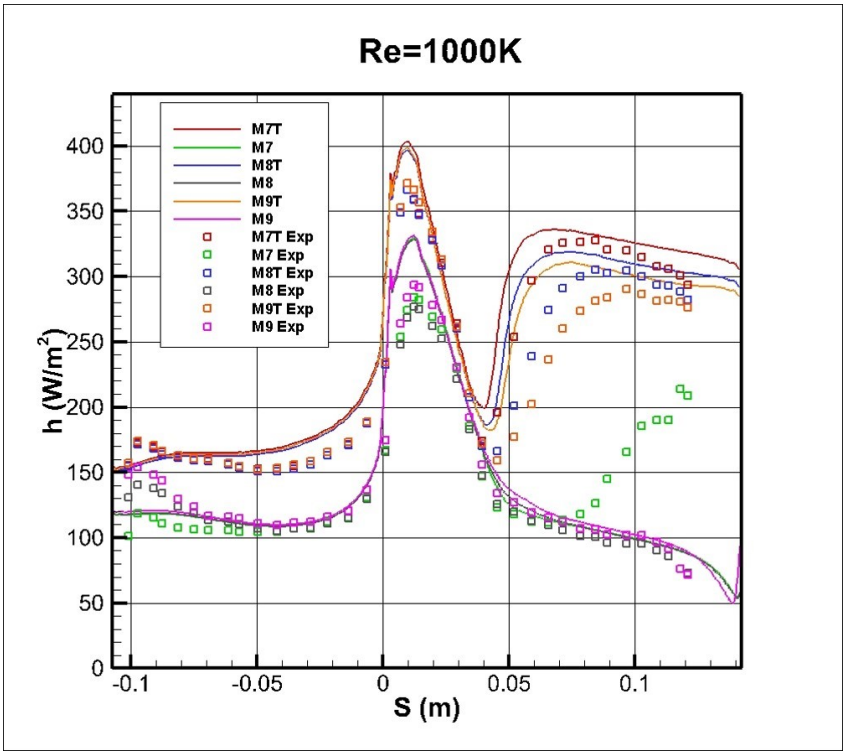

Figure 6.12. Heat Transfer Coefficient for Re = 1,000,000

As expected, the heat transfer becomes over predicted on the suction surface for all Reynolds numbers above 360,000 at the high turbulence setting. Transition onset is also predicted too early, and the severity of the discrepancy decreases as the Mach number decreases.

In all low turbulence cases, the heat transfer predictions are nearly perfect on both the pressure and suction surfaces, but the computations slightly over predict heat transfer in the stagnation region.

6.1.2.1. Heat Transfer Results with Modified Turbulence Model

To improve the heat transfer predictions at the high turbulence settings, a modification to the k-ε section of the SST turbulence model was to be implemented as discussed in section 3.1.1.4 above. Before modifying the SST model, the k-ε model alone was modified with a mixing length model (Ames & Kwon, 1996). The goal of this implementation was to test the model manipulation tools offered in the CFX software. Ideally, the new model should match the

heat transfer coefficient in the turbulent region of the vane surface. Once the turbulent section is matched, a transition model will be coupled with the new turbulence model to improve the predictions across the entire surface. Figure 6.13-Figure 6.15 show the heat transfer results with two versions of the new turbulence model implemented.

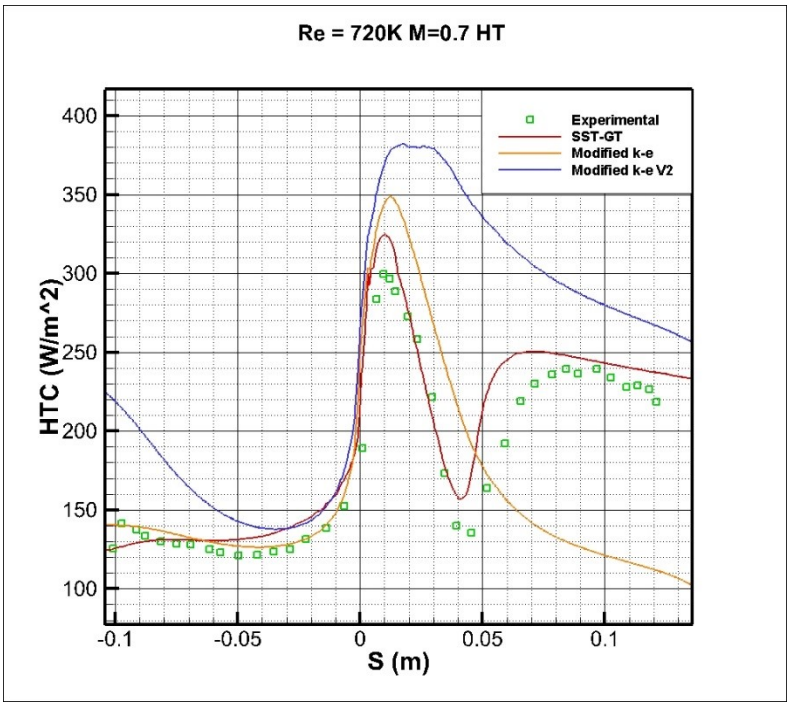

Figure 6.13. Heat Transfer Coefficient for Re=720k and M=0.7 with New Turbulence Model

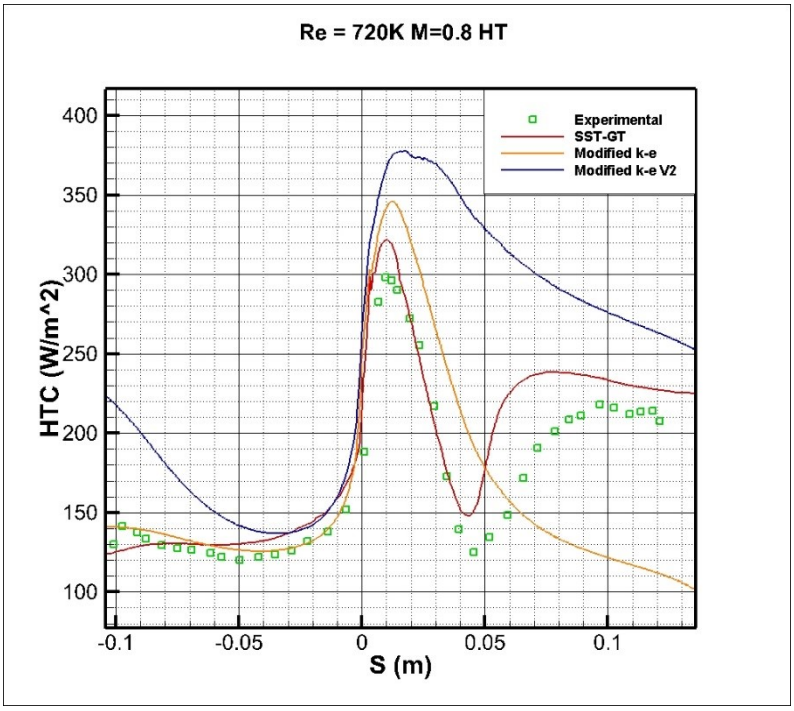

Figure 6.14. Heat Transfer Coefficient for Re=720k and M=0.8 with New Turbulence Model

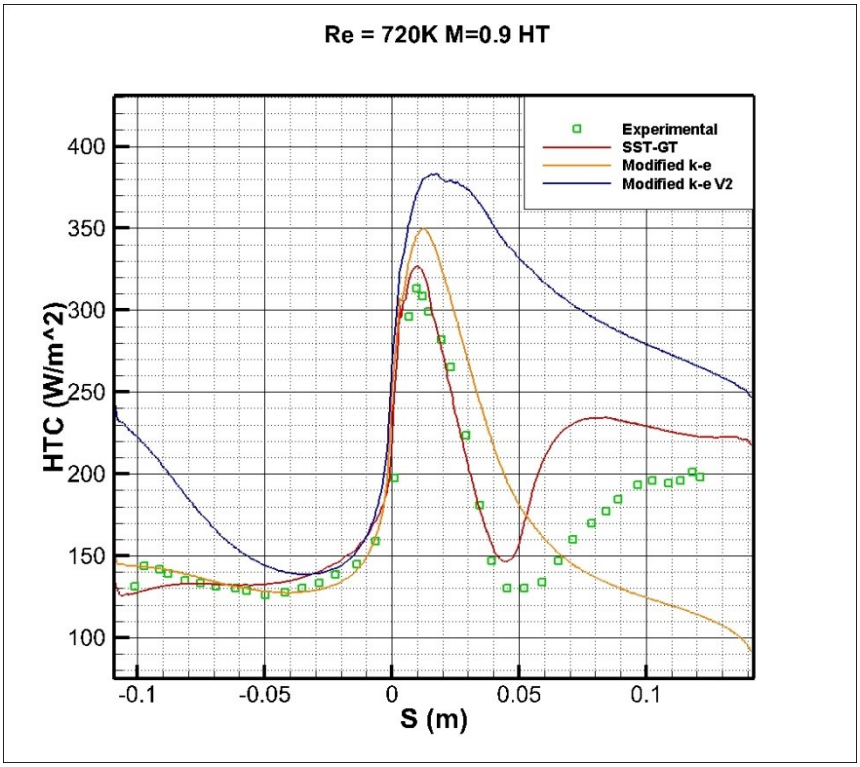

Figure 6.15. Heat Transfer Coefficient for Re=720k and M=0.9 with New Turbulence Model

With the first version of the modified k-ε turbulence model implemented, the results improve on the pressure surface of the vane, but heat transfer is over predicted in the stagnation region and under predicted on the suction surface. The second implementation of this model over predicts heat transfer across the entire surface. The differences between these implementations will be discussed below.

6.1.2.2. Flat Plate Turbulence Model Investigation

At this point, it was evident that the new model needed to be validated against an accepted turbulence model to ensure that it was implemented correctly. In this case, the various models available in CFX were tested against a set of NASA data across a 2 meter long flat plate (Rumsey, 2012). The grid used for these simulations had a y+ value of about 0.25, and it was provided by NASA. Some of the important parameters to investigate in a turbulence model are the eddy viscosity, skin friction, and boundary layer velocity profiles. Plotting these values against accepted values give researchers hints as to whether or not the models are behaving as they should. Several models were tested in this flat plate study, including Shear Stress Transport, k-epsilon, and Eddy Viscosity Transport model, which is a one equation model based on k-epsilon. Figure 6.16 below shows the skin friction plotted along the length of the flat plate. The data lines labeled CFL3D and FUN3D are data from NASA that use an in-house code for structured and unstructured grids.

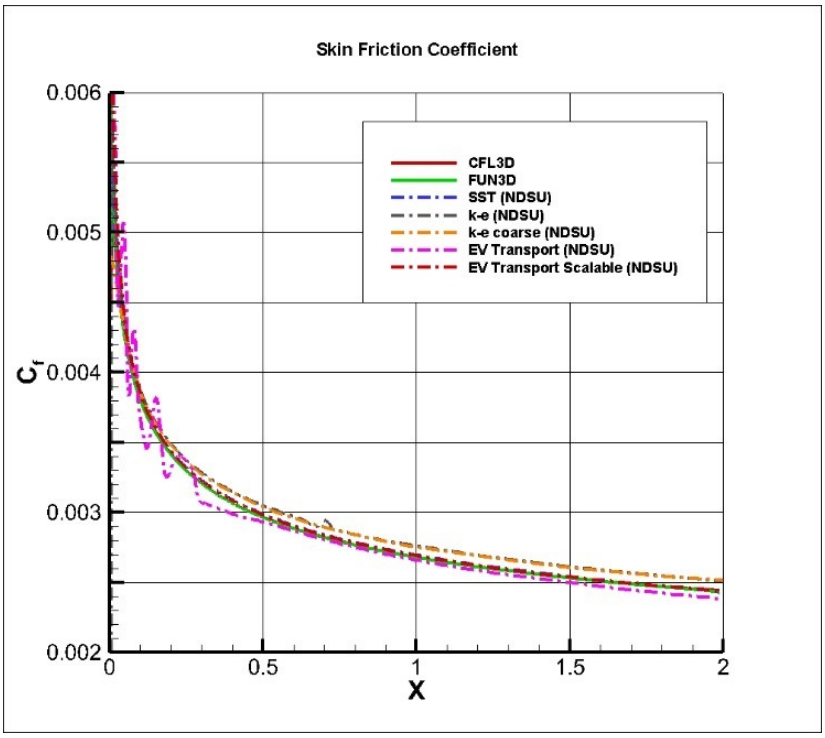

Figure 6.16. Skin Friction along a Flat Plate

The k-epsilon models tend to slightly over predict along the entire length of the flat plate, while the SST and eddy viscosity transport models predict very closely to the accepted data.

Eddy viscosity contours can also be a useful tool to determine whether a turbulence model is implemented correctly. Figure 6.17 below shows a non-dimensionalized eddy viscosity contour provided by NASA's CFL3D solver code running the SST turbulence model. Figure 6.18 and Figure 6.19 represent the eddy viscosity contours obtained with the ANSYS CFX solver using the SST and k-ε turbulence models. Figure 6.20 and Figure 6.22 then show contours for eddy viscosity using the modified k-ε models.

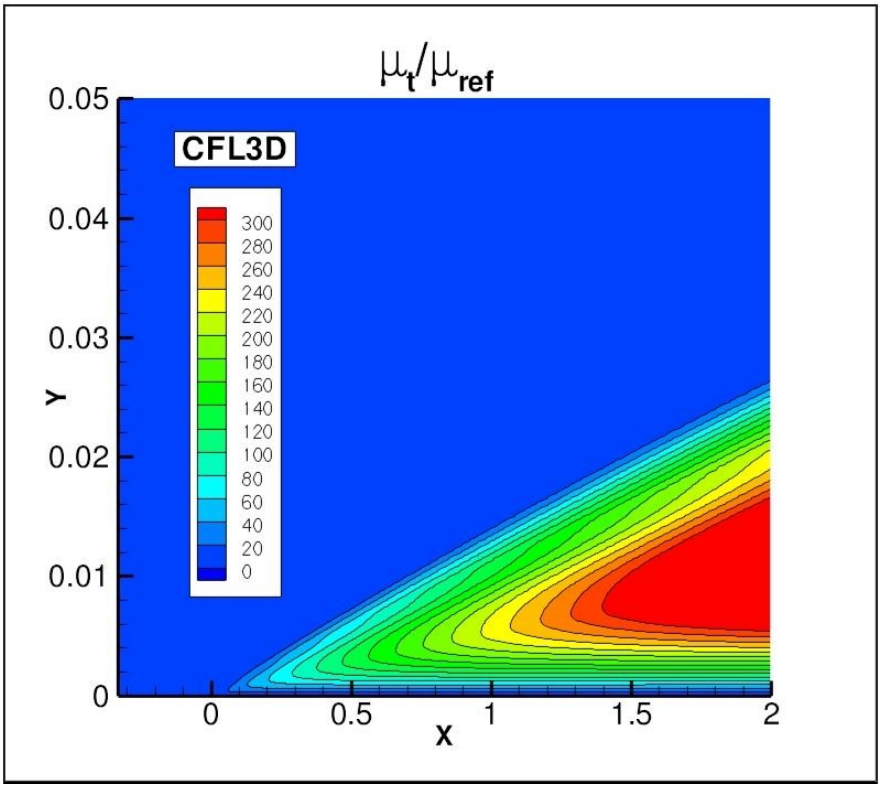

Figure 6.17. Nondimensionalized Eddy Viscosity Contour for NASA CFL3D Code

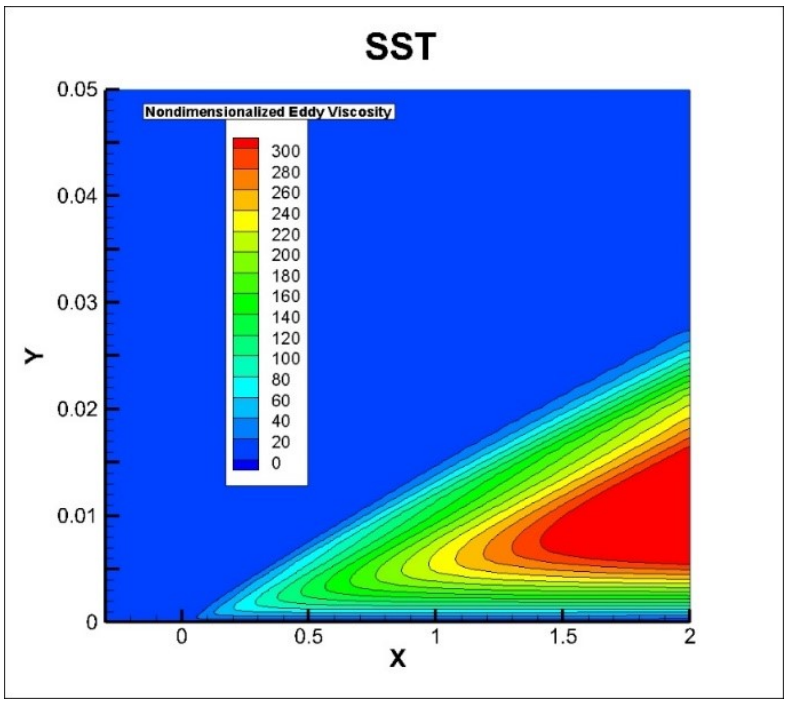

Figure 6.18. Eddy Viscosity Contour for SST Turbulence Model at NDSU

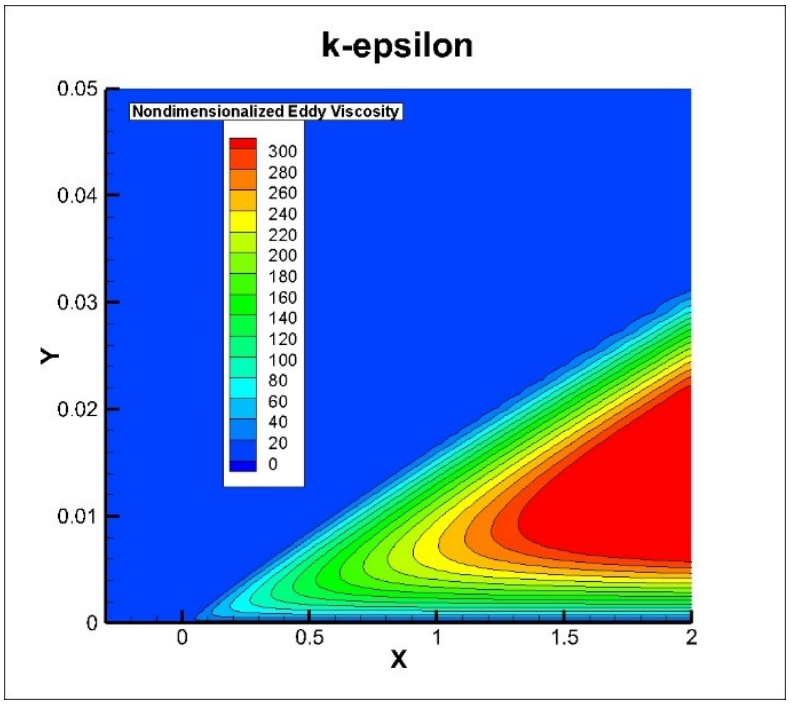

Figure 6.19. Eddy Viscosity Contour for k-ε Turbulence Model at NDSU

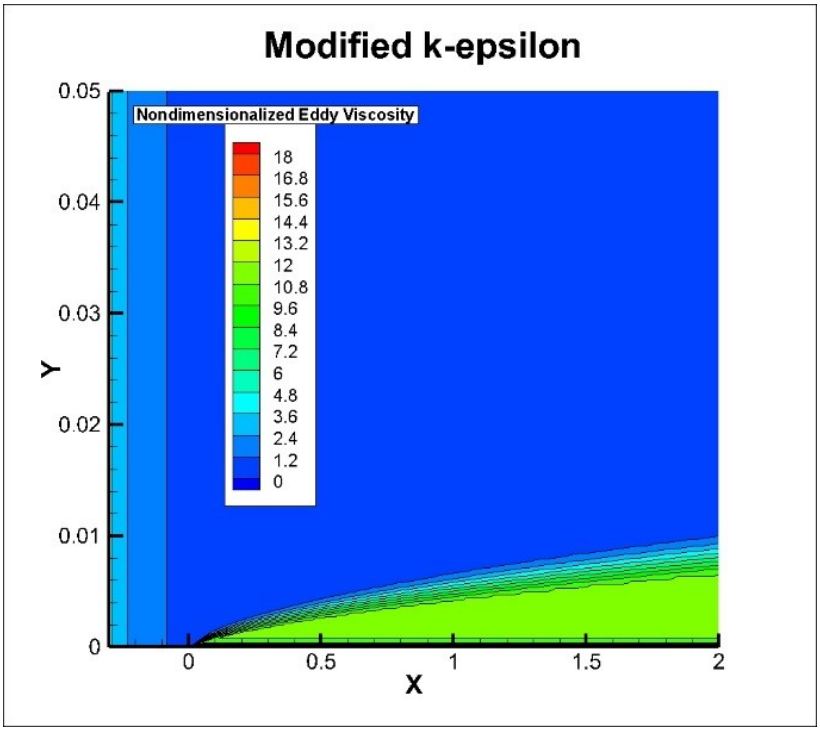

Figure 6.20. Eddy Viscosity Contour for Modified k-ε Turbulence Model at NDSU

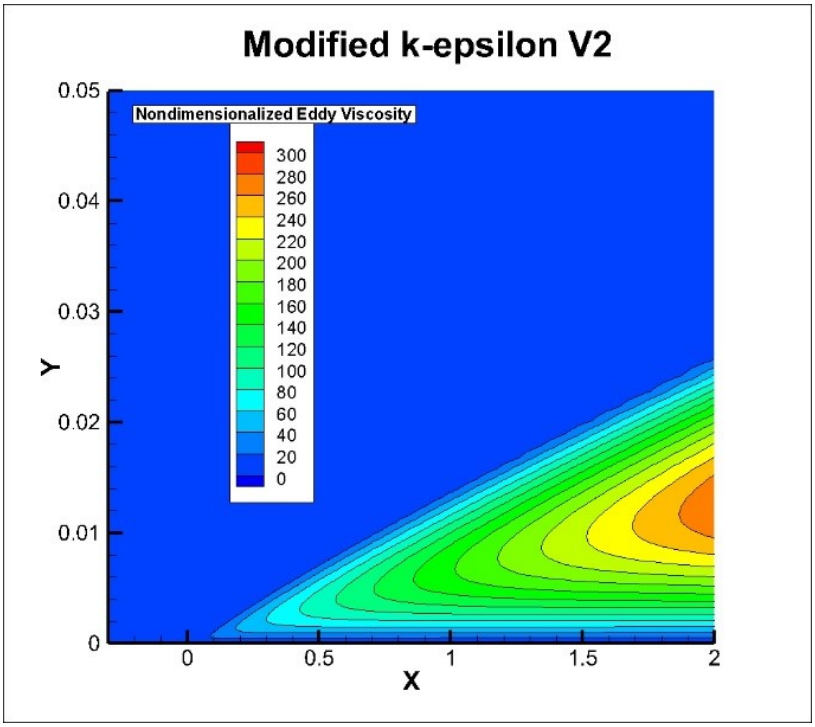

Figure 6.21. Eddy Viscosity Contour for Modified k-ε Version 2 Turbulence Model at NDSU

The SST model at NDSU provides a very similar result to the NASA model, however the ANSYS CFX model does not capture the sharp wave at the edge of the boundary layer. The k-ε contour shows a boundary layer that grows more rapidly than the SST model. The first version of the modified k-ε contour shows that there is a major error with the implementation of the new model. Over the course of the 2 meter flat plate, the eddy viscosity too low by more than a factor of 10. At this point, it was clear that the implementation of this model required further investigation. A second model was implemented with all the same equations; however, the turbulence kinetic energy and dissipation rates in the damping function were calculated at each point in the flowfield instead of being held at freestream values. While there are still discrepancies, this improved the model significantly, as shown in Figure 6.21. While contours are useful for portraying an overall picture of the flow, it can be difficult to quantify any discrepancies with the models. Instead, Figure 6.22 below shows each model's eddy viscosity at a location approximately halfway across the plate. This plot shows the problematic areas much more clearly.

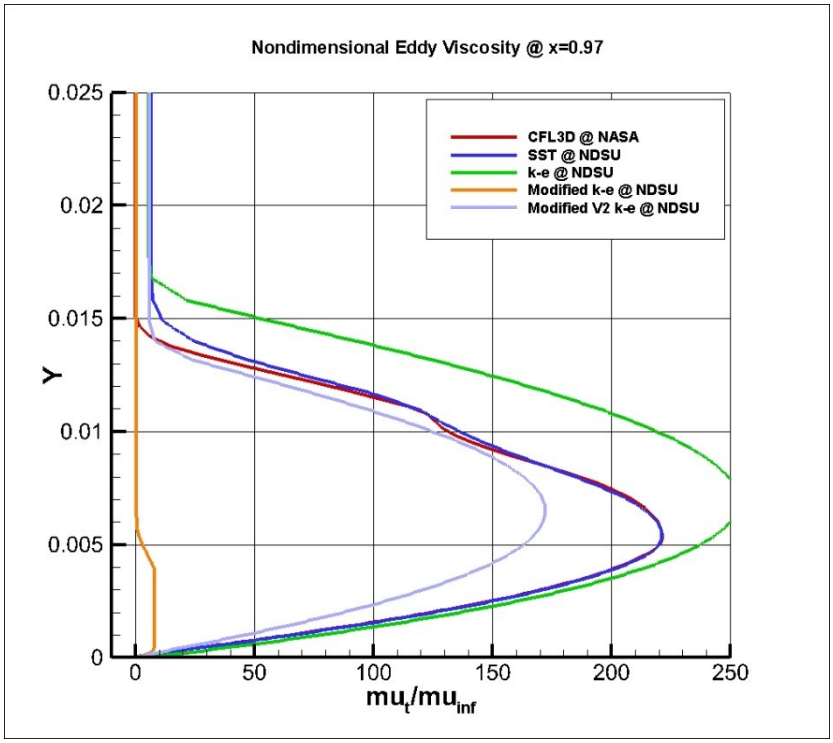

Figure 6.22. Eddy Viscosity for Each Model at X = 0.97 m

The SST model at NDSU behaves very similarly to the NASA code; however, there is a small discrepancy at the outer edge of the boundary layer at a reference viscosity of about 125. The CFX solver used at NDSU fails to model the sharp increase in eddy viscosity at that point. One other key point that should be noted is the fact that the CFX eddy viscosity never actually returns to zero beyond the boundary layer. This result is unexpected, although the discrepancy is very small. The k-ε model predicts a much taller boundary layer than the SST model. The shape near the wall is accurate until the center of the boundary layer is reached, at which point the eddy viscosity levels increase over 10% more than that of the SST code. The orange line shows the modified k-ε model tested in the CFX solver. This plot again exemplifies that this model is incorrectly implemented and is not functioning properly. The light blue line shows that version 2 of the new model is behaving much more accurately. Model manipulation in the CFX solver is limited, so an in-house code may need to be produced for testing to improve the results.

Perhaps the most telling plot to determine a turbulence model's behavior in the boundary layer is the u+ vs. y+ plot. u+ represents a non-dimensionalized velocity while y+ represents a non-dimensionalized distance from the wall. Near the wall up to a y+ value of about 10, the u+ and y+ values should have a linear relationship. This region is called the viscous sublayer. When y+ is near 10, an inflection point should occur into a logarithmic region. This is often referred to as the log law region. As the distance grows to the edge of the boundary layer, the wake region is reached (White, 2006). If the profiles for each of these three regions is not matched, something may be incorrectly implemented with the turbulence model. Figure 6.23 below shows u+ vs y+ profiles for several turbulence models at a location approximately halfway across the plate.

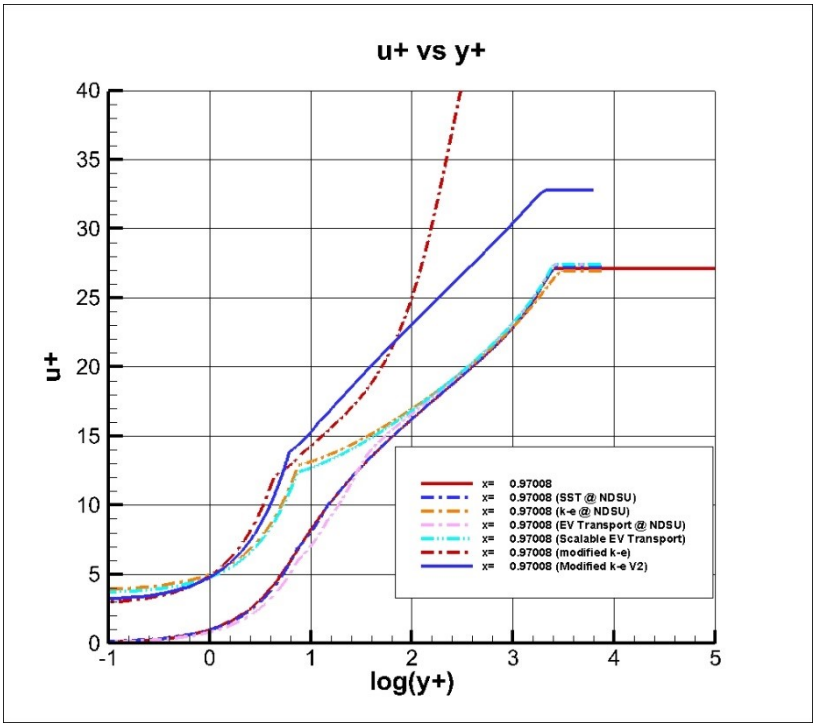

Figure 6.23. u+ vs y+ for Each Model at X = 0.97008

From this plots, the SST model at NDSU is very comparible to the CFL3D solver from NASA. However, it is evident that the k-ε and eddy viscosity transport models are exibiting very interesting behavior in the near-wall viscous sublayer. The initial modified k-ε implentation

shows a very poor result and grossly overpredicts the u+ value beyond the log law region of the boundary layer. Version 2 of the implementation shows the three very distince boundary layer regions, but they are offset by a u+ value of approximately five. After extensive testing and investigation, it was found that the CFX k-ε solver does not behave properly with a low y+ value. One of the main criteria for this flat plate test is that an identical mesh be used for comparison. Because of the low y+ value on this mesh, the wall function of the k-ε and Eddy Viscosity Transport models are displaying an incorrect result. Unfortunately, the deficiencies discovered with the k-ε model in ANSYS make the model less reliable for manipulation. The quantities investigated in this project, especially heat transfer, require a very fine mesh density near the wall, so the k-ε model should not be used with this solver. The mixing length and algebraic models should be implemented into the k-ε portion of the SST turbulence model, and the flat plate analysis should be repeated.

6.2. **Part II—Incidence Angle Tolerant Turbine Blade**

In addition to the first stage vane discussed previously, an incidence angle tolerant turbine blade design was analyzed. The idea behind this geometry is to develop a turbine blade that minimizes aerodynamic losses over a wide range of attack angles. The data will be presented in the same way as the vane, with the variable of interest on the Y axis and the surface arc on the X axis. In this case, the variable of interest is the pressure coefficient, C_p, and it is calculated with the following equation:

$$C_p = \frac{P_{blade} - P_\infty}{P_\infty - P_{exit}} \tag{6.2}$$

Figure 6.24 below shows the x-axis notation of the C_p data charts. The S value is zero at the front pressure tap, or the stagnation region. As S becomes positive, the data comes from the

suction surface of the blade. As S becomes negative, the data comes from the pressure surface of the blade.

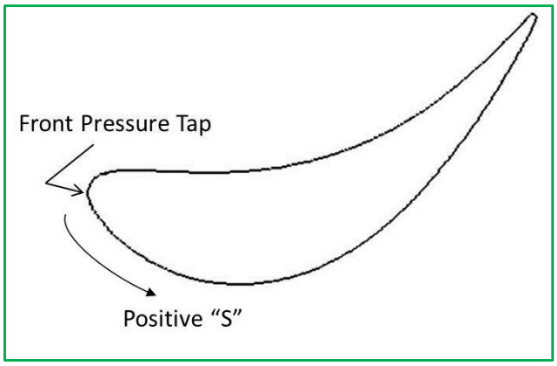

Figure 6.24. Turbine Blade X-Axis Notation

6.2.1. Aerodynamic Simulation Results

Figure 6.25 to Figure 6.40 below show the C_p distribution for each of the turbine cases. Note that the 40, 34, and -2 degree low turbulence plots have an additional experimental data set for blade 3. The extra set is used to verify that the flow is uniform through each blade passage.

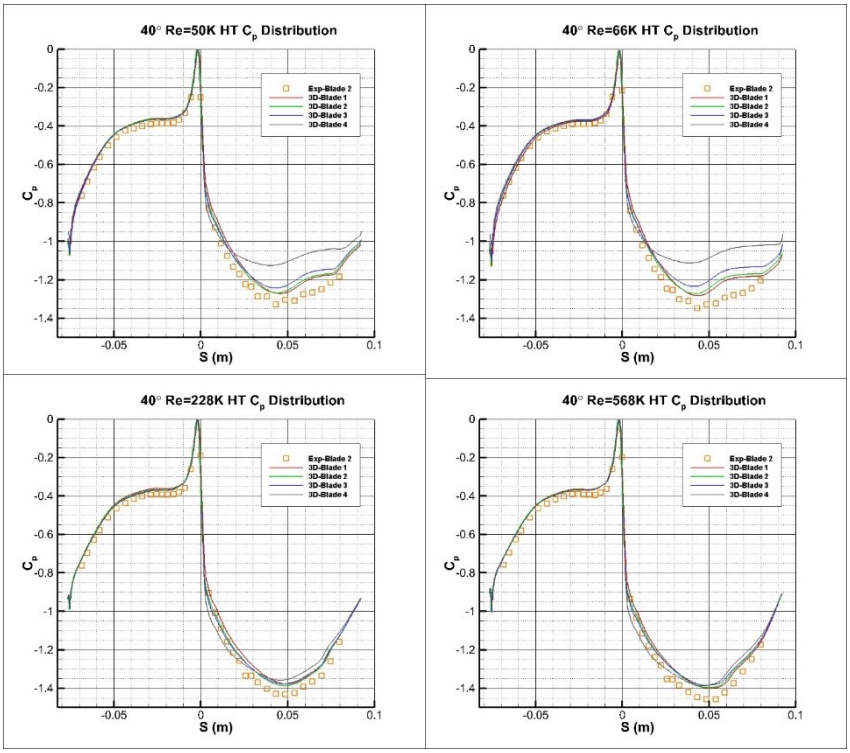

Figure 6.25. Pressure Coefficient Distribution for 40 Degree High Turbulence Cases

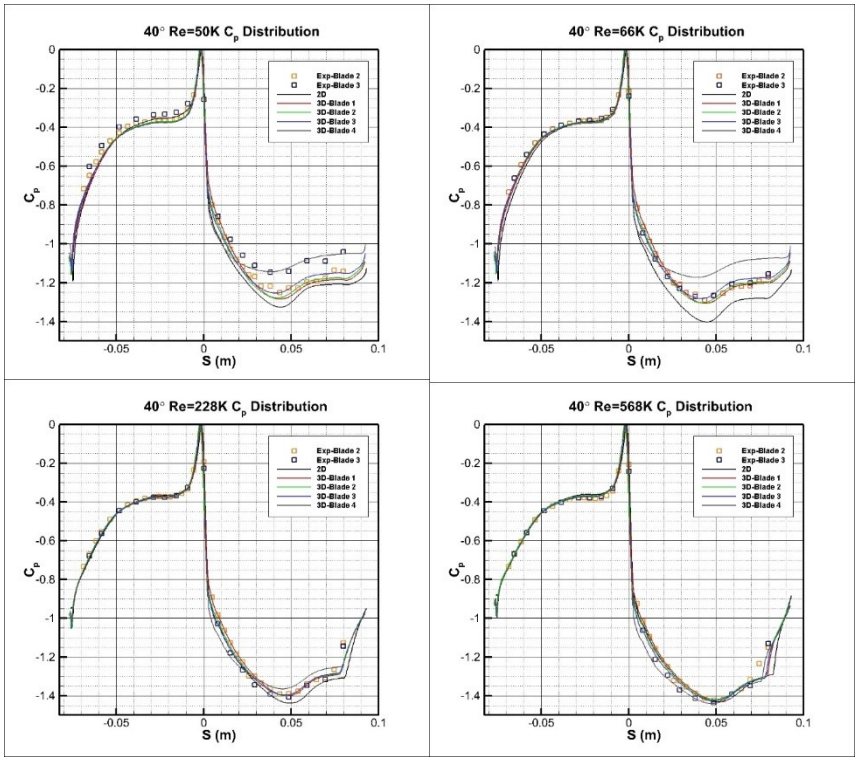

Figure 6.26. Pressure Coefficient Distribution for 40 Degree Low Turbulence Cases

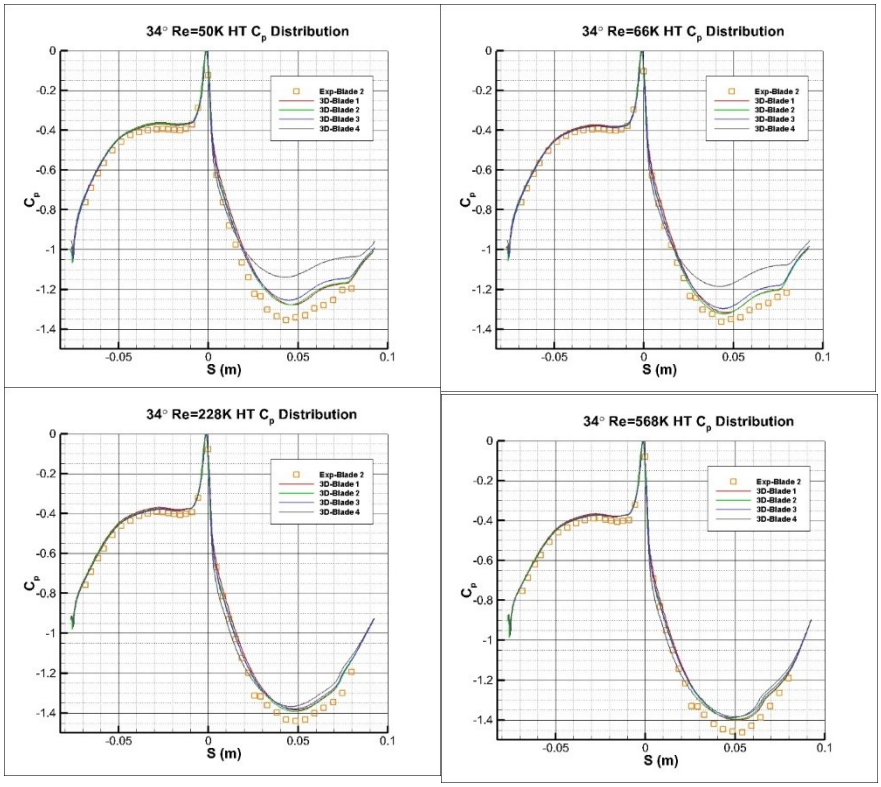

Figure 6.27. Pressure Coefficient Distribution for 34 Degree High Turbulence Cases

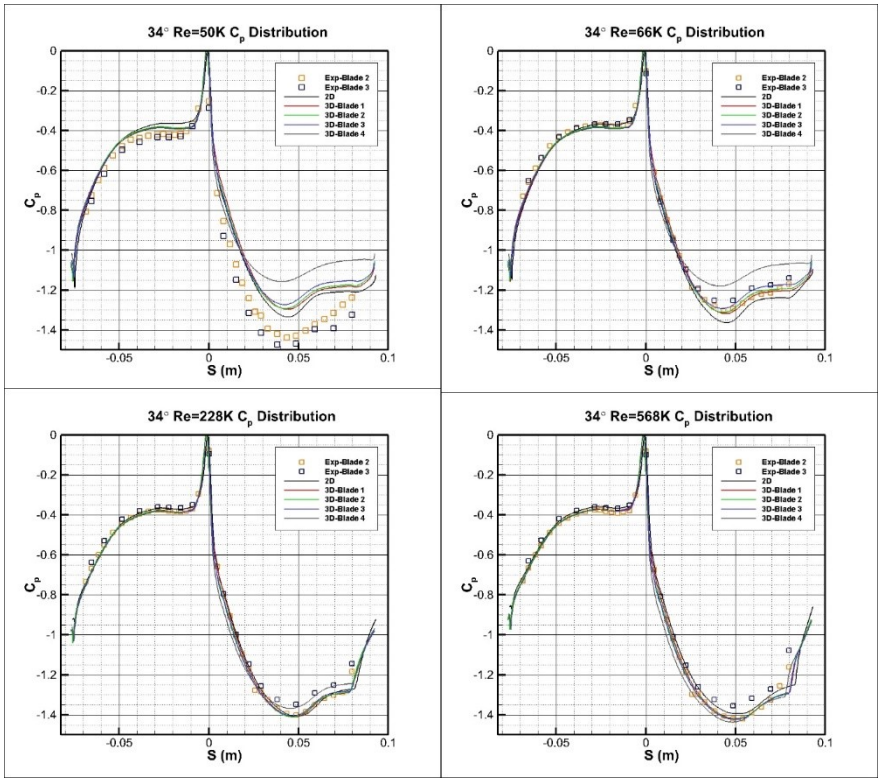

Figure 6.28. Pressure Coefficient Distribution for 34 Degree Low Turbulence Cases

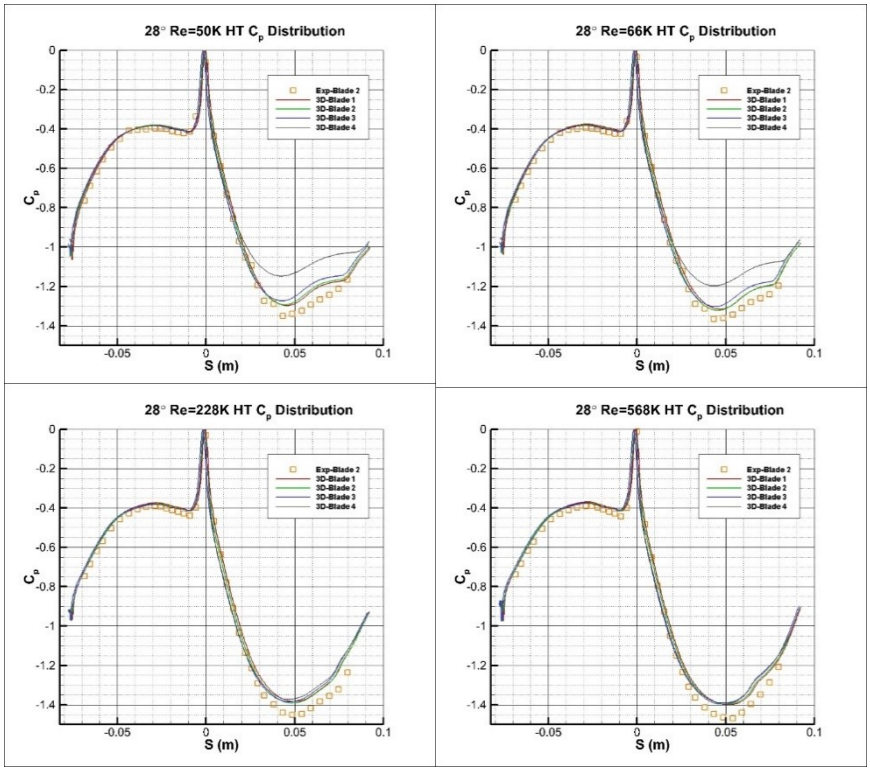

Figure 6.29. Pressure Coefficient Distribution for 28 Degree High Turbulence Cases

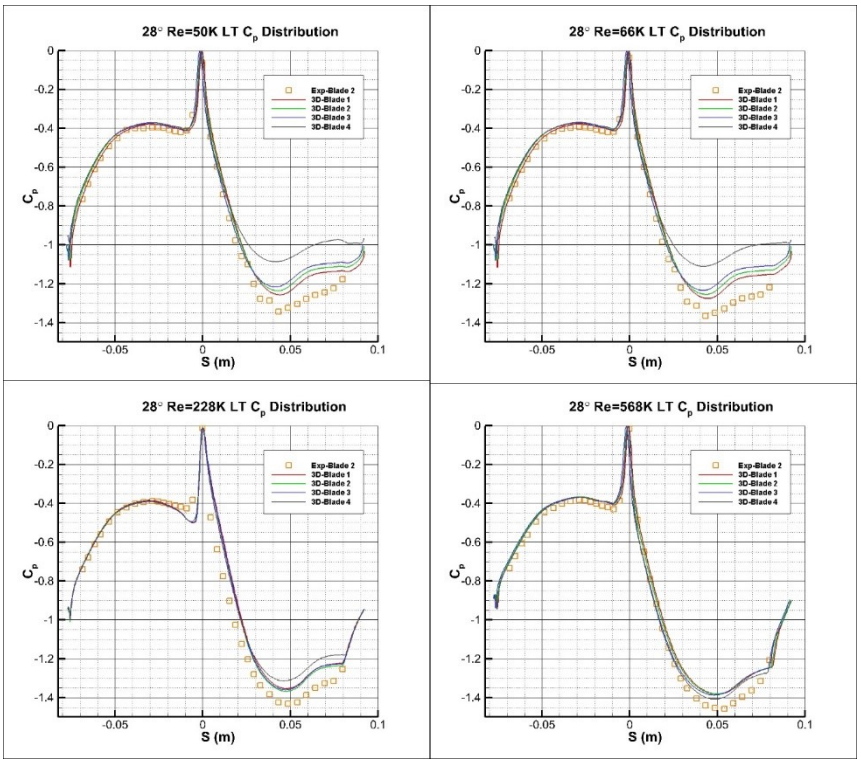

Figure 6.30. Pressure Coefficient Distribution for 28 Degree Low Turbulence Cases

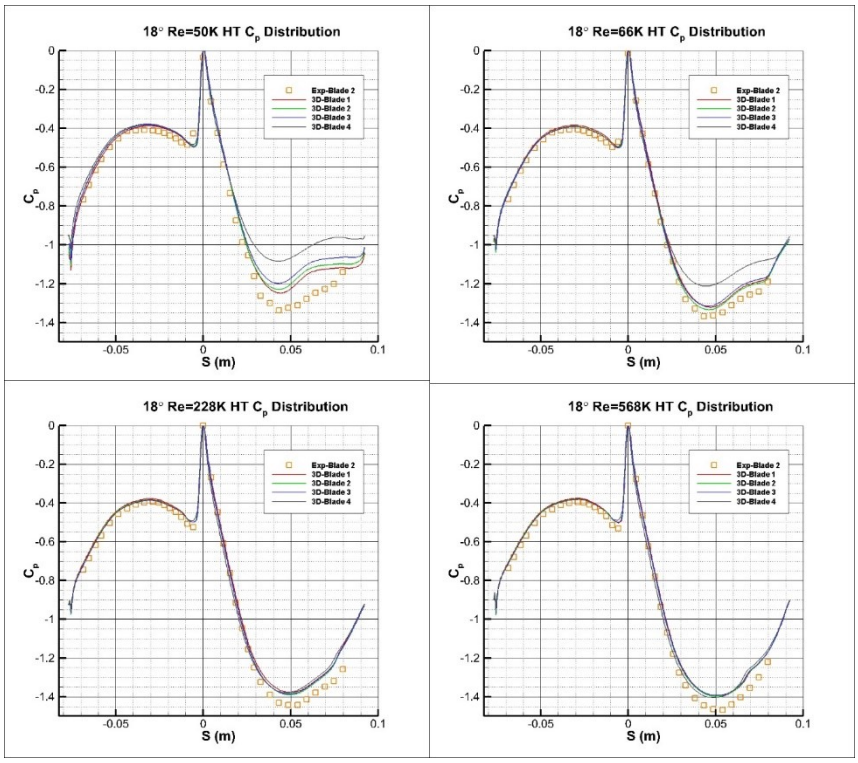

Figure 6.31. Pressure Coefficient Distribution for 18 Degree High Turbulence Cases

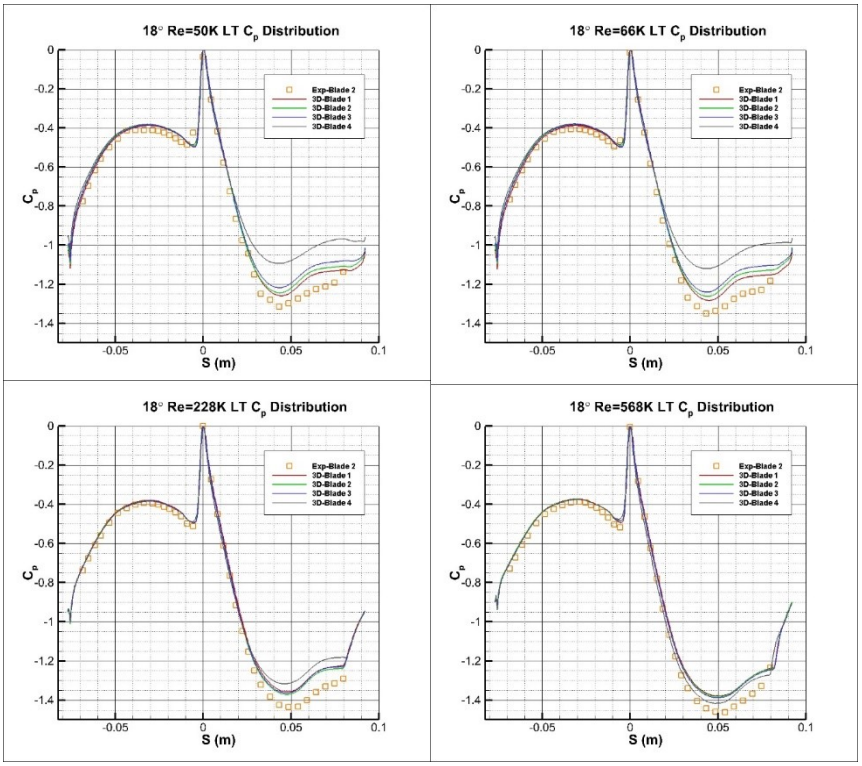

Figure 6.32. Pressure Coefficient Distribution for 18 Degree Low Turbulence Cases

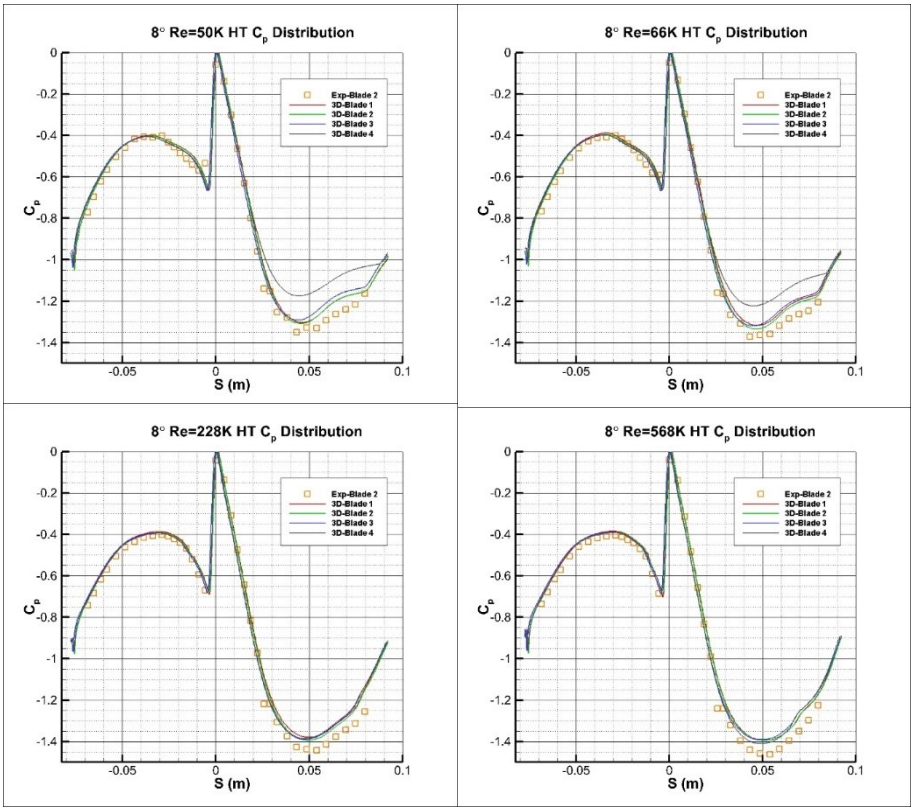

Figure 6.33. Pressure Coefficient Distribution for 8 Degree High Turbulence Cases

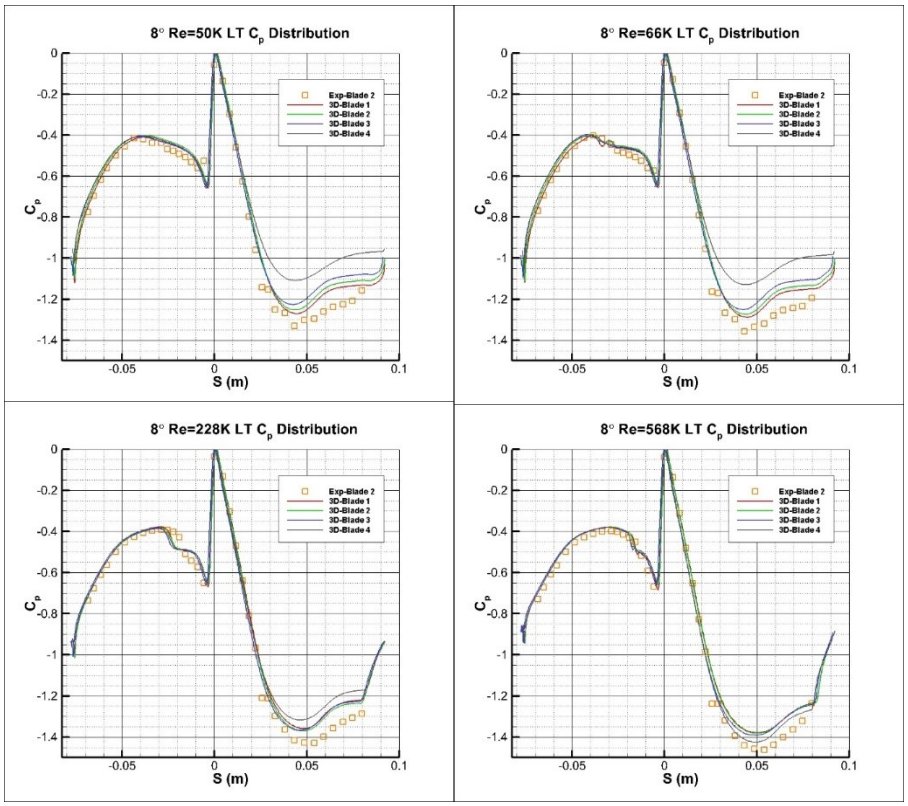

Figure 6.34. Pressure Coefficient Distribution for 8 Degree Low Turbulence Cases

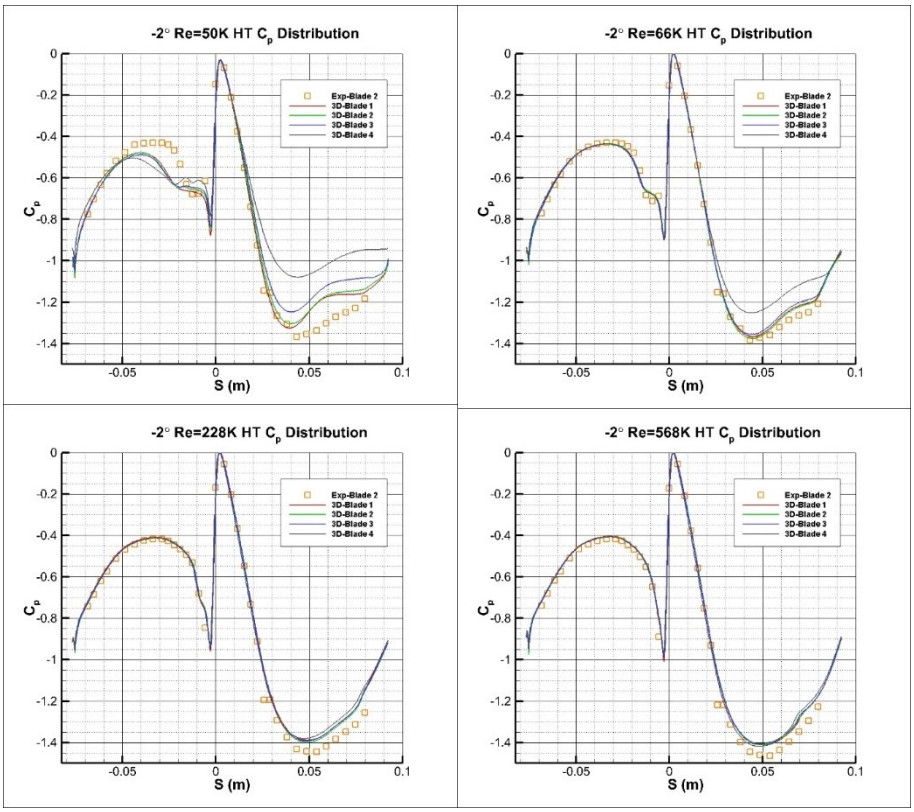

Figure 6.35. Pressure Coefficient Distribution for -2 Degree High Turbulence Cases

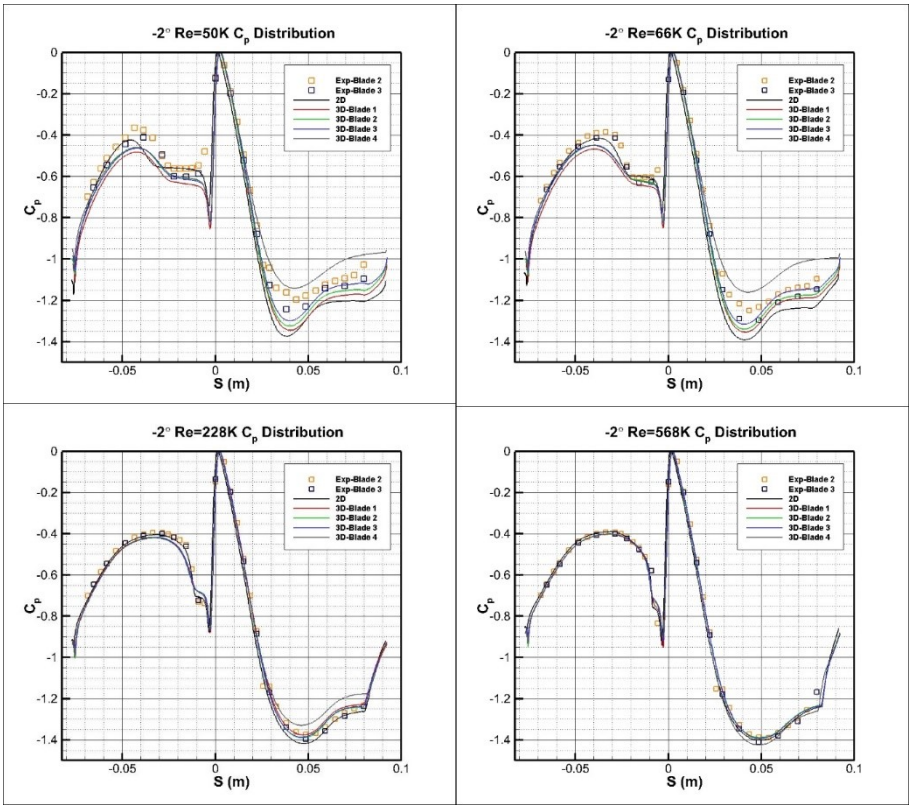

Figure 6.36. Pressure Coefficient Distribution for -2 Degree Low Turbulence Cases

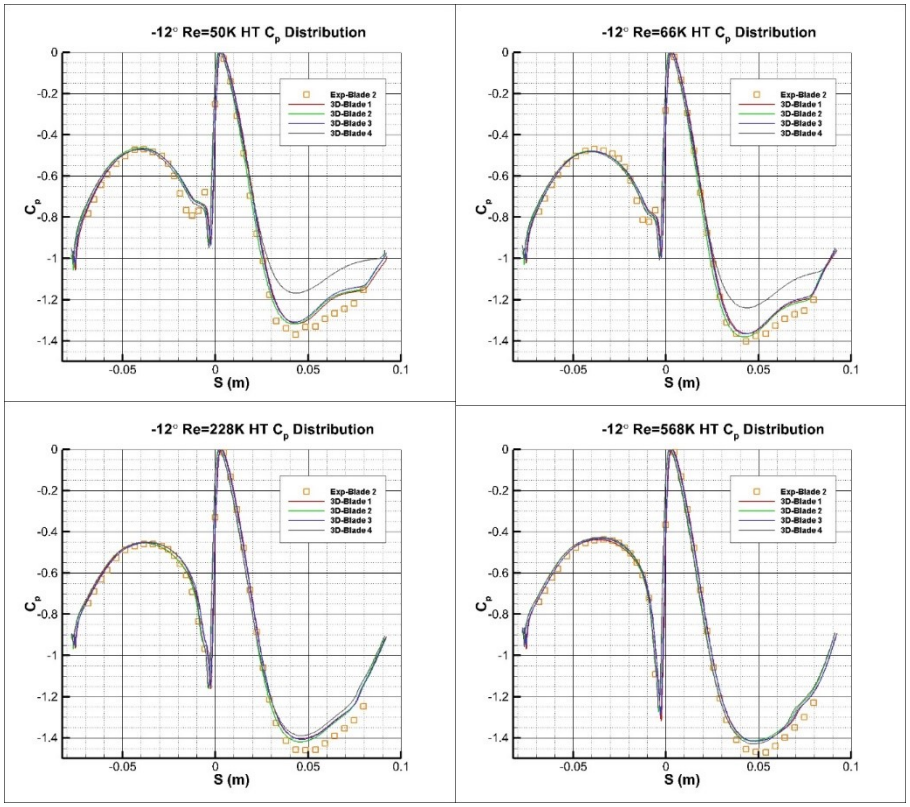

Figure 6.37. Pressure Coefficient Distribution for -12 Degree High Turbulence Cases

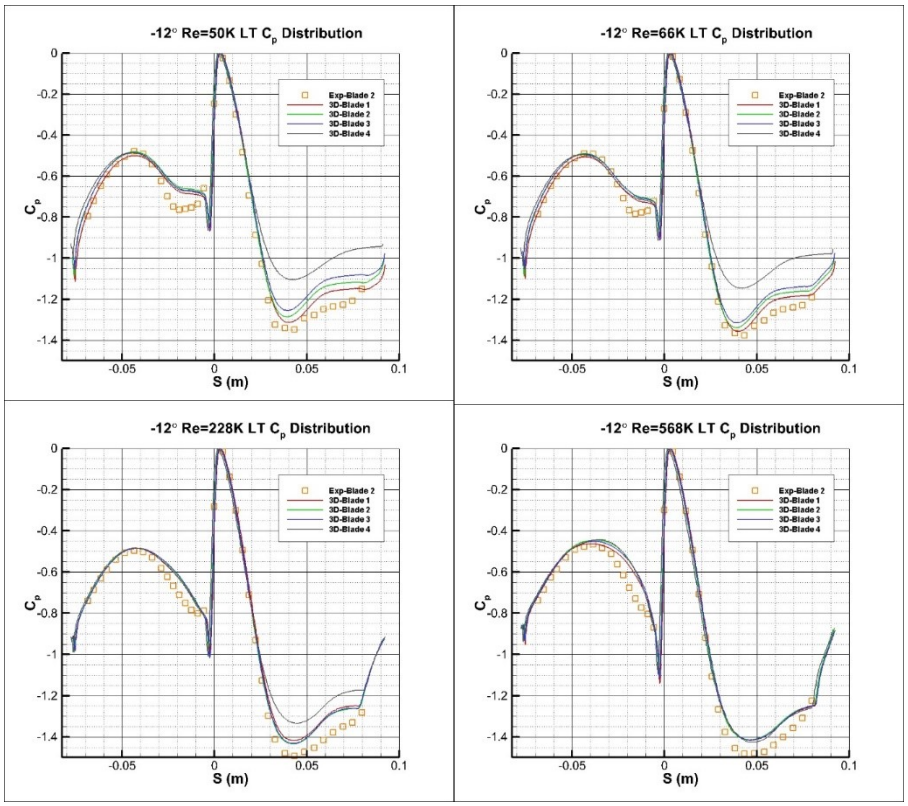

Figure 6.38. Pressure Coefficient Distribution for -12 Degree Low Turbulence Cases

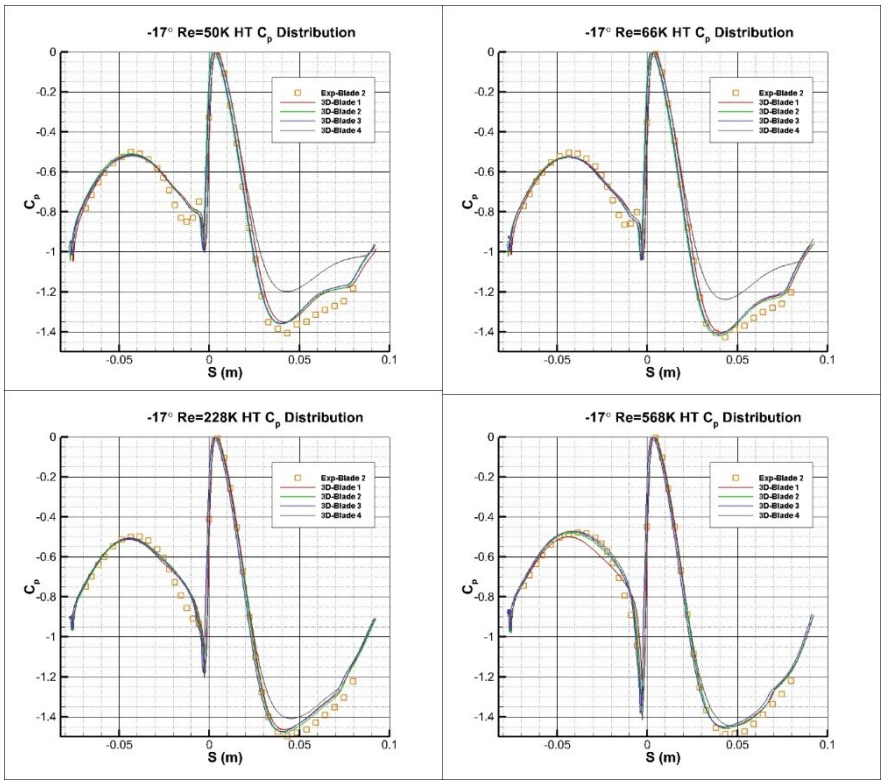

Figure 6.39. Pressure Coefficient Distribution for -17 Degree High Turbulence Cases

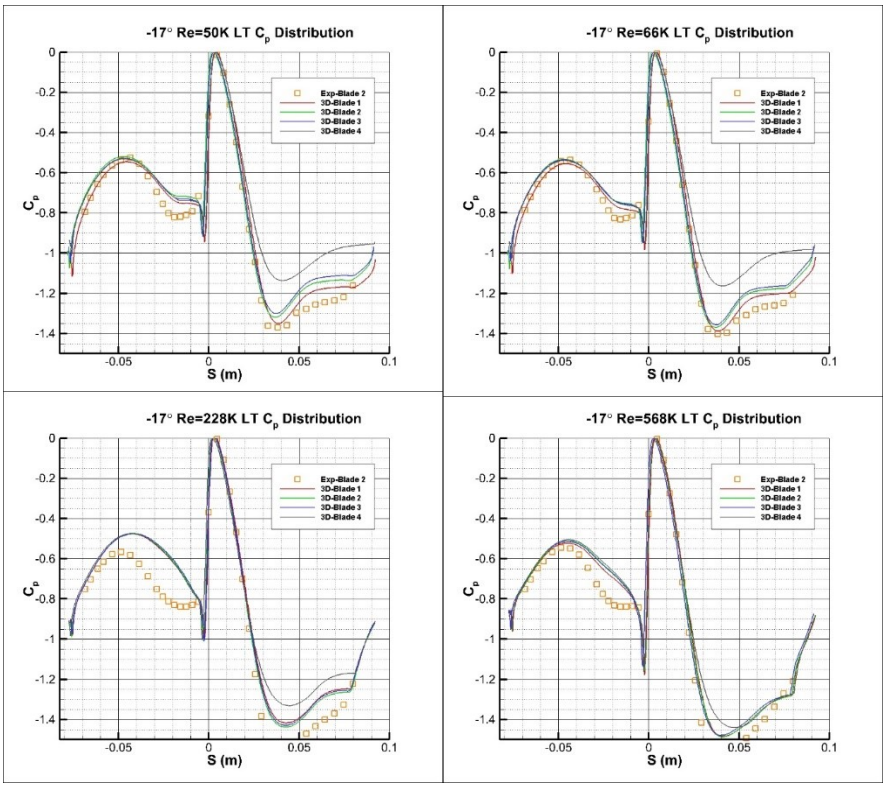

Figure 6.40. Pressure Coefficient Distribution for -17 Degree Low Turbulence Cases

The general trend with the turbine blade results showed overpredictions of the pressure coefficient on the suction surface of the blade. A significant amount of time has been dedicated to matching the experimental data by adjusting the flow speed to better match the experimental flow speed. Another key to this problem is matching the transition and separation regions on the blade surface. Current efforts involve matching experimental flow parameters such as Mach number and turbulence levels before and turbulence model manipulation takes place.

6.2.1.1. Results After Experimental Load Matching

To improve pressure coefficient predictions across the turbine blade surface, it is imperative that the simulation boundary conditions match those of the experiments as closely as possible. To test the accuracy of the flow conditions, the exit Mach number was plotted ¼ chord downstream, as this value was provided experimentally. Initially, the computational Mach number was much too low for each of the cases. To resolve this issue, the back pressure was

decreased at the outlet of the domain, effectively speeding up the flow. Once the outlet flow speed matched that of the experiment, the pressure coefficient was again compared with the experiments. Figure 6.41 below shows the experimental Mach number along with the downstream Mach number found with the computations. The blue line represents the experimental Mach number at ¼ chord downstream from the top of the cascade to the bottom. The red line represents the initial computational run, and the green line represents the computations after the back pressure was decreased to match the experimental flow speed.

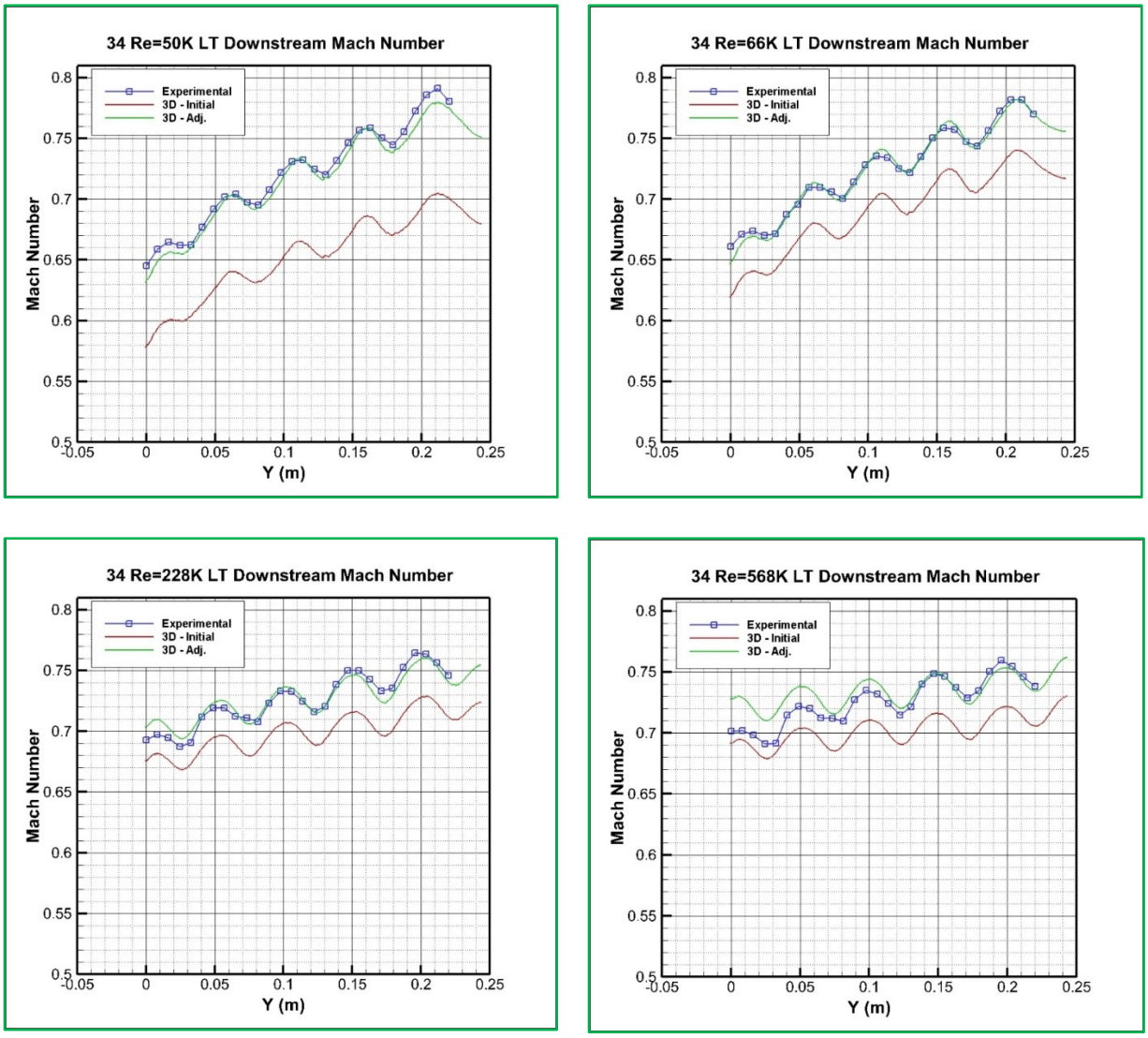

Figure 6.41. Downstream Mach Number Matching for 34 Degree Low Turbulence Case

After matching the Mach number with the experimental values through a trial and error process, the pressure coefficient distribution was much more accurate. Figure 6.42 and Figure 6.43 below reflect the changes of pressure coefficient across the surface before and after matching the Mach number. The lower Reynolds number cases are much more sensitive to the back pressure changes.

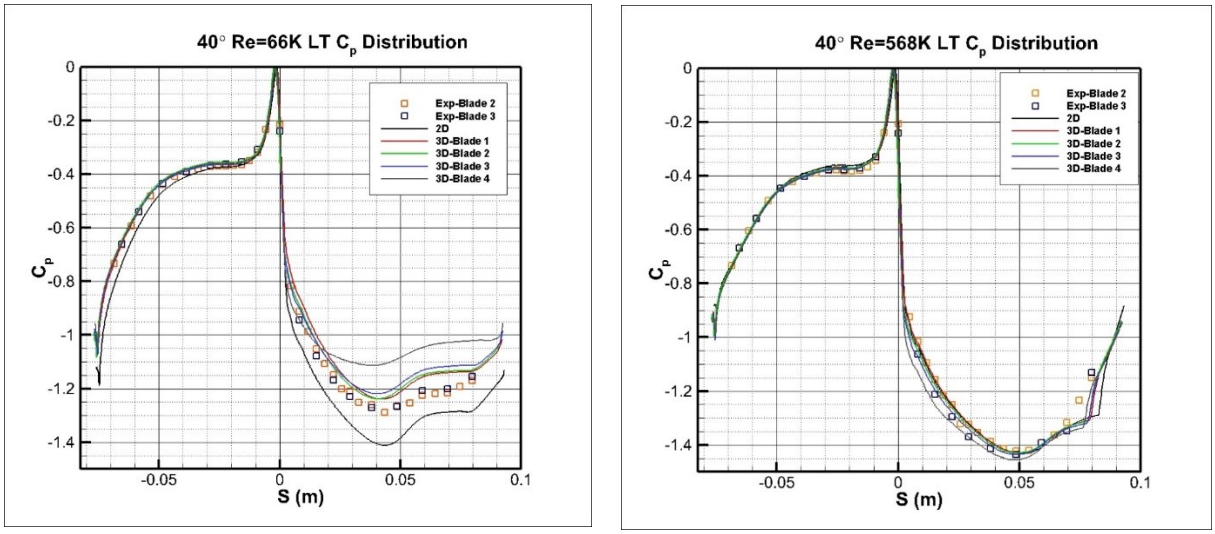

Figure 6.42. Pressure Coefficient before Mach Number Matching

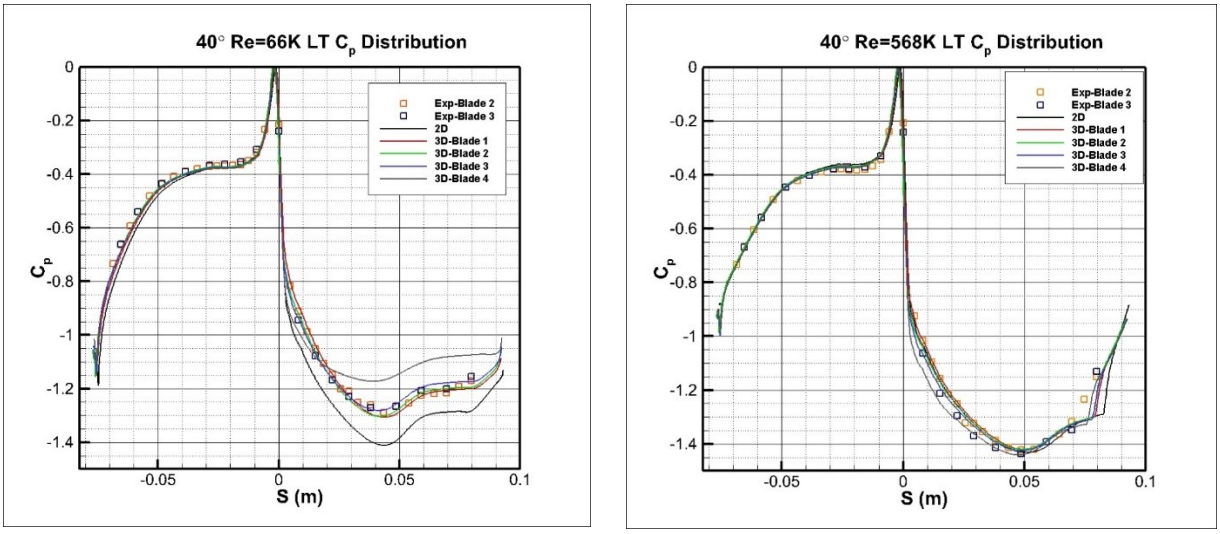

Figure 6.43. Pressure Coefficient after Mach Number Matching

These improvements are only shown for 2 of the cases; however, this process was completed for several other cases and the results are consistent with those shown above.

One other major discrepancy that was found between the computational data and the experiments was the length of separation bubble on the blade surface. The reason for this discrepancy is most likely that the turbulence levels were not consistent with those of the UND experiments. Since the experimental values are provided at a location ¼ chord upstream, the inlet turbulence must be estimated in the computations to match the experimental levels ¼ chord upstream. This estimation was an iterative process to match the experimental values. The yellow line along the inlet nozzle in Figure 6.44 below shows where inlet turbulence data was gathered. The turbulence kinetic energy and eddy dissipation rates both vary through the inlet along this line.

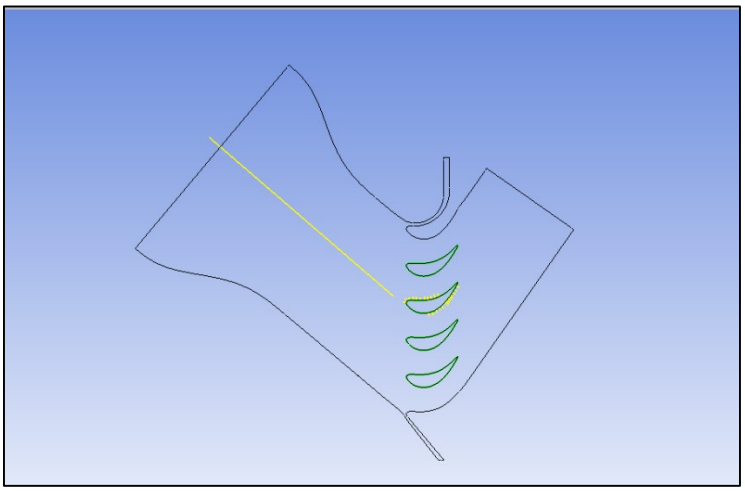

Figure 6.44. Inlet Line for Turbulence Matching

For this particular case, the turbulent kinetic energy decayed about 25% from the inlet of the nozzle to the ¼ upstream location, as shown in Figure 6.45 below. This rate of decay varies based on the inlet angle and Reynolds number, but it is important that the flow characteristics

match the experiments as closely as possible before any turbulence model manipulation take place.

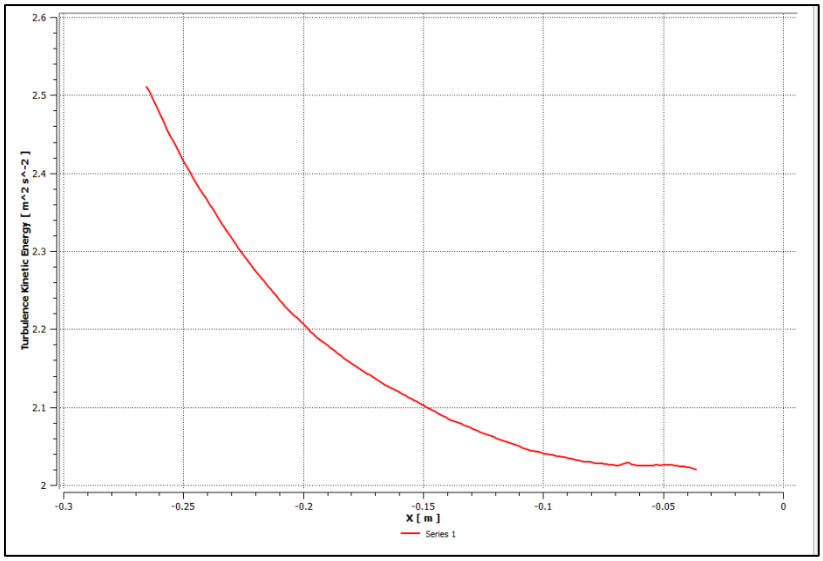

Figure 6.45. Decay of Turbulence Kinetic Energy through Inlet Nozzle

The turbulence kinetic energy and the eddy dissipation rate both vary through the inlet, and it is important to match both quantities to the experimental values before developing any changes to a turbulence model. A very small trial was conducted on a 40 degree case with varying inlet kinetic energy. As with most of the blade cases, a small separation bubble was detected in the computations, but the experiments showed no separation. Figure 6.46 below shows the pressure distribution after increasing the kinetic energy.

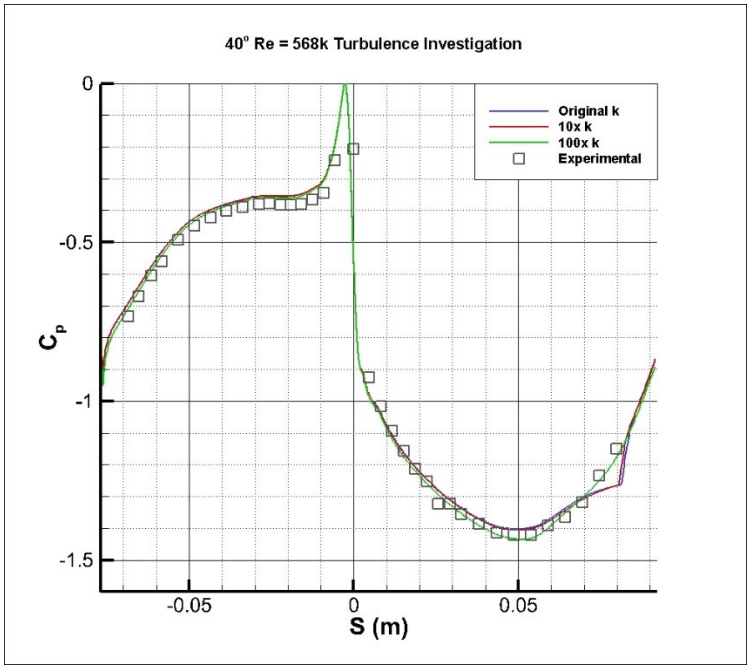

Figure 6.46. Pressure Coefficient after Turbulence Matching

It took nearly 100 times the experimental value of kinetic energy to prohibit the flow from separating. This discrepancy is far larger than expected, and it implies that something is setup incorrectly. Possible culprits include the implementation of the turbulence and transition model and the calculated experimental values. This discrepancy must be further investigated before any new turbulence modeling takes place.

7. CONCLUSIONS AND FUTURE WORK

7.1. **Conclusions**

Turbulence and transition modeling is a very important topic in the world of computational fluid dynamics. When dealing with gas turbine engines, accurate predictions of fluid flows require robust numerical models that incorporate the effects of turbulence levels, surface characteristics, pressure gradients, and flow speeds among many other factors. Because the nature of any turbulent flow is random and chaotic, modeling the flow is a complex subject that requires thorough testing and validation. This research project involved validating the Shear Stress Transport turbulence model coupled with the γ-Re_θ transition model on both an incidence angle tolerant turbine blade geometry and a first stage stator vane. When compared with the experimental data provided by UND, the simulation results are excellent for a large portion of the surface; however, the CFD model presented some discrepancies in areas where the flow transitions from laminar to turbulent.

The turbine blade predictions matched very closely to the experimental data on the pressure surface for positive angles of attack. As the angle of attack moves toward the takeoff position, the flow begins to separate on the pressure surface. The computations at NDSU also predict this separation bubble, but the length of separation and the onset position differ from experimental results. This behavior is very similar on the suction surface near the trailing edge of the blade for all the cases. At the lower Reynolds number range and the low turbulence conditions, the experimental data shows a small separation bubble, but the CFD simulations predicted a much larger region of separation. Possible causes of these discrepancies include inconsistent turbulence conditions from the experiment to the computations or deficiencies with the transition model.

When comparing aerodynamic data along the surface, the vane computations also exhibited very good results. The pressure surface predictions were nearly perfect over the entire Reynolds number range, and there were slight discrepancies on the suction surface that could be remedied by matching the experimental vane loading through a trial and error process. When a heat transfer study was conducted on this geometry, a major deficiency of the transition or turbulence model was uncovered on the suction surface. The onset of transition occurs too early when the Reynolds number increases of 360,000. Not only does the flow transition too early, it over predicts the heat transfer levels on the turbulent region of the vane surface. The fundamental goal of this project was to develop model corrections that would account for these discrepancies. The SST turbulence model was the primary turbulence model used in this project due to its optimal performance near the wall, but the k-ε model was implemented and modified to try to correct these heat transfer issues.

A modified k-ε model was implemented to better match the surface heat transfer results on the vane cases. Due to improper implementation or insufficient experimental turbulence data, the heat transfer predictions for this model were very close to that of a laminar solution. A second modification to the k-ε model was implemented with much more reasonable results. To test the implementation of these modified models, a comprehensive test was conducted and solution data was compared to experiments of a fundamental flow problem, a flat plate. The flat plate tests showed that there is further investigation to be done with the implementation of these modified k-ε models. One of the difficulties when modifying models in the ANSYS CFX software is the very limited access to the variables in the solver. CFX generally allows for small changes in model coefficients and properties, but not a complete overhaul of the model. To test this model further, a separate solver code should be used with complete access to model properties.

The discrepancies encountered with this project show that there is still a need for further transition and turbulence model refinement for flows at high turbulence intensity and Reynolds number. These findings are consistent with previous research projects at NDSU, and corrections are currently being developed to improve flow predictions under these conditions.

7.1.1. Future Work

To date, simulations have been conducted to compare with experimental data for all data sets provided. This totals 118 data sets, although it took a significantly higher number of simulations to properly set up and test the cases to ensure the proper settings were used. These simulations provide a comparison for the performance of the current SST turbulence model coupled with the γ-Re_θ transition model over a low pressure turbine geometry. This project can be taken a step further by implementing model changes that account for the shortcomings in the transition regions. Recommendations for improvement include developing an in-house source code that gives users full access to the solver and including corrections for compressibility effects to the transition model.

8. REFERENCES

Ames, F. .. (2013). Aerodynamic Loss Measurements in a Compressible Flow Vane Cascade Showing the Influence of Reynolds Number Lapse. *ASME Turbo Expo.* San Antonio, Texas.

Ames, F. (1997). The Influence of Large-Scale High Intensity Turbulence on Vane Surface Heat Transfer. *Journal of Turbomachinery*, 23-30.

Ames, F. E. (1999). An Algebraic Model for High Intensity Large Scale Turbulence. *ASME Turbo Expo* . Indianapolis, Indiana.

Ames, F. E. (2013). The Development of a Closed Loop High Speed Cascade Wind Tunnel For Aerodynamic and Heat Transfer Testing At Moderate To Low Reynolds Numbers. *ASME Turbo Expo.* San Antonio, Texas.

Ames, F. E., Argenziano, M., & Wang, C. (2004). Measurement and Prediction of Heat Transfer Distributions on an Aft-Loaded Vane Subjected to the Influence of Catalytic and Dry Low NOx Combustor Turbulence. *Journal of Turbomachinery*, 139-149.

Ames, F. E., Wang, C., & Barbot, P. A. (2003). Measurement and Prediction of the Influence of Catalytic and Dry Low NOx Combustor Turbulence on Vane Surface Heat Transfer. *Journal of Turbomachinery*, 221-231.

Ames, F., & Kwon, O. (1996). A Velocity and Length Scale Approach to k-e Modeling. *Journal of Heat Transfer*.

Anderson, J. (2011). *Fundamentals of Aerodynamics.* McGraw-Hill.

ANSYS . (2010). Retrieved from Turbulence Modeling: http://imechanica.org/files/fluent_13.0_lecture06-turbulence.pdf

ANSYS, Inc. (2011). *ANSYS CFX-Solver Theory Guide Release 14.0.*

Burden, T. (2008). *The Length, Time and Velocity Scales of Turbulence.* Retrieved from http://www2.mech.kth.se/courses/5C1218/scales.pdf

Chen, K. K., & Thyson, N. A. (1971). Extension of Emmons' Spot Theory to Flows on Blunt Boddies. *AIAA Journal*, 821-825.

Cho, J. R., & Chung, M. K. (1992). A k-e-y Equation Turbulence Model. *Journal of Fluid Mechanics*, 301-322.

Cutrone, L., Palma, P., Pascazio, G., & Napolitano, M. (2008). Predicting transition in two- and three-dimensional separated flows. *International Journal of Heat and Fluid Flow*, 504-526.

De Palma, P. (2006). Numerical simulations of three-dimensional trnsistional compressible flows in turbomachinery cascades. *International Journal of Numerical Methods for Heat & Fluid Flow*, 509-529.

Dhawan, S., & Narasimha, R. (1958). Some properties of boundary layer flow durin gthe transition from laminar to turbulent motion. *Journal of Fluid Mechanics*, 418-436.

Glassman, J., Whitney, W., & Steward, W. (1994). *Turbine Design and Application.* NASA SP-290.

Gostelow, J. P., Blunden, A. R., & Walker, G. J. (1994). Effects of Free-Stream Turbulence and Adverse Pressure Gradients on Boundary Layer Transition. *Journal of Turbomachinery*, 392-404.

Grotjans, H., & Menter, F. R. (1998). Wall Functions for General Application CFD Codes. *European Computational Fluid Dynamics Conference*.

Hinze, J. O. (1959). *Turbulence.* New York: McGraw-Hill.

Hodson, H. P. (2005). The role of transition in high-lift low-pressure turbines for aeroengines. *Progress in Aerospace Sciences*, 419-454.

Hoffman, K. A., & Chiang, S. T. (1998). *Computational Fluid Dynamics.* Wichita, KS: Engineering Education System.

Huang, J., Corke, T. C., & Thomas, F. O. (2003). Plamsa actuators for separation control of low pressure turbine blades. *AIAA Paper AIAA-2003-1027*.

Huber, J. (2013). *Numerical Simulations of Incompressible and Compressible Transitional Turbine Flows.* Fargo.

Kachanov, Y. S. (1994). Physical Mechanisms of Laminar-Boundary-Layer Transition. *Annual Rev. Fluid Mechanis*, 411-482.

Kaszeta, R. W., Simon, T. W., & Asphis, D. E. (2001). Experimental Investigation of Transition to Turbulence as Affected by Passing Wakes. *ASME Turbo Expo 2001, ASME Paper No. 2001-GT-0195*.

Kaynak, U. (2012). Transition at Low-Re Numbers for some Airfoils at High Subsonic Mach Numbers. In *Low Reynolds Number Aerodynamics and Transition.* InTech.

Kingery, L. B., Suzen, Y. B., & Ames, F. E. (2010). Computations of Heat Transfer in Transitional Turbine Flows. *10th AIAA/ASME Joint Thermophysics and Heat Transfer Conference.*

Kolmogorov, A. N. (1941). Local Structure of Turbulence in Incompressible Viscous Fluid for Very Large Reynolds Numbers. *Doklady Akademiya Nauk SSSR*, 299-303.

Lake, J. P., King, P. I., & Rivir, R. B. (1999). Reduction of separation losses on a turbine blade with low Reynolds number. *AIAA Paper AIAA-99-0242*.

Mayle, R. E. (1991). The Role of Laminar-Turbulent Transition in Gas Turbine Engines. *Journal of Turbomachinery*, 509-537.

Mayle, R. E., & Schulz, A. (1996). The Path to Predicting Bypass Transition. *Journal of Turbomachinery*, 405-411.

McAuliffe, B. R., & Metin, M. I. (2008). Numerical Study of Instability Mechanisms Leading to Transition in Separation Bubbles. *Journal of Turbomachinery*.

McAuliffe, B. R., & Metin, M. I. (2010). Transition Mechanisms in Separtion Bubbles Under Low- and Elevated- Freestream Turbulence. *Journal of Turbomachinery*.

McDonough, J. (n.d.). *Introduction to Turbulence Lecture Notes.* Retrieved from http://www.engr.uky.edu/~acfd/lctr-notes634.pdf

Medic, G., & Durbin, P. A. (2002). Toward Improved Prediction of Heat Transfer on Turbine Blades. *Journal of Turbomachinery*, 187-192.

Menter, F. R. (1994). Two-Equation Eddy-Viscosity Turbulence Models for Engineering Applications. *AIAA*.

Menter, F. R. (1997). Eddy Viscosity Transport Equations and Their Relation to the k-e Model. *Journal of Fluids Engineering*, 876-884.

Menter, F. R. (n.d.). Influence of Freestream Values on k-w Turbulence Model Predictions. *AIAA, 30*(6).

Menter, F. R., & Egorov, Y. (2010). The Scale-Adaptive Simulation Method for Unsteady Turbulent Flow Predictions. Part 1: Theory and Model Description. *Flow Turbulence Combust* (pp. 113-138). Springer Science.

Menter, F. R., & Langtry, R. B. (2012). Transition Modelling for Turbomachinery Flows. In *Low Reynolds Number Aerodynamics and Transition.* InTech.

Menter, F. R., Kuntz, M., & Bender, R. (2003). A Scal-Adaptive Simlation Model for Turbulent Flow Predictions. *AIAA*.

Menter, F. R., Langtry, R. B., Likki, S. R., Suzen, Y. B., Huang, P. G., & Volker, S. (2006). A Correlation Based Transition Model Using Local Variables - Part 2: Test Cases and Industrial Applications. *Journal of Turbomachinery*, 423-434.

Menter, F. R., Langtry, R. B., Likki, S. R., Suzen, Y. B., Huang, P. G., & Volker, S. (2006). A Correlation-Based Transition Model Using Local Variables - Part 1: Model Formulation. *Journal of Turbomachinery*, 413-422.

Mihelish, M. P., & Ames, F. E. (2013). The Development of a Closed Loop High Speed Cascade Wind Tunnel for Aerodynamic and Heat Transfer Testing at Moderate to Low Reynolds Numbers. *ASME Turbo Expo.* San Antonio, Texas.

Morkovin, M. V. (1969). On the many faces of transition. In *Viscous Drag Reduction* (pp. 1-31). New York: Plenum Press.

Munson, Young, Okiishi, & Huebsch. (2010). *Fundamentals of Fluid Mechanics.* John Wiley & Sons.

NASA. (n.d.). *Goddard Institute for Space Studies*. Retrieved October 2012, from http://www..giss.nasa.gov/reserach/briefs/canuto_01/

Piotrowski, W., Elsner, W., & Drobniak, S. (2010). Transition Predition on Turbine Blade Profile with Intermittency Transport Equation. *Journal of Turbomachinery*.

Praisner, T. J., & Clark, J. P. (2007). Predicting Transition In Turbomachinery - Part 1: A Review and New Model Development. *Journal of Turbomachinery*, 1-13.

Praisner, T. J., & Clark, J. P. (2007). Predicting Transition In Turbomachinery - Part 2: Model Validation and Benchmarking. *Journal of Turbomachinery*, 14-22.

Richardson, L. F. (1922). *Weather Prediction by Nymerical Process.* Cambridge University Press.

Rumsey, C. (2012, August 20). *NASA Turbulence Modeling Resource.* Retrieved from NASA Langley Research Center: http://turbmodels.larc.nasa.gov/flatplate.html

Savill, A. M. (1993). Some Recent Progress in the Turbulence Modeling of By-pass Transition. In *Near End Wall Flows* (pp. 829-848). Elsevier Sccience Publishers.

Schlichting, H. (1979). *Boundary Layer Theory.* New York: McGraw-Hill.

Schubauer, G. B., & Klebanoff, P. S. (1955). Contribution on the Mechanics of Boundary Layer Transition. *NASA TN 3489*.

Simon, F. F., & Stephens, C. A. (1991). *Modeling of the Heat Transfer in Bypass Transitional Boundary-Layer Flows.* NASA.

Simon, T. W., Qiu, S., & Yuan, K. (2000). Measurements in a Transitional Boundary Layer Under Low-Pressure Turbine Airfoil Conditions. *NASA-CR-2000-209957*.

Snyder, C. A. (2012). Preliminary Assessment of Variable Speed Power Turbine Technology on Civil Tiltrotor Size and Performance. *Annual Helicopter Society 68th Annyal Forum*.

Solomon, W. J., Walker, G. J., & Gostelow, J. P. (1995). Transition Length Prediction for Flows with Rapidly Changing Pressure Gradients. *ASME International Gas Turbine and Aeroengine Congess & Exposition*.

Spalart, P. R. (2000). Strategies for turbulence modeling and simulations. *International Journal of Heat and Fluid Flow*, 252-263.

Spalart, P. R., & Strelets, M. K. (2000). Mechanisms of transition and heat transfer in a separation bubble. *Journal of Fluid Mechanics*, 329-349.

Steelant, J., & Dick, E. (1996). Modelling of Bypass Transition with Conditioned Navier-Stokes Equations Coupled to an Intermittency Equation. *International Journal for Numerical Methods in Fluids*, 193-220.

Stieger, R. D. (2002). *The Effects of Wakes on Separating Boundary Layers in Low-pressure Turbines* (Vol. PHd dissertatoin). Cambridge University, Engineering Department.

Suzen, Y. B., & Huang, P. G. (1999). Modeling of Flow Transition Using an Intermittency Transport Equation. *NASA/CR-1999-209313*.

Suzen, Y. B., & Huang, P. G. (2005). Comprehensive validation of an intermittency transport model for transitional low-pressure turbine flows. *The Aeronautical Journal of the Royal Aeronautical Society*.

Suzen, Y. B., & Huang, P. G. (2005). Numerical Simulation of Unsteady Wake/Blade Interactions in Low-Pressure Turbine Flows Using an Intermittency Transport Equation. *Journal of Turbomachinery*, 431-444.

Suzen, Y. B., Huang, P. G., & Ashpis, D. E. (2007). A Computational Fluid Dynamics Study of Transitional Flows in Low-Pressure Turbines Under a Wide Range of Operating Conditions. *Journal of Turbomachinery*, 527-541.

Suzen, Y. B., Huang, P. G., Hultgren, L. S., & Ashpis, D. E. (2001). Predictions of Separated and Transtional Boundary Layers Under Low-Pressure Turbine Airfoil Conditions Using an Intermittency Transport Equation. *39th AIAA Aerospace Sciences Meeting & Exhibition AIAA 2001-0446*.

Suzen, Y. B., Xiong, G., & Huang, P. G. (2002). Predictions of Transitional Flows in Low-Pressure Turbines Using Intermittency Transport Equation. *AIA Journal*, 254-266.

Tennekes, & Lumley. (1972). *A First Course in Turbulence.* The Massachusetts Institute of Technology.

Versteeg, H. K., & Malalasekera, W. (2007). *An Introduction to Computational Fluid Dynamics: The Finite Volume Method.* Pearson Education Limited.

Vicedo, J., Vilmin, S., Dawes, S., & Savill, A. M. (2004). Intermiettency Transport Modeling of Separated Flow Transition. *Journal of Turbomachinery*, 424-431.

Volino, R. J. (2002). Separated Flow Transition Under Simulated Low-Pressure Turbine Airfoil Conditions - Part 1: Mean Flow and Turbulence Statistics. *Journal of Turbomachinery*, 656-664.

Volino, R. J. (2002). Separated Flow Transition Under Simulated Low-Pressure Turbine Airfoil Conditions - Part 2: Turbulence Spectra. *Journal of Turbomachinery*, 645-655.

Walker, G. (1993). The Role of Laminar-Turbulent Transition in Gas Turbine Engines: A Discussion. *Journal of Turbomachinery*, 207-217.

Wang, L., Fu, S., Carnarius, A., Mockett, C., & Theile, F. (2010). A modular RANS approach for modelling laminar-turbulent transition in turbomachinery flows. *International Journal of Heat and Fluid Flow*.

Welch, G. E. (2011). Computational Assessment of the Aerodynamic Performance of a Variable-Speed Power Turbine for Large Civil Tilt-Rotor Application. *American Helicopter Society 67th Annual Forum.* Virginia Beach, VA.

White, F. (2006). *Viscous Fluid Flow.* McGraw-Hill.

Wilcox, D. (2006). *Turbulence Modeling for CFD.* DCW Industries, Inc.

Wilcox, D. (2006). *Turbulence Modeling for CFD.* DCW Industries, Inc.

APPENDIX. IMPLEMENTATION OF NEW K-E MODEL INTO CFX USING CFX EXPRESSION LANGUAGE

The simulation setup software used in this research, CFX-Pre, allows users to modify various parts of the solver. In this case, the goal was to resolve the turbulence and transition models for cases with high turbulence intensity and high Mach numbers. This was done by manipulating the eddy viscosity based on a near wall damping function (Ames F. E., 1999). The following procedure is used to implement this new eddy viscosity model.

1. In the outline of CFX Pre, right click on the **Expressions** folder and click **Insert Expression.**

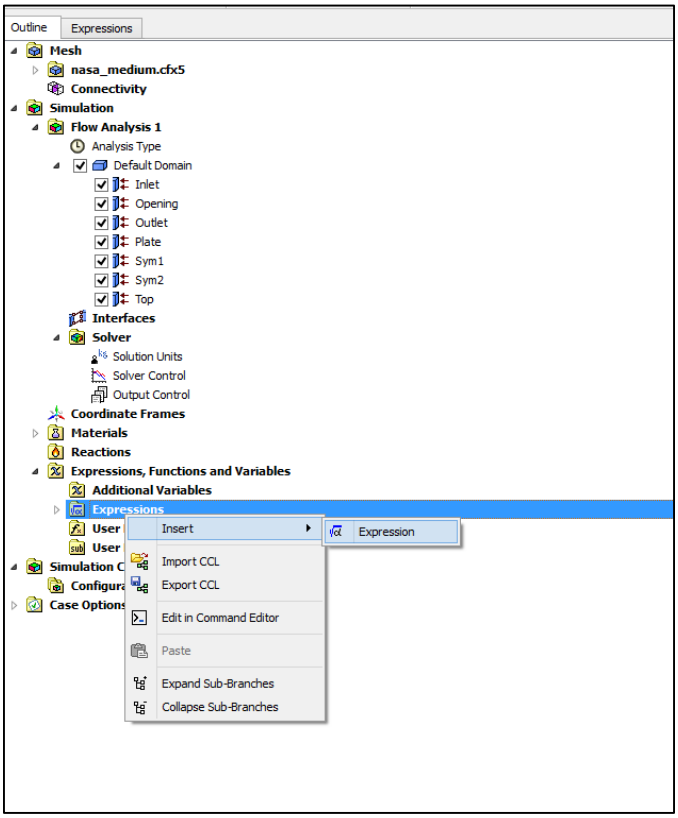

Figure A.1. Insert CFX Expression

2. In the new Expressions tab, right click again on the **Expressions** folder, click **Insert Expression,** and give the expression a name.

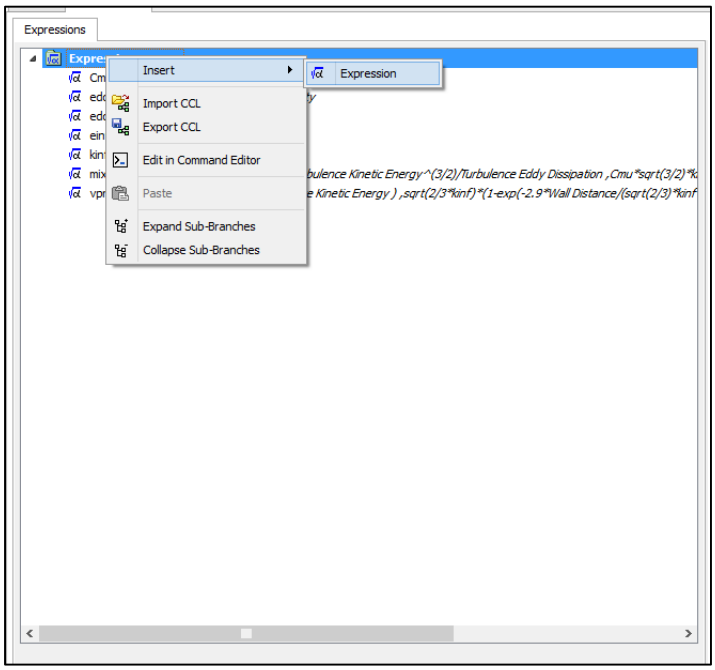

Figure A.2. Insert and Name the Expression

3. Expressions can be constants or equations made up of any variables that are available in CFX. Equations can also be made up of any other user-defined expressions or functions as well. An extensive list of the available functions and variables can be found by right clicking in the Definition area of the expression and hovering the mouse over the desired category, as shown in the figure below.

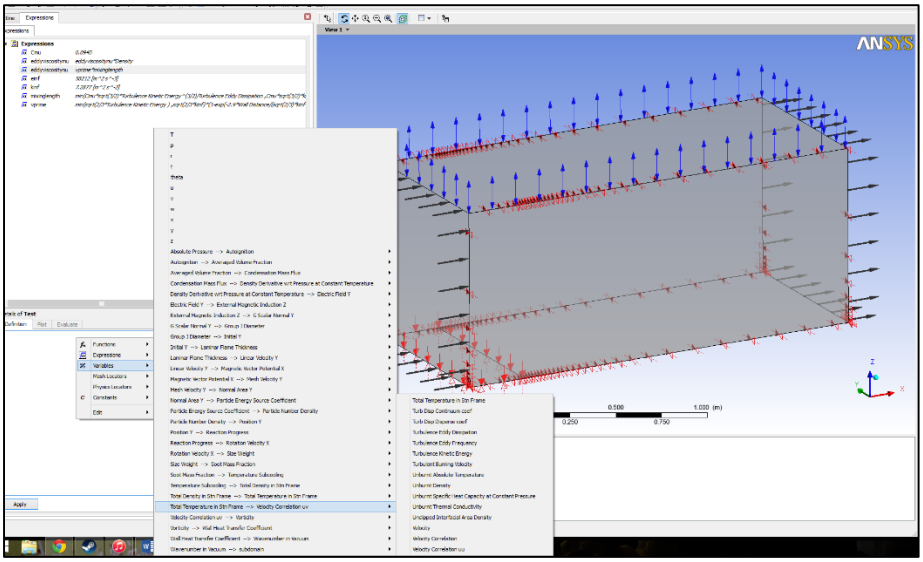

Figure A.3. Insert Software Functions into CFX Expressions

4. In this case, an expression was created to represent the eddy viscosity based on the Wall Distance variable. As the distance from the wall grows, a different equation for eddy viscosity is implemented based on the CFX expression. When all of the expressions and equations are defined, the modified eddy viscosity can be implemented by entering the expression name under the Fluid Models tab.

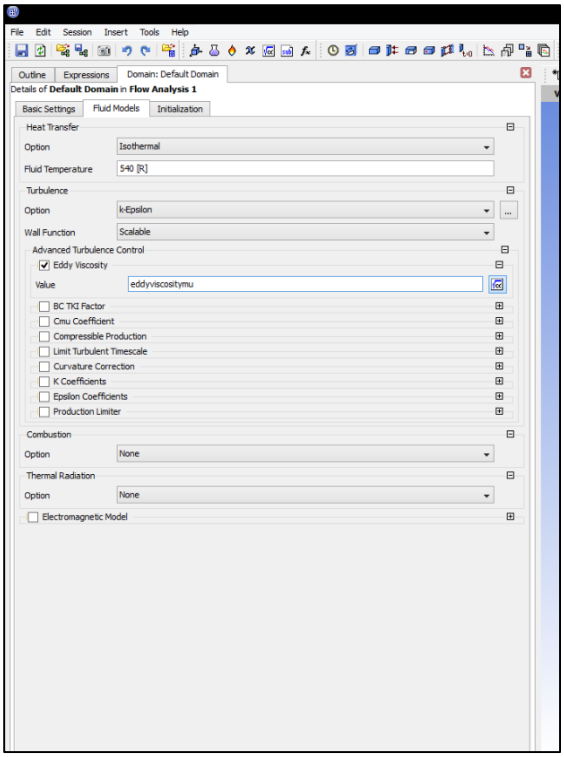

Figure A.4. Implement the New Expression

5. The expression name is “eddyviscositymu” in this case, and it is entered by clicking **Default Domain** in the model outline, then the **Fluid Models** tab, and finally the “+” symbol next to advanced turbulence control. Note that all units must be specified in the expressions created previously, or CFX will not allow the new eddy viscosity to be implemented. It should also be noted that this model was added to modify the k-epsilon turbulence model. Different turbulence models will have different options when clicking on the advanced turbulence control button.